UNIVERSIDAD POLITÉCNICA DE MADRID

Escuela Técnica Superior de Ingeniería y Sistemas de Telecomunicación

Joint-Transceiver Design for Short Reach Multi-Mode Fiber Systems

D O C T O R A L T H E S I S

Submitted for the Degree of Doctor by:

Jasmeet Singh
M. Eng.

Madrid, 2024

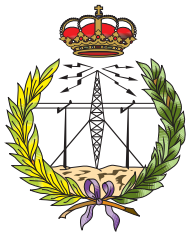

UNIVERSIDAD POLITÉCNICA DE MADRID
Escuela Técnica Superior de Ingeniería y
Sistemas de Telecomunicación

Doctoral Degree in Systems and Services Engineering for the Information Society

Joint-Transceiver Design for Short Reach Multi-Mode Fiber Systems

D O C T O R A L T H E S I S

Submitted for the Degree of Doctor by:

Jasmeet Singh
M. Eng.

Under the supervision of:
Prof. Dr. César Benavente-Peces (Supervisor)
Prof. Dr.-Ing. habil. Andreas Ahrens (Co-supervisor)

Madrid, 2024

Title: Joint-Transceiver Design for Short Reach Multi-Mode Fiber Systems

Author: Jasmeet Singh

Doctoral Programme: Systems and Services Engineering for the Information Society

Thesis Supervision:

Prof. Dr. César Benavente-Peces, Professor at Universidad Politécnica de Madrid, Spain (Supervisor)

Prof. Dr.-Ing. habil. Andreas Ahrens, Professor at Hochschule Wismar, Germany (Co-Supervisor)

External Reviewers:

Thesis Defense Committee:

Thesis Defense Date:

Dedicated

to my parents...

Acknowledgments

I would like to express my sincere gratitude to Prof. Andreas Ahrens for providing the opportunity to work on this topic. I am grateful for his constant support and encouragement, which significantly enriched the quality of this research work. In addition to insightful discussions and valuable feedback, his unwavering confidence in me has played a crucial role in the completion of this work.

I owe my deepest gratitude to Prof. Steffen Lochmann for sharing his profound knowledge regarding the development of the experimental testbed. His expertise, patience, and fruitful discussions have been instrumental in shaping this dissertation. I am also grateful to Prof. César Benavente-Peces for providing me the opportunity to pursue doctoral studies at Universidad Politécnica de Madrid, and I would like to thank him for his scientific and organizational guidance.

Furthermore, I would like to express my appreciation to Mr. Ralph Bornitz for productive discussions, which have proven to be resourceful. Special thanks to my friend and colleague, Marek Götten, for proofreading my dissertation and providing constant motivation throughout this work. Your insights and camaraderie have made this endeavor all the more rewarding. I would like to thank Valeria Ibarra Ramirez for supporting the Spanish parts of this work. Finally, I want to express my deep appreciation to Anna Yasynetska; your support and understanding have been a cornerstone during this dissertation.

My heartfelt gratification is dedicated to my family for their unending support and encouragement. To my parents, Baljit Singh and Balvinder Kaur, your enduring belief in my potential and standing by me through the challenges have been the driving force behind completing this dissertation.

Jasmeet Singh

Resumen

Esta tesis doctoral presenta un diseño novedoso de ecualizador de transceptor conjunto para sistemas de fibras multimodo (MMF) de corto alcance, con modulación de intensidad y detección directa (IM/DD). Un diseño óptimo combinado del pre y post-ecualizador permite mejoras en el rendimiento del sistema. Un pre-ecualizador de feed-forward lineal con algunos coeficientes filtro es incorporado para permitir una señalización multinivel para conservar la estructura sencilla del transmisor. Mediante la utilización de apenas unos pocos coeficientes filtro del pre-ecualizador, la señalización multinivel es responsable de la mitigación parcial de un canal MMF. Consecuentemente, las interferencias residuales son compensadas con un post-ecualizador en el receptor. Contrario a los esquemas de pre y post ecualización (PPE) convencionales, los coeficientes del esquema PPE conjunto o del ecualizador de transceptor conjunto son diseñados y optimizados conjuntamente utilizando un algoritmo de optimización numérica. Este sistema de ecualización recientemente desarrollado se adapta a un sistema IM/DD óptico con una extensa aplicabilidad que va desde conceptos de entrada y salida única (SISO) hasta conceptos de entrada y salida múltiple (MIMO). El rendimiento del sistema del esquema PPE conjunto es analizado y comparado con los esquemas comúnmente utilizados de solo post-ecualización (PE-only) y con la técnica PPE basada en el principio de forzar a cero (ZF). Considerando un sistema SISO con una conexión MMF de 250 m de longitud, la potencia óptica recibida requerida para alcanzar un rango de error bit (BER) de 10^{-3} utilizando el ecualizador PEE conjunto se ve reducido en un 7.3% para PE-ZF y en un 6.8% para un error cuadrático medio mínimo (MMSE) PE-only. Adicionalmente, se observan mejoras significativas en el rendimiento del sistema con un incremento en el número de coeficientes del pre-ecualizador, al utilizar el ecualizador PPE conjunto. Cuando se aplica el esquema PPE conjunto a un sistema óptico MIMO (2×2) en un canal MMF de 1.4 km de longitud, la potencia óptica recibida promedio para alcanzar un BER de 10^{-4} mejora 2.58 dB para el formato PAM-2 y 2.68 dB para el formato PAM-4 en comparación con PEMMSE. Bajo los escenarios analizados, los beneficios alcanzados en el rendimiento del BER al utilizar el sistema PPE conjunto son el doble de los alcanzados con los esquemas ZF-PPE utilizados convencionalmente. Agregando a lo anterior, la apertura del diagrama de ojo, al analizar el rango de señal-a-ruido de diferentes esquemas de ecualización, coincide con su respectivo rendimiento de BER. Los resultados experimentales de BER obtenidos también son comparados con simulaciones Monte-Carlo. Mejoras adicionales en los rendimientos BER son posibles al aplicar descomposición en valores singulares (SVD) y método de asignación de potencia en combinación con el esquema PPE conjunto. En las simulaciones por com-

putadora, la potencia óptica promedio requerida para alcanzar un BER de 10^{-4} utilizando el esquema SVD-PPE se reduce en 3.52 dB para el formato PAM-2 y en 3.82 dB para el formato PAM-4, ambos con un canal MMF de 1.4 km en configuración MIMO (2×2). El diseño de ecualizador de transceptor conjunto supera a diversos esquemas de ecualización en sistemas IM/DD basados en MMF al hacer posible la señalización multinivel en el lado del transmisor.

Abstract

This dissertation presents a novel joint-transceiver equalizer design for short reach multi-mode fiber (MMF) systems with intensity modulation and direct detection (IM/DD). A combined optimal design of the pre-and post-equalizer allows improvements in the system performance. A linear feed-forward pre-equalizer with a few taps is incorporated to enable multi-level signaling in order to retain a simple structure of a transmitter. The multi-level signaling using just a few filter coefficients of a pre-equalizer is responsible for the partial mitigation of an MMF channel. Consequently, the residual interferences are compensated with a post-equalizer at the receiver. In contrary to state-of-the-art pre- and post-equalization (PPE) schemes, the coefficients of the joint-PPE scheme or joint-transceiver equalizer are designed and optimized together using a numerical optimization algorithm. This newly developed equalization scheme is tailored for an optical IM/DD system with extensive applicability from single-input and single-output (SISO) to multiple-input and multiple-output (MIMO) concepts. The system performance of the joint-PPE scheme is analyzed and compared with the commonly used post-equalization only (PE-only) schemes and PPE technique based on the zero-forcing (ZF) principle. Considering a SISO system with a 250 m long MMF link, the required optical received power to reach a bit-error rate (BER) of 10^{-3} using the joint-PPE is reduced by 7.3% for PE-ZF and 6.8% for minimum mean square error (MMSE) PE-only. Additionally, significant improvements in the system performance using the joint-PPE equalizer are observed with an increase in the number of pre-equalizer coefficients. When the joint-PPE scheme is applied on a (2×2) optical MIMO system over a 1.4 km long MMF channel, the average optical received power to reach a BER of 10^{-4} is improved by 2.58 dB for PAM-2 and 2.68 dB for PAM-4 formats in comparison to PE-MMSE. Under the analyzed scenarios, the achieved BER performance benefits utilizing the joint-PPE are twice that of the conventionally used ZF-PPE schemes. Furthermore, the eye openings at analyzed signal-to-noise ratio from the different equalization schemes agree with their respective BER performance. The obtained experimental BER results are also compared with Monte-Carlo simulations. Further enhancement in the BER performances is enabled by applying singular value decomposition (SVD) and power allocation methods in combination with the joint-PPE scheme. From the computer simulations, the required average optical power to reach a 10^{-4} BER using the SVD-PPE scheme is lowered by 3.52 dB for PAM-2 and 3.82 dB for PAM-4 formats with a 1.4 km MMF channel in (2×2) MIMO configuration. The joint-transceiver equalizer design outperforms different equalization schemes in MMF-based IM/DD systems by enabling multi-level signaling at the transmitter side.

Contents

List of Abbreviations

ADC	Analog/digital Conversion
AWG	Arbitrary Waveform Generator
AWGN	Additive, White And Gaussian Noise
BER	Bit-error Rate
CAP	Carrier-less Amplitude Phase Modulation
DML	Directly-modulated Laser
DMT	Discrete Multi-tone
DSO	Digital Storage Oscilloscope
DSP	Digital Signal Processing
FBG	Fiber-Bragg Grating
FIR	Finite Impulse Response
FMF	Few-mode Fiber
GCS	Geometric Constellation Shaping
HOM	High-order Mode
HOMF	Higher-order Modulation Format
HPGCS	Hybrid Probabilistic-geometric Constellation Shaping
ICI	Inter-channel Interference
IM/DD	Intensity Modulation / Direct Detection
ISI	Inter-symbol Interference
LOM	Lower-order Mode
LP	Linearly-polarized
MCF	Multi-core Fiber
MIMO	Multiple-input And Multiple-output
MMF	Multi-mode Fiber
MMSE	Minimum Mean Square Error
MPLC	Multi-plane Light Converter
MZM	Mach-Zehnder Modulator
NWF	Noise Weighting Factor
OFC	Optical Fiber Communication
OOK	On-off Keying
PAM	Pulse-amplitude Modulation
PCS	Probabilistic Constellation Shaping
PDF	Probability Density Function
PDM	Polarization-division Multiplexing
PE-only	Post-equalization Only
PFS	Parallel Frame Synchronization
PPE	Pre- And Post-equalization
PRBS	Pseudo-random Binary Sequence
QAM	Quadrature Amplitude Modulation
S/P	Serial-to-parallel
SCM	Subcarrier Modulation
SDM	Space-division Multiplexing

SISO	Single-input And Single-output
SMF	Single-mode Fiber
SNR	Signal-to-noise-ratio
SVD	Singular Value Decomposition
TDM	Time-division Multiplexing
VOA	Variable Optical Attenuator
WDM	Wavelength-division Multiplexing
ZF	Zero-forcing

List of Symbols

$s(k)$	All the elements in the series
k_B	Boltzmann constant
$\mathrm{erfc}(\cdot)$	Complementary error operator
H	Conjugate transpose or Hermitian operator
$*$	Convolution operator
$\boldsymbol{V}$	Eigen matrix with $(n_\mathrm{R} \times n_\mathrm{T})$ dimensions
q	Electro-optical conversion factor
A	Fiber attenuation in dB/km
$\boldsymbol{H}$	Frequency-selective channel matrix
$s_{\mu,m}$	Gray coded input symbols
U_A	Half vertical eye opening
U_π	Half-wave voltage
$\boldsymbol{s}$	Input signal matrix
$s_\mu(k)$	Input symbol sequence at μ-th MIMO input
$s[k]$	k-th element from the series
L_h	Length of the channel taps
L_f	Length of the post-equalizer filter
L_p	Length of the pre-equalizer filter
μ	MIMO input index
ν	MIMO output index
M_μ	Modulation format index at μ-th MIMO input
$\boldsymbol{w}$	Noise signal vector
P_n	Noise power
N_μ	Number of distinct pre-equalizer levels
n_T	Number of MIMO inputs
n_R	Number of MIMO outputs
$\Re$	Photodiode responsivity
α_0	Pockels coefficient
$\boldsymbol{F}$	Post-equalizer matrix
$b_\mu(k)$	Pre-equalized symbol stream
$\boldsymbol{b}$	Pre-equalized multi-level transmitted signal
$p_\mu(k)$	Pre-equalizer filter coefficients
$\boldsymbol{P}$	Pre-equalizer matrix
β_{ml}	Propagation constant
$n(r)$	Radial refractive index distribution
$\boldsymbol{r}$	Received signal matrix
$\mathbb{N}^+$	Set of natural numbers excluding zero
$\mathbb{Z}^+$	Set of non-negative integers including zero
c	Speed of light
ϱ_μ	Transmission quality
$\boldsymbol{S}$	Unitary matrix with $(n_\mathrm{R} \times n_\mathrm{R})$ dimensions
$\boldsymbol{D}$	Unitary matrix with $(n_\mathrm{T} \times n_\mathrm{T})$ dimensions

List of Figures

List of Tables

1. Introduction

Digital communication has become an integral part of everyone's daily life. From high-resolution video streaming to a bank transaction, every single bit of information is carried by optical fibers, which are present at data centers, mobile radio backhaul, under the seas or core networks. Optical fiber communication (OFC) systems are the backbone to support this infrastructure. Optical fibers offer higher bandwidth-length products and resistance to electromagnetic interference compared to copper wires. Thus, optical fibers are revolutionizing the telecommunication industry [Agr02; Rao20].

The evolution of OFC continues to play a significant role in enabling the proliferated usage of the internet. Accordingly, the demand for solutions to achieve higher data throughput with cost-effectiveness is strengthening [Cis20; Uni22]. The available bandwidth of an optical fiber is fully utilized with the help of multiplexing schemes, which use a common transmission medium for transmitting two or more independent signals [Win09; JC19]. In OFC, the multiplexing schemes based on physical dimensions are illustrated in Figure 1.1 [WF11]. Using the frequency dimension, wavelength-division multiplexing (WDM) technologies have initially contributed to increase the data throughput by $\approx 80\%$ from the late 1990s [Tka10; WNC18]. However, the potential of WDM was fully exploited in the early 21^{st} century, resulting in the shrinkage of the overall growth rate to $\approx 20\%$ [Ess10; WF11]. Additionally, the channel capacity is increased by 2-fold with the introduction of two linear polarization directions acting as separate channels in polarization-division multiplexing (PDM) [Wil20]. In time-division multiplexing (TDM), several signals are interleaved temporally for transmission, which includes the usage of symbol rate and shape. Since a complex optical field is utilized during OFC, the amplitude and phase constitute together to generate higher-order and complex modulation schemes. In particular, all these multiplexing schemes are well-researched and deployed for commercial applications. In order to cope with the surging demand of the capacity, new methods must be investigated to aid in increasing spectral efficiency and better system performance. Therefore, the main focus of this work is on the spatial dimension.

In the last decade, the research on space-division multiplexing (SDM) intensified due to rapidly approaching Shannon's limit of single-mode fiber (SMF) based systems despite the availability of time, wavelength, or polarization as degrees of freedom [Ess10; Bai12; RFN13]. The concept of SDM for the spatially diverse channel using parallel transmission was first introduced in the late 1980s [Ina79; BF82]. The technique of using the transverse spatial extent of a multi-mode fiber and/or multi-core fiber (MMF/MCF) to create multiple

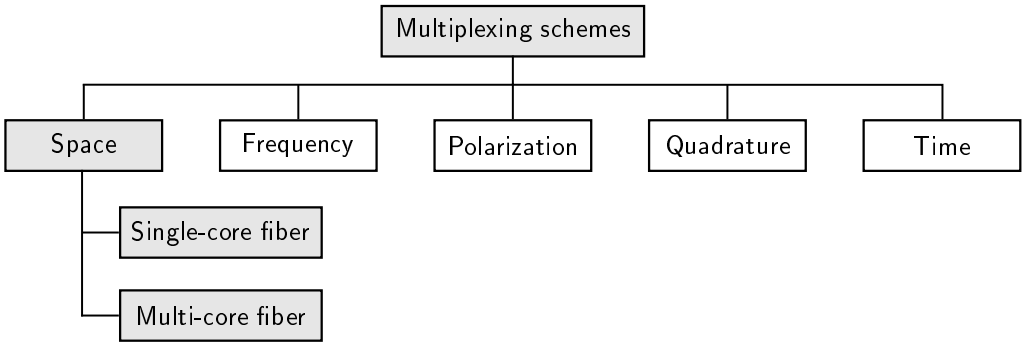

Figure 1.1.: Overview of the multiplexing schemes on the basis of physical dimensions.

parallel data channels is termed as SDM [Ell16; PSV19]. Accordingly, these transmission channels are formed with the excitation of guided modes. The concept of multiple-input and multiple-output (MIMO) can be applied to an MMF channel analogous to a wireless MIMO system, assuming the guided modes as scattering paths [Hsu06]. The advantage of an optical MIMO is to utilize modal cross-talk in an MMF channel. Moreover, mode scrambling can be mitigated using a MIMO configuration [Vel18; PSV19]. In an OFC system, single-core fibers such as MMF or few-mode fiber (FMF) are preferred over MCFs due to their lower manufacturing costs. Thus, the use of single-core fibers supporting guided modes as transmission channel is focus of the work.

An SDM-based optical system with FMF or MMF aims to propagate multiple guided modes while maintaining their orthogonality in a single-core fiber. A standard MMF with a core diameter of 50 µm can support up to 100 transverse modes at an operating wavelength of 1550 nm [Sil16; Vel18; PSV19]. Additionally, the larger core diameter of the MMFs also allows higher alignment margins [PRL21]. Ideally, all guided modes by an MMF would be translated into an individual channel. However, mode orthogonality can only be preserved for a short distance due to mode cross-talk, mode-dependent losses, and the phase difference between each mode [Zhu21]. In this work, an MMF-based optical interconnect is considered to increase the spectral efficiency and improve the system performance. Furthermore, an MMF-based intensity modulation / direct detection (IM/DD) system is utilized for cost-effectiveness and simpler implementation in short reach applications.

Coherent optical systems using SDM have achieved a record-breaking bit rate over an MMF channel using optical MIMO configurations [Ryf18; Rad21]. Ryf et al. reported a (90×90) MIMO configuration utilizing 45 spatial modes with 50 wavelength channels, achieving a 101 Tb/s data rate over a 26.5 km MMF channel [Ryf18]. Similarly, the data rate of 1 Pb/sec is attained using a 64 quadrature amplitude modulation (QAM) format and 15 spatial modes in [Rad21]. The area of coherent optical systems is well-researched for enhancing the capacity and transmission rate in a single-core MMF. However, the commercial deployment of such systems is challenging due to their high cost and greater complexity. The presence of a

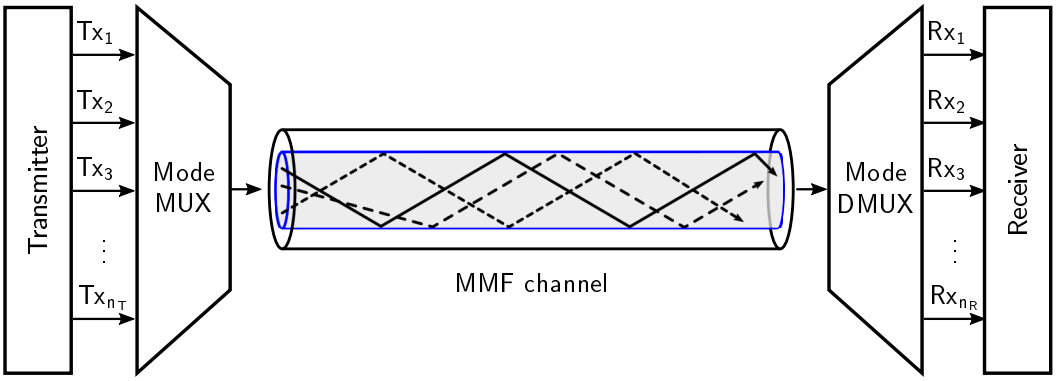

Figure 1.2.: Generalized SDM system using an MMF channel.

highly sensitive coherent receiver with carrier synchronization and controlled spectral line widths of the laser sources incur high costs. Therefore, using a cost-effective IM/DD system in short reach optical interconnects is imperative compared to a coherent system.
A generalized SDM-based optical MIMO scheme using an MMF channel is demonstrated in Figure 1.2. The parallel data streams, shown as Tx_1, Tx_2,...,$\mathrm{Tx}_{n_\mathrm{T}}$, are converted into individual spatial modes at the transmitter side with n_T denoting the number of transmitters. Ideally, each individual spatial mode is selectively excited and carried using a separate MMF. Afterwards, these parallel spatial modes are multiplexed (MUX) together into an MMF channel. Ideally, these modes are supposed to be orthogonal and should create parallel channel in an MMF. However, these modes interfere with each other and induce mode-dependent losses during the propagation. Therefore, the recovery of the transmitted data streams becomes challenging. At the receiver end, the modes are segregated using a demultiplexer (DMUX) and the data streams are detected. The challenge of an optical MIMO system is to excite a particular mode and to segregate these generated modes. Practically, solutions such as multi-plane light converters or phase plates are available in the market for selective mode excitation [Lab14; Wil15; Len16]. However, using such opto-mechanical components is proven to be expensive and increases the complexity of the system. Therefore, these solutions are inadequate for the low-cost IM/DD system with simple implementation. Offset light launching conditions from SMF to MMF are utilized in this work.

1.1. State of the Art

The principle of utilizing mode multiplexing for carrying data in a graded-index MMF was first reported in [BF82]. The feasibility of SDM, where modal dispersion was utilized to enhance the capacity of an MMF interconnect, was also demonstrated in [Stu00]. The concept of exploiting fiber modes for creating parallel data streams is analogous to multipath propagation in a wireless MIMO transmission. The offset light launching conditions

at MMFs were established in [Rad97; Rad98], which excite a subset of propagation modes to improve the bandwidth. The mode-selective excitation was advanced by using different offsets of light launching conditions from SMF to MMF [Ram81; Koo02; SXR06].
The properties of an IM/DD system using the MIMO processing technique are directed by the utilized SDM devices. According to the literature, SDM can be realized using fiber couplers, multi-plane light converters (MPLCs), and photonic lanterns [Iga18; Sil10]. While analyzing different SDM devices, the data rates are normalized with respect to the number of polarization states and wavelengths. Using fiber couplers, a (2×2) optical MIMO configuration has been demonstrated incorporating a 1 km 50/125 µm MMF at symbol frequency $f_{\mathrm{T}} = 50\,\mathrm{MHz}$ in [Stu00]. Additionally, binary phase shift keying was utilized at a data rate of $0.1\,\mathrm{Gbps/pol/}\lambda$. The SDM-enabling components were further optimized during this decade, which has resulted in investigating a 4.4 km long MMF at a data rate of $10\,\mathrm{Gbps/pol/}\lambda$ [Ste14]. Moreover, a (2×2) optical MIMO configuration combined with fiber coupler has been realized using an on-off keying (OOK) modulation format. The practical implementation of fiber couplers is limited to a (2×2) due to low mode orthogonality, which leads to cross-talk between modes. For instance, a (3×3) configuration is not yet reported while using an MMF with a 50 µm core diameter. Schollmann et al. expanded the MIMO configuration to three layers restricted to only 1 m MMF consisting of a 62.5 µm core diameter [SSR08]. Moreover, the ease of industrial compatibility and integration is challenging due to the architecture of fiber couplers [Iga18].

With the introduction of MPLC, a large number of multiplexed modes can be excited by manipulating the spatial distribution of an optical field [Bad18]. The realization of multiple orthogonal spatial modes is conducted with a succession of transverse phase profiles, which are segregated according to a specific propagation distance in a single core MMF. The working of MPLC is based on successive reflections at the phase plates and at a mirror, which offers low cross-talk and high mode selectivity. The development of MPLC has led to the implementation of MIMO configurations such as (3×3) with 1 km MMF and (4×4) over a 4.4 km MMF [Lab15; San17; San21]. Despite of the desirable mode-selectivity and minimal cross-talk properties of MPLC, the adaption of such expensive free-space SDM devices in accordance to the low-cost IM/DD systems is not yet established [Ben18; Zou20b]. Another possibility to excite different spatial modes can be conducted using photonic lanterns. However, a significant amount of cross-talk between the excited modes is present due to the excitation of multiple mode groups from each input of a photonic lantern. Mode-selectivity with a photonic lantern can be improved using dissimilar fiber cores [Sai17; Hua18]. The manufacturing complexity and high cross-talk of photonic lanterns are responsible for a limited integration into IM/DD-based optical MIMO systems [Hua18; Vel18].

1.2. Novel Contribution

This doctoral study aims to improve the system performance of a cost-effective IM/DD system with higher spectral efficiency while using an MMF channel. The novelty of this doctoral study is outlined as:

A single-input and single-output (SISO) system model is developed to improve the bit-error rate (BER) by non-uniform spacing between the constellation points, i.e., geometric constellation shaping (GCS), for IM/DD systems. The dependency of the received optical power over the noise impairments originating from the photo detector is examined. A performance comparison between a conventional equidistant constellation and a GCS-optimized non-uniform constellation is provided utilizing a higher-order pulse-amplitude modulation (PAM) format. Additionally, an experimental setup is developed to validate the relation between the noise variance and received power, highlighting the advancements due to GCS in analyzed scenarios.

A novel equalization technique, joint transceiver equalizer, is proposed to improve the BER performance in an MMF-based IM/DD system. The coefficients of a joint transceiver equalizer are computed collectively to mitigate significant impairments originating from an MMF channel. A nonlinear optimization statement with constrained maximum transmission power is applied to minimize the noise amplification due to the post-equalizer. The transmitter's complexity is limited using a few-tap pre-equalizer, and it aids in pre-compensation of the modal dispersion using multi-level signaling. The merits of utilizing a joint-transceiver scheme are verified using an experimental setup with a 250 m long MMF channel. The BER performance comparison of the proposed joint-transceiver scheme with the conventional post-equalizers is taken into account, to outline the benefits of the joint-transceiver scheme in an MMF-based SISO system.

The potential of the joint-transceiver equalizer design is extended to a (2×2) IM/DD-based optical MIMO system. A system model is developed to analyze the impact of the joint-transceiver scheme on the system performance. A mathematical optimization is formulated to calculate the transceiver scheme jointly while shifting a few post-equalizer efforts to the transmitter, enabling multi-level signaling. Afterward, an SDM-based optical MIMO experimental setup is constructed, where higher spectral efficiency is achieved using PAM-4 and a MIMO configuration. A partial joint-transceiver equalization is realized over a 250 m long MMF channel, where only one of the two MIMO inputs undergoes joint-transceiver equalization. After yielding the benefits from the partial joint-transceiver equalization design, a longer MMF channel of 1.4 km and a higher bit rate are utilized to analyze the effectiveness of the joint-transceiver equalizer. The BER performances are compared with the state-of-the-art zero-forcing (ZF) based pre- and post-equalization (PPE) filter and post-equalizers. After proving the effectiveness of the joint-transceiver equalization over a MIMO system, advanced signal processing concepts are integrated with the proposed joint-transceiver equalizer design. A parallel frame synchronization (PFS) setup is incorporated at the transmitter side

using the delay fiber, which uses only one modulator on both MIMO inputs. Thereafter, the BER performance of the joint-PPE scheme with PFS configuration is evaluated over (2×2) MIMO setup consisting of a 100 m long MMF channel. The benefits of the joint-PPE are verified using simulations and experimental setups. Moreover, the joint-PPE scheme is combined with singular valued decomposition (SVD) to yield more benefits in the MIMO configuration. Additionally, a power allocation technique is applied for optimal distribution of the transmission power over the MIMO inputs. Subsequently, the performance of the joint-transceiver combined with SVD and power allocation concepts is analyzed, demonstrating significant performance improvements.

1.3. Published Material

During the doctoral study, some parts of this work were published as conference papers or journal articles. The following overview maps the published material with the corresponding chapters and sections of this work.

[Sin21]	Section 2.5
[Sin22b]	Chapter 3
[Sin22a]	Section 4.5
[SA23]	Section 4.6
[SAL22]	Section 5.1
[SA23] & [Sin23]	Section 5.2

1.4. Outline of the Thesis

This thesis is divided into five chapters; the first is the introduction. In Chapter 2, fundamentals of an IM/DD system in short reach optical links are discussed regarding transmitter, fiber channel, and receiver. Moreover, this chapter highlights the noise mechanisms originating from the optical receiver and provides noise compensation strategies using constellation shaping. Chapter 3 focuses on implementing the proposed joint-transceiver equalizer design in an MMF-based SISO system. Chapter 4 extends the scope of the joint-PPE scheme to a MIMO system. This chapter describes the transmission system model and the calculation of the joint-PPE coefficients. Additionally, the performance of the joint-PPE is evaluated using two different MMF channels. In the last chapter, the joint-PPE scheme is implemented with PFS configuration. Moreover, SVD and power allocation techniques are also combined with the joint-PPE scheme to yield better BER performance benefits. The closing remarks of this doctoral study are provided in the summary.

2. Fundamentals of IM/DD Systems in Short Reach Optical Links

In this chapter, the fundamental architecture of light propagation through an optical fiber is described. An overview of components related to an IM/DD system is also presented in this chapter. The definition of quality criteria for a short reach optical interconnect is mentioned using the analytical and area integration method. Ultimately, compensation techniques for noise originating from the optical receiver are analyzed.

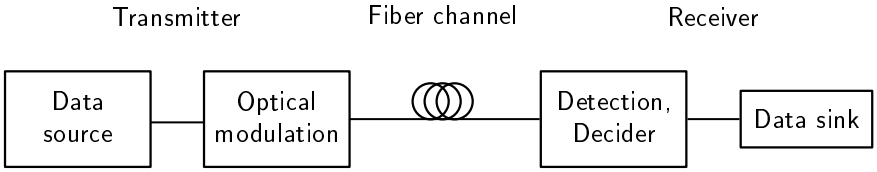

Figure 2.1.: Basic structure of an optical fiber communication link.

A fundamental structure of the OFC link is illustrated in Figure 2.1. This structure includes three major parts: transmitter, fiber channel, and receiver. The data source is presented at the transmitter, which generates the data sequences. Afterward, an optical modulator modulates a beam of light according to the provided sequence. The modulated signal then propagates through the optical fiber channel. In the last stage, the signal is detected at the receiver and undergoes signal processing such as sampling and decision. Consequently, the received signal is estimated, and the transmission link performance is evaluated. The detailed description of OFC components is discussed in the following sections.

2.1. Optical Transmitter

In an OFC link, the optical transmitter is responsible for converting the electrical signals into optical signals. Since this work focuses on low cost with stringent power and simple implementation, IM/DD systems are preferred over coherent transceivers. A laser diode with a narrow spectral width is utilized as the carrier signal, which propagates through the fiber channel. In this section, the modulator required for the intensity modulation is discussed. Additionally, the modulation format compatible with IM/DD systems are mentioned.

2.1.1. Intensity Modulation

The optical modulators are utilized to modulate the intensity of light with respect to the applied electrical signal. In this work, an external electro-optic modulator and an electro-absorption based modulator are utilized with direct detection.

Mach-Zehnder Modulators

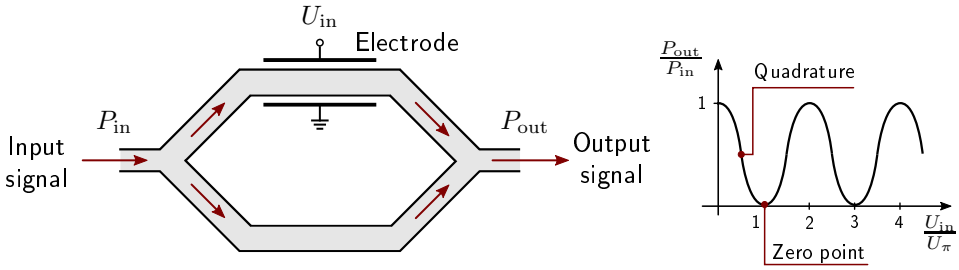

Figure 2.2.: Basic structure and transmission characteristics of an MZM.

An Mach-Zehnder modulator (MZM) operates on the Mach-Zehnder interferometric principle and Pockels effect. The basic structure of an MZM is shown in Figure 2.2. According to the provided structure, an input signal originating from a laser source is supplied to the MZM. The input signal is then divided into two equal optical paths with a 50 % splitting ratio. In order to utilize the Pockels effect, electrodes are present either on one or both of the optical paths. The phenomenon of the Pockels effect describes that the refractive index n can be modified by applying an electrical field E_{x} across the optical path. Therefore, the propagation velocity v of the light is modified due to its electromagnetic properties, which can be expressed as

$$v = \frac{2c}{(2n - \alpha_0 E_{\text{x}} \cdot n^3)} \quad , \tag{2.1}$$

where α_0 represents the Pockels coefficient and c is the speed of light [ST91]. The applied electrical field is controlled by using the voltage U_{in}. It implies that the interference between optical paths can be manipulated according to U_{in}, the applied voltage. Therefore, the output power P_{out} is dependent upon the voltage U_{in}. The transmission characteristics of an MZM are demonstrated in Figure 2.2 and are formulated as

$$\frac{P_{\text{out}}}{P_{\text{in}}} = \cos^2\left(\frac{\pi}{2}\frac{U_{\text{in}}}{U_\pi}\right) \quad , \tag{2.2}$$

with U_π denoting the half-wave voltage, i.e., the voltage required for generating a phase change of π. Figure 2.2 shows the transfer function with the bias points, such as quadrature and zero points, which should be chosen according to the application. MZMs can be constructed using the electro-optic materials such as $LiNbO_3$, GaAs and polymers [UWM15]. In this work, a MZM with $LiNbO_3$ substrate is utilized in the experimental setup.

Directly-Modulated Lasers

The directly-modulated lasers (DMLs) are semiconductor-based optical modulators. The working principle of a DML is the Franz–Keldysh effect [Fra58; LV58]. According to this effect, the absorption spectrum can be modified by changing the applied electric field. It implies that the corresponding band-gap energy is altered, which results in the modulation of the output light intensity of a laser [Liu08; LSS05]. The ability to work on low voltage while providing high bandwidth makes DML compatible to be utilized in IM/DD systems. The power-to-voltage characteristic of a DML is illustrated in Figure 2.3, where different devices are utilized for the measurement. The first and second measurement campaigns incorporate the input from a direct-current (DC) power supply and an arbitrary signal generator, respectively. Subsequently, the output power is measured by an optical power meter. In the third measurement campaign, the input voltage and the output power are measured with an arbitrary signal generator and an opto-electrical converter.

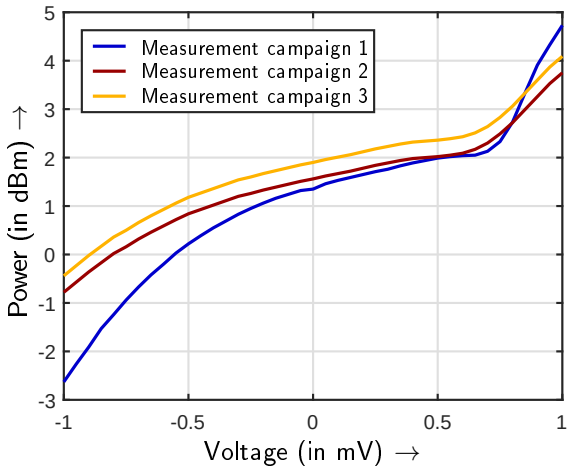

Figure 2.3.: Measured power versus voltage characteristics of a DML.

2.1.2. Modulation Formats

The primary focus of this work is on IM/DD systems as they offer lower complexity and cost-effectiveness in short reach optical fiber interconnects. The limited power budget is a significant constraint in the selection of the modulation format in such systems. Thus, the modulation format should exhibit properties such as high spectral efficiency, moderate complexity, and good sensitivity. Additionally, the data centers have restricted access in terms of utilization of equalization efforts. Considering the mentioned requirements, PAM is preferred over carrier-less amplitude phase modulation (CAP) [Olm14], discrete multi-tone (DMT) [Wei19; Zha18a], and subcarrier modulation (SCM) [Szc12] due to their better sensitivity and simple implementation.

Pulse Amplitude Modulation

For short reach optical links, an IM/DD system using a PAM format is utilized due to lower complexity and cost-effectiveness [ABP22]. Additionally, higher spectral efficiency can be achieved using a higher-order M-ary PAM format, where M is the modulation order. The constellation diagram of the PAM-M scheme with non-negative signal space is illustrated in Figure 2.4, which is plotted with quadrature Q and in-phase I components. OOK is a particular case of PAM-M, with $M = 2$ consisting of two symbols, s_0 and s_1. The symbols are illustrated over the signal space with Gray coding in Figure 2.4(b). A generalized constellation diagram of PAM-M consisting of s_m symbols with index $m = [0, 1, 2, \ldots, M-1]$ is shown in Figure 2.4(c).

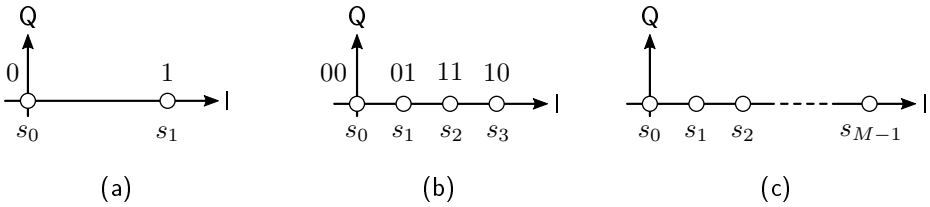

Figure 2.4.: Constellation diagrams of PAM-M format.

Considering a SISO system, the amplitude of the symbols s_m corresponds to the maximum transmit power $P_{\mathrm{s,max}}$ of the laser source. The corresponding signal amplitudes in the PAM-M scheme are defined as

$$s_m = \frac{m}{M-1} \cdot q \cdot P_{\mathrm{s,max}} \quad \text{with} \quad M \neq 1 \ , \tag{2.3}$$

where q represents the conversion factor from the electrical to the optical domain. In (2.3), the restriction over the symbol amplitudes provides an equal average transmit power irrespective of the utilized PAM-M format.

2.2. Optical Fiber Channel

The selection of an optical fiber channel is dependent upon the application area. For instance, an SMF is preferred for long-haul applications due to its low signal attenuation and dispersion properties during propagation. The capacity of an SMF is boosted using time, polarization, or wavelength as the available degree of freedom. Despite the presence of these degree of freedoms, the capacity of SMFs is approaching the Shannon limit [Bai12; RFN13; Zhu21]. Moreover, the smaller core of an SMF compared to an MMF causes sub-micron alignment tolerances. Therefore, the scope of SMF utilization in a short reach optical interconnect is limited. On the other hand, the larger core diameter of an MMF has higher alignment margins. Additionally, the larger core diameter creates a possibility to explore the

spatial degree of freedom to enable parallel data streams using SDM techniques. The parallel data streams are created by exciting different mode groups. However, the orthogonality of mode groups in an MMF can only be preserved for shorter distances. Thus, an MMF is a potential candidate for application in an IM/DD system for short reach optical links over an SMF due to its higher spectral efficiency, cost-effectiveness, and simple implementation.

2.2.1. Multi-Mode Fiber Structure

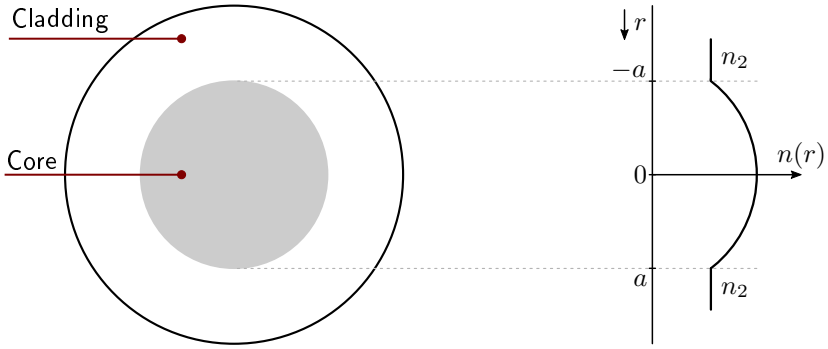

Figure 2.5.: Cross-sectional view and parabolic refractive index of a multi-mode graded-index optical fiber.

The MMFs are categorized into step-index and graded-index fibers according to the fiber structure. In a step-index fiber, the refractive index of the core n_1 is constant in the core region and directly changes to a lower refractive index value at the boundary of the core and cladding. The refractive index of the cladding n_2 is uniform in the cladding region of the step-index fiber. The structure of a graded-index fiber consists of a gradually decreasing refractive index from the center of the core to the boundary of the cladding. A graded-index fiber exhibits the characteristic of an infinite parabolic refractive index profile, which is demonstrated in Figure 2.5. The radial refractive index distribution $n(r)$ changes with the radius r and is approximated as

$$n^2(r) = n_1^2 \left[1 - 2\Delta \left(\frac{r}{a}\right)^2\right] \quad , \tag{2.4}$$

with Δ describing the normalized difference between the refractive indices of the core $n_1 = n(0)$, the cladding $n_2 = n(a)$ and a is the core radius [Ung84; CC01]. The parameter Δ is defined as

$$\Delta \approx \frac{n_1 - n_2}{n_1} \quad . \tag{2.5}$$

The description of light propagation in an optical fiber can be explained with several theories, such as geometrical-ray theory, quantum theory, and electromagnetic mode theory. The latter model is selected for the improved modal analysis in the graded-index MMFs. The

modal field distributions are approximated with the help of Maxwell's wave equations under the boundary conditions of a graded-index MMF [Ung84]. The wave equation of the weakly guided fibers for the linearly polarized electrical field component E_x in the x-direction is represented by

$$\Delta E_x + n^2(r) k_0^2 E_x = 0 \ , \tag{2.6}$$

where k_0 is the free-space wave number. The solution of the scalar wave equation in (2.6) is calculated in the cylindrical coordinate system for taking advantage of cylindrical symmetry of the fiber, which is given as

$$E_x(r, \phi, z) = \psi_{ml}(r) \cdot \left\{ \begin{array}{c} \cos(m\phi) \\ \sin(m\phi) \end{array} \right\} \cdot \exp(-\mathrm{j}\beta_{ml} z) \ , \tag{2.7}$$

where ϕ and z are the cylindrical polar coordinates denoting the transversal plane and the direction of the fiber. Variables ψ and β are the radial electrical field distribution and the propagation constant. The integer m is the selected azimuthal index with $m \in \mathbb{Z}^+$, and the radial index is denoted by l with $l \in \mathbb{N}^+$. The wave equation solutions are unique with every single combination of m and l. These solutions are termed as fiber modes, consisting of a distinct electrical field pattern. The terms $\cos(m\phi)$ and $\sin(m\phi)$ describe the periodic dependency on the azimuthal index in the circumferential direction. The fiber modes in the x-direction are named as linearly-polarized (LP) modes. Moreover, the cosine and sine modes are produced for m and l indices, which are represented by $\mathrm{LP}_{ml,a}$ and $\mathrm{LP}_{ml,b}$ modes, respectively. The radial distribution of the electric field $\psi_{ml}(r)$ for the parabolic profile of a graded-index MMF is calculated as

$$\psi_{ml}(r) = \sqrt{\frac{(l-1)!}{(l+m-1)!} \cdot \frac{2}{\pi}} \cdot \frac{1}{\omega_0} \left(\frac{\sqrt{2} r}{\omega_0} \right)^m \cdot L_{l-1}^{(m)} \left(\frac{2r^2}{\omega_0^2} \right) \cdot \exp\left(\frac{-r^2}{\omega_0^2} \right) \ , \tag{2.8}$$

with $L_l^{(m)}(x)$ denoting the Laguerre polynomial and ω_0 is the mode field radius [Ung84]. The mode field radius is given by

$$\omega_0 = \sqrt{\frac{2}{V}} \cdot a \ , \tag{2.9}$$

where V is the V-number representing the normalized frequency parameter. The generalized Laguerre polynomial of m-th order and l-th degree is defined as

$$L_l^{(m)}(x) = \sum_{v=0}^{l} \left(\begin{array}{c} l+m \\ l-v \end{array} \right) \cdot \frac{(-x)^v}{v!} \ . \tag{2.10}$$

The mode group index [Ung84] can be calculated as follows

$$\text{Mode group index} = 2l + m - 1 \ . \tag{2.11}$$

The generated LP mode with respect to the mode groups is mentioned in Table 2.1. The

Table 2.1.: LP modes categorized according to their respective mode groups.

Mode groups	LP modes
MG_0	LP_{01}
MG_1	LP_{11a} LP_{11b}
MG_2	LP_{21a} LP_{21b} LP_{02}
MG_3	LP_{12a} LP_{12b} LP_{31a} LP_{31b}
MG_4	LP_{22a} LP_{22b} LP_{41a} LP_{41b} LP_{03}

intensity patterns of different modes are also demonstrated in Figure 2.6. When these modes are excited, they generate spatial diversity in a fiber [GN89]. Subsequently, these excited modes are responsible for creating parallel data streams. A total of 100 transverse modes are supported by an MMF, which could be used as data channels [PSV19]. The challenge is to excite specific modes and to maintain the orthogonality of these modes through transmission while restraining the cost and simple implementation of an IM/DD system.

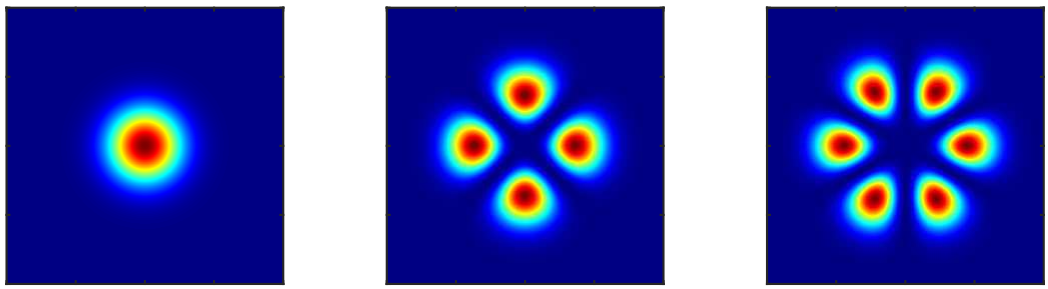

(a) LP_{01} mode (b) LP_{21} mode (c) LP_{31} mode

Figure 2.6.: Simulated intensity pattern of ideal LP modes.

2.2.2. Mode Excitation and Coupling

In this work, the selective mode-excitation is executed using restricted light launching conditions from SMF to MMF with a radial offset to a fiber core. In Figure 2.7, the core of the SMF is aligned either to the center or with a radial offset to the MMF core. In [Ram81], the power coupling efficiency of the mode number m and l between the incident mode and specific mode guided into the MMF can be expressed as the function of respective electrical

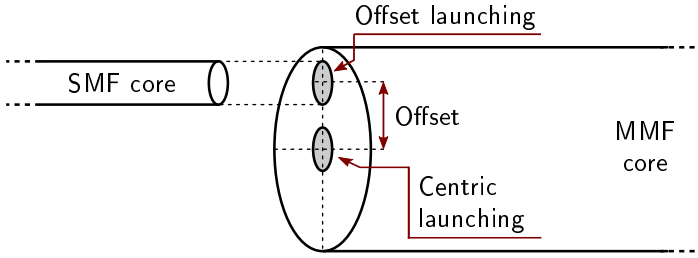

Figure 2.7.: Restricted SMF to MMF launch positions with centric and offset launching conditions for mode-selective excitation.

fields, which is given as

$$c_{l,m} = \frac{\left| \iint_{-\infty}^{+\infty} E_{\text{in}}(x,y)\, E_{ml}^{*}(x,y)\, \mathrm{d}x\, \mathrm{d}y \right|^2}{\iint_{-\infty}^{+\infty} E_{\text{in}}(x,y)\, E_{\text{in}}^{*}(x,y)\, \mathrm{d}x\, \mathrm{d}y \cdot \iint_{-\infty}^{+\infty} E_{ml}(x,y)\, E_{ml}^{*}(x,y)\, \mathrm{d}x\, \mathrm{d}y} \quad , \tag{2.12}$$

where $E_{\text{in}}(x,y)$ and $E_{ml}(x,y)$ represent the incident and mode-specific electric fields, respectively. The operator $(\cdot)^*$ denotes the complex conjugate operation. The restricted launching conditions are applied to excite several mode groups, where each mode group can ideally be considered as a parallel data stream [App13]. Theoretically, a standard OM4 grade 50 µm core MMF, identified by ISO11801, can support up to 55 modes per polarization. In graded-index MMF with a parabolic profile, these modes are arranged into 10 degenerated mode groups. The LP_{ml} modes belonging to the same groups, as shown in Table 2.1, are more likely to couple together due to their identical propagation constant [CES13]. The studies on mode excitation and coupling demonstrate the usage of restricted launch conditions, excitation of different modes, and different spot sizes of an incident electric field [XR05; BF82; App13]. The restricted light launching from SMF to MMF offers low-cost and simple implementation compared to MPLC and other SDM devices. Thus, the restricted light launching with a radial offset to an MMF is incorporated in this work.

2.2.3. Dispersion Mechanisms

The optical fibers are well-suited to meet the requirements of high bandwidth in OFC links. However, the dispersion impairments are the limiting factor for the bandwidth-length product. These dispersion mechanisms are categorized into linear and non-linear effects. The linear dispersion impairments include chromatic, mode and polarization dispersion effects, which have a linear effect on the transmitted signal. On the other hand, the non-linear dispersion effects, such as self-phase modulation, cross-phase modulation, four-wave mixing, or stimulated Raman/Brillouin scattering, lead to non-linear influences. The relation of fiber losses dependent on the used wavelength is illustrated in Figure 2.8a. The minimum

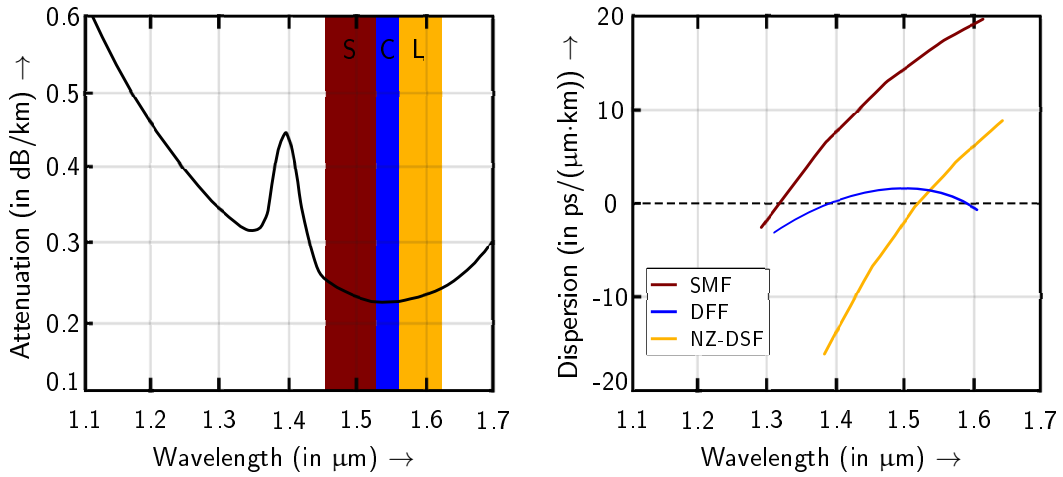

(a) Attenuation versus wavelength

(b) Dispersion versus wavelength

Figure 2.8.: Fiber losses and total dispersion dependency on the wavelength.

attenuation of $\approx 0.2\,\mathrm{dB/km}$ is reported at a wavelength of 1550 nm. The second minimum value of attenuation can be found at 1310 nm. In Figure 2.8a, three transmission windows are labeled, such as S is from 1460 nm to 1530 nm, C is from 1530 nm to 1565 nm, and L is from 1565 nm to 1625 nm, which are commonly utilized in the lightwave systems [Agr02; Szc13; SSB08].

The dispersion depending upon the wavelength is demonstrated in Figure 2.8b. The total dispersion D of a standard single-mode optical fiber includes the material D_M and waveguide D_W dispersion mechanisms, which is expressed as

$$D = D_\mathrm{M} + D_\mathrm{W} \ . \tag{2.13}$$

The material dispersion D_M at a wavelength λ, which is oscillating at frequency ω, is described as

$$D_\mathrm{M} = \frac{2\pi}{\lambda^2}\frac{\mathrm{d}n_{2\mathrm{g}}}{\mathrm{d}\omega} \ , \tag{2.14}$$

with $n_{2\mathrm{g}}$ denoting the group index of the cladding material [Agr02]. Additionally, the waveguide dispersion is given as

$$D_\mathrm{W} = \frac{2\pi\Delta}{\lambda^2}\left(\frac{n_{2\mathrm{g}}^2}{\omega\, n_2}\frac{V\mathrm{d}(Vb)}{\mathrm{d}V^2} + \frac{\mathrm{d}n_{2\mathrm{g}}}{\mathrm{d}\omega}\frac{d(Vb)}{\mathrm{d}V}\right) \ , \tag{2.15}$$

where b is the normalized propagation constant and the V is the cut-off parameter. These parameters are formulated as

$$V = \left(\frac{2\pi}{\lambda}\right) a\, n_1\sqrt{2\Delta} \quad \text{and} \quad b = \frac{\tilde{n} - n_2}{n_1 - n_2} \ . \tag{2.16}$$

In (2.16), $\tilde{n}$ is the effective refractive index of a mode, and a is the core radius [Agr02]. The zero dispersion (ZD) point is located at approximately 1310 nm. The typical value of dispersion at 1550 nm is from 15-18 ps/(nm·km). The contribution of waveguide dispersion is dependent upon the core radius and the refractive index difference Δ. Therefore, the ZD point can be shifted, and these fibers are known as dispersion-shifted fibers (DSFs) [Agr02; SSB08]. Moreover, the fibers can be tailored in such a way that the response of the fiber dispersion is nearly constant for a range of frequencies. These fibers are known to be dispersion-flattened fibers (DFFs).
In an optical system with an MMF, the propagated light generates several modes with different group velocities, which is termed as modal dispersion. The mode coupling effect occurs when different propagation modes superposition with each other due to core eccentricity or bends, causing inter-symbol interference (ISI) and limiting the fiber bandwidth [SK09]. The power-coupling models have been reported in the literature, where the dependency of mode power over the fiber length is reported [Ols75; KSU80]. Additionally, transmission models on pulse broadening with graded-index MMFs have also been introduced [OK76]. However, the concept of modal dispersion provides an aid in an optical MIMO configuration, where different modes ideally act as parallel data streams.

2.3. Optical Receiver

In fiber-optic transmission, the fundamental role of an optical receiver is to convert the incident light into electric current utilizing a photodetector. Additionally, the optical receivers perform amplification and recovery of the received signal. Therefore, the efficacy of an optical receiver dictates the performance of a fiber-optics transmission link. The basic principle of optical-electrical conversion is the photoelectric effect. The essential characteristics of an optical receiver should include low noise, high reliability, low cost, high sensitivity, and optical linearity at the operating wavelength. The semiconductor photodetectors are preferred due to their compatibility with the fiber-core size, better performance, and high cost-effectiveness [Agr02; M J14].

In optical communication, the receiver can be configured either for direct or coherent detection depending upon the application. Direct detection involves the conversion of only the incident optical power into an electrical signal, and the phase as well as frequency information is not obtained. On the contrary, the output electrical signal using coherent detection consists of amplitude as well as phase information. The complexity of the receiver increases due to transceiver carrier synchronization. Considering the short reach optical links with PAM formats, where the low cost and simple implementation are crucial factors, the optical receivers with direct detection system are preferred. The main challenge in an optical direct detection system is to accurately recover the temporal characteristics of the input signal while minimizing the noise due to the photo detection process and an amplifier.

2.3.1. Direct Detection with Square-Law Detector

A direct detection system is based on detecting the modulated optical intensity. A solid-state photodiode is utilized in these systems with a corresponding transmitter structure, which modulates only the optical power. The most commonly used photo diodes for OFC are PIN-diodes, avalanche diodes, and high-speed detectors. The PIN photodiode is typically deployed in the IM/DD system due to their cost-effectiveness and lower complexity. A simplified structure of a PIN diode consists of an intrinsic material between the p-n doped regions. The advantage of having such a structure is the presence of a strong electric field due to a high resistance voltage drop across the intrinsic region [Agr02]. The relationship between incident power P_s and average output current I_p is formulated as

$$I_\mathrm{p} = \Re P_\mathrm{s} \ , \tag{2.17}$$

with $\Re$ denoting the responsivity of the PIN diode. The detection process is considered to be the square-law process. Subsequently, incident power is proportional to the square of the electrical field. The detection process is aided by a transimpedance amplifier to convert the current into voltage. Considering a detector with a surface area of D, the output voltage u with respect to the incident electric field is calculated as

$$u = C \iint\limits_{D} \left| E_\mathrm{in}(x, y, z_0) \right|^2 \mathrm{d}x \, \mathrm{d}y \ , \tag{2.18}$$

where $E_\mathrm{in}(x, y, z_0)$ is the incident electric field in Cartesian coordinates, z_0 is the location of detector surface and C is the conversion factor including responsivity and transimpedance [San21].

2.3.2. Noise Impairments

The conversion process of an incident optical power into current in (2.17) is ideally considered to be noise free. However, noise impairments still occur at the optical receiver due to current fluctuations or thermal agitation of electrons [Sim20; Bot08]. The system performance of the transmission is limited due to the presence of these noise mechanisms. The two fundamental noise impairments that prevail in all optical receivers are shot noise and thermal noise.

Shot Noise

The existence of shot noise was studied by Schottky in 1918 [Sch18] and was related to the photon absorption in a photodetector. However, [RMY91] proved that the occurrence of the shot noise is due to the manifestation of the quantum nature of light rather than an aftereffect of the photodetector. The shot noise originates during the optical absorption process. The statistical fluctuations in photocurrent at a specific time interval between

photon absorption and electron-hole pair generation result in shot noise [Agr02; GP60]. The photocurrent variance due to shot noise σ_{sh}^2 is defined by

$$\sigma_{\mathrm{sh}}^2 = 2q_0\big(i(t) + I_{\mathrm{d}}\big)B \ , \tag{2.19}$$

where q_0 is the elementary charge, $i(t)$ is the generated photocurrent dependent upon the time instance t, dark current is I_{d}, and B represents the effective noise bandwidth of the receiver. The photocurrent fluctuations due to shot noise are modeled by the Poisson probability distribution function with a white power spectral density. However, the shot noise variance is often approximated by Gaussian statistics.

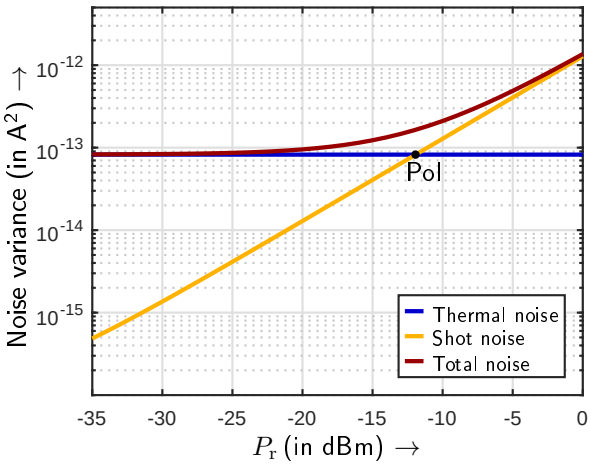

Figure 2.9.: Noise variance depending upon average optical received power, where PoI is labeled as the point of intersection.

Thermal Noise

In passive-resistive components, random thermal motion is exhibited at a finite temperature, which leads to the current fluctuations. The thermal noise variance σ_{th}^2 utilizing a feedback resistance R_{f} connected to the photodetector is given by

$$\sigma_{\mathrm{th}}^2 = \frac{4k_{\mathrm{B}}TBF_{\mathrm{n}}}{R_{\mathrm{f}}} \ , \tag{2.20}$$

where k_{B} is the Boltzmann constant, F_{n} relates to the noise figure of an optical amplifier, and T is the absolute temperature. Thermal noise is commonly called as Nyquist noise or Johnson noise [ST91]. The thermal noise is described as a Gaussian random process consisting of frequency-independent spectral density.

The current fluctuations due to shot noise and thermal noise, as mentioned in (2.19) and (2.20), are independent random mechanisms. Therefore, the total variance of fluctuations is obtained by simply adding these two Gaussian approximated process. The resulting variance

due to shot noise and thermal noise is represented as

$$\sigma^2_{\text{total}} = \sigma^2_{\text{sh}} + \sigma^2_{\text{th}} = 2q_0\big(i(t) + I_{\text{d}}\big)B + \frac{4k_{\text{B}}TBF_{\text{n}}}{R_{\text{f}}} \quad . \tag{2.21}$$

An optical receiver is parameterized with $B = 5\,\text{GHz}$, $R_{\text{f}} = 1\,\text{k}\Omega$, $\Re = 0.8\,\text{A/W}$, $I_{\text{d}} = 50\,\text{nA}$ and $T = 298\,\text{K}$. The dependency of noise variances on the average optical received power P_{r} is presented in Figure 2.9, where PoI describes the point of intersection between the shot noise and thermal noise. The PoI segregates the P_{r} area into a shot noise dominant region with $P_{\text{r}} >$ PoI and a thermal noise dominant region with $P_{\text{r}} \leq$ PoI. From Figure 2.9, it is evident that the shot noise variance strengthens with the increase in P_{r}. Furthermore, the thermal noise variance remains constant irrespective of P_{r}. In the shot noise dominant region, all the symbols are affected by distinct noise variances depending upon the generated photocurrent with each symbol amplitude. When $P_{\text{r}} \leq$ PoI, the thermal noise dominant region will result in a similar noise variance of all the symbols.

2.3.3. Post Equalization Techniques

The interference originating from the channel degrades the system performance. Additionally, the interference between the transmission channels produces inter-channel interference (ICI) in a MIMO configuration. The frequency-selective channel causes ISI, which is the interference between the neighboring symbols. The equalization techniques are utilized to mitigate these interferences. Generally, the equalization is present on the receiver side. However, the presence of a transceiver equalization has proven to be beneficial compared to an equalization existing either at the transceiver or the receiver [Raj19; Zha21]. Currently available are equalization strategies based on orthogonal frequency division multiplexing, spatio-temporal vector coding, linear and adaptive methods. In this work, the focus is on linear equalizers based on ZF and minimum mean square error (MMSE) principles. The selection of these equalization methods is conducted due to their comprehensive implementation, simple realization, and analytical traceability [Agr02; Zhu21].

Zero-forcing Equalization

A standard system model with a MIMO channel and a linear equalizer is demonstrated in Figure 2.10. The system model is provided in matrix notation, which can be transformed into a SISO model by assuming the number of MIMO inputs n_{T} and outputs n_{R} to be one. The transmit signal vector $\boldsymbol{s}[k]$ is given as

$$\boldsymbol{s}[k] = \begin{pmatrix} s_1[k] & s_2[k] \ \ldots \ s_{n_{\text{T}}}[k] \end{pmatrix}^{\text{T}} \quad , \tag{2.22}$$

with $(n_{\text{T}} \times 1)$ dimensions and $k \in \mathbb{Z}$. The number of MIMO inputs and outputs are defined as $\mu = [1, 2, \ldots, n_{\text{T}}]$ and $\nu = [1, 2, \ldots, n_{\text{R}}]$, respectively. The notation of square brackets,

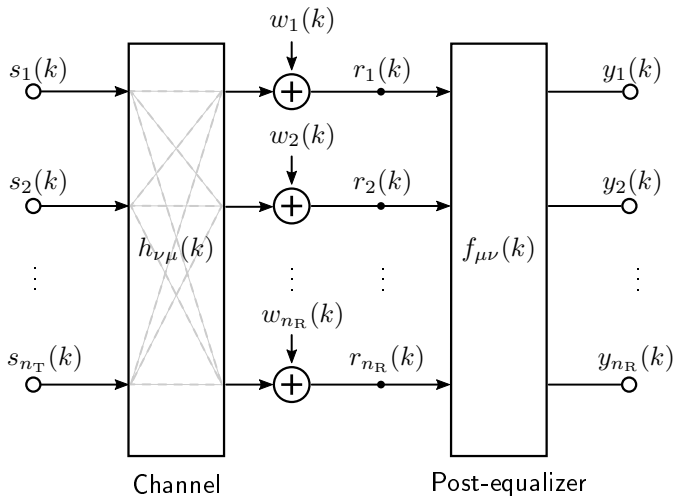

Figure 2.10.: Standard discrete system model with MIMO channel and linear equalizer.

e.g. $s_1[k]$, denotes the k-th element of the series and the round brackets, e.g. $s(k)$, refers to all elements of a series. A $(n_\mathrm{R} \times n_\mathrm{T})$ frequency-selective channel is expressed as

$$\boldsymbol{H}[k] = \begin{pmatrix} h_{11}[k] & \cdots & h_{1n_\mathrm{T}}[k] \\ \vdots & \ddots & \vdots \\ h_{n_\mathrm{R}1}[k] & \cdots & h_{n_\mathrm{R}n_\mathrm{T}}[k] \end{pmatrix} \quad . \tag{2.23}$$

The noise signal vector of size $(n_\mathrm{R} \times 1)$ is defined as

$$\boldsymbol{w}[k] = (w_1[k] \quad w_2[k] \ldots w_{n_\mathrm{R}}[k])^\mathrm{T} \quad . \tag{2.24}$$

Subsequently, a $(n_\mathrm{R} \times 1)$ received signal vector is given as

$$\boldsymbol{r}[k] = (r_1[k] \quad r_2[k] \ldots r_{n_\mathrm{R}}[k])^\mathrm{T} \quad . \tag{2.25}$$

According to Figure 2.10, the received signal vector can be described as

$$\begin{pmatrix} r_1[k] \\ \vdots \\ r_{n_\mathrm{R}}[k] \end{pmatrix} = \sum_{i=0}^{L_\mathrm{h}-1} \begin{pmatrix} h_{11}[i] & \cdots & h_{1n_\mathrm{T}}[i] \\ \vdots & \ddots & \vdots \\ h_{n_\mathrm{R}1}[i] & \cdots & h_{n_\mathrm{R}n_\mathrm{T}}[i] \end{pmatrix} \cdot \begin{pmatrix} s_1[k-i] \\ \vdots \\ s_{n_\mathrm{T}}[k-i] \end{pmatrix} + \begin{pmatrix} w_1[k] \\ \vdots \\ w_{n_\mathrm{R}}[k] \end{pmatrix} \quad , \tag{2.26}$$

where L_h is the number of channel coefficients. The matrix notation for the given MIMO system model is

$$\boldsymbol{r}[k] = \sum_{i=0}^{L_\mathrm{h}-1} \boldsymbol{H}[i] \cdot \boldsymbol{s}[k-i] + \boldsymbol{w}[k] \quad . \tag{2.27}$$

When an equalizer is incorporated into the MIMO model with a finite number of feed-forward equalizer coefficients L_f, the system description in (2.27) is expanded as

$$\boldsymbol{r}[k] = (\boldsymbol{H}[0] \quad \boldsymbol{H}[1] \ldots \boldsymbol{H}[L_\mathrm{h}-1]) \cdot \begin{pmatrix} \boldsymbol{s}[k] \\ \boldsymbol{s}[k-1] \\ \vdots \\ \boldsymbol{s}[k-L_\mathrm{h}+1] \end{pmatrix} + \boldsymbol{w}[k] \ . \tag{2.28}$$

Considering the past instances of the received signal, the equations are summarized as

$$\begin{pmatrix} \boldsymbol{r}[k] \\ \boldsymbol{r}[k-1] \\ \vdots \\ \boldsymbol{r}[k-L_\mathrm{f}+1] \end{pmatrix} = \boldsymbol{H}_\mathrm{V} \cdot \begin{pmatrix} \boldsymbol{s}[k] \\ \boldsymbol{s}[k-1] \\ \vdots \\ \boldsymbol{s}[k-L_\mathrm{h}-L_\mathrm{f}+2] \end{pmatrix} + \begin{pmatrix} \boldsymbol{w}[k] \\ \boldsymbol{w}[k-1] \\ \vdots \\ \boldsymbol{w}[k-L_\mathrm{f}+1] \end{pmatrix} \ , \tag{2.29}$$

where

$$\boldsymbol{H}_\mathrm{V} = \begin{pmatrix} \boldsymbol{H}[0] & \boldsymbol{H}[1] & \boldsymbol{H}[2] & \ldots & \boldsymbol{H}[L_\mathrm{h}-1] & \boldsymbol{0} & \ldots & \boldsymbol{0} \\ \boldsymbol{0} & \boldsymbol{H}[0] & \boldsymbol{H}[1] & \ldots & \boldsymbol{H}[L_\mathrm{h}-2] & \boldsymbol{H}[L_\mathrm{h}-1] & \ldots & \boldsymbol{0} \\ \boldsymbol{0} & \boldsymbol{0} & \boldsymbol{H}[0] & \ldots & \boldsymbol{H}[L_\mathrm{h}-3] & \boldsymbol{H}[L_\mathrm{h}-2] & \ldots & \boldsymbol{0} \\ \vdots & \vdots & \vdots & \ddots & \vdots & \vdots & \ddots & \vdots \\ \boldsymbol{0} & \boldsymbol{0} & \boldsymbol{0} & \ldots & \ldots & \ldots & \ldots & \boldsymbol{H}[L_\mathrm{h}-1] \end{pmatrix} \ . \tag{2.30}$$

In (2.30), $\boldsymbol{0}$ is the $(n_\mathrm{R} \times n_\mathrm{T})$ zero matrix and the overall system model is as follows

$$\underset{(n_\mathrm{R}L_\mathrm{f}\times 1)}{\boldsymbol{r}_\mathrm{V}} = \underset{(n_\mathrm{R}L_\mathrm{f}\times n_\mathrm{T}(L_\mathrm{f}+L_\mathrm{h}-1))}{\boldsymbol{H}_\mathrm{V}} \cdot \underset{(n_\mathrm{T}(L_\mathrm{f}+L_\mathrm{h}-1)\times 1)}{\boldsymbol{s}_\mathrm{V}} + \underset{(n_\mathrm{R}L_\mathrm{f}\times 1)}{\boldsymbol{w}_\mathrm{V}} \ . \tag{2.31}$$

When a linear equalizer of $(n_\mathrm{T} \times n_\mathrm{R})$ matrix is applied to the received signal vector, which is given as

$$\boldsymbol{F}[k] = \begin{pmatrix} f_{11}[k] & \cdots & f_{1n_\mathrm{R}}[k] \\ \vdots & \ddots & \vdots \\ f_{n_\mathrm{T}1}[k] & \cdots & f_{n_\mathrm{T}n_\mathrm{R}}[k] \end{pmatrix} \ , \tag{2.32}$$

and

$$\boldsymbol{y}[k] = \sum_{m=0}^{L_\mathrm{f}-1} \boldsymbol{F}[m] \cdot \boldsymbol{r}[k-m] \ . \tag{2.33}$$

Additionally, the matrix multiplication results in

$$\boldsymbol{y}[k] = (\boldsymbol{F}[0] \quad \boldsymbol{F}[1] \ldots \boldsymbol{F}[L_\mathrm{f}-1]) \cdot \begin{pmatrix} \boldsymbol{r}[k] \\ \boldsymbol{r}[k-1] \\ \vdots \\ \boldsymbol{r}[k-L_\mathrm{f}+1] \end{pmatrix} \quad . \tag{2.34}$$

Consequently, substituting (2.29) into (2.34) results in

$$\boldsymbol{y}[k] = \boldsymbol{F}_\mathrm{V} \cdot \boldsymbol{H}_\mathrm{V} \cdot \begin{pmatrix} \boldsymbol{s}[k] \\ \boldsymbol{s}[k-1] \\ \vdots \\ \boldsymbol{s}[k-L_\mathrm{h}-L_\mathrm{f}+2] \end{pmatrix} + \boldsymbol{F}_\mathrm{V} \cdot \begin{pmatrix} \boldsymbol{w}[k] \\ \boldsymbol{w}[k-1] \\ \vdots \\ \boldsymbol{w}[k-L_\mathrm{f}+1] \end{pmatrix} \quad , \tag{2.35}$$

In order to recover the transmit signal vector$\boldsymbol{s}$ by removing the interferences, the following conditions should be fulfilled

$$\boldsymbol{F}_\mathrm{V} \cdot \boldsymbol{H}_\mathrm{V} = \boldsymbol{Z} \quad , \tag{2.36}$$

where $\boldsymbol{Z}$ is the Nyquist matrix. The system is transformed into non-interfering transmission layers with the help of the post-equalization. Therefore, the ZF design of the post-equalizer is given as

$$\boldsymbol{F}_\mathrm{V} = \boldsymbol{Z}\boldsymbol{H}_\mathrm{V}^\mathrm{H} \left(\boldsymbol{H}_\mathrm{V}\boldsymbol{H}_\mathrm{V}^\mathrm{H}\right)^{-1} \quad , \tag{2.37}$$

with $(\cdot)^\mathrm{H}$ denoting the transpose and complex conjugate matrix or Hermitian operator. Moreover, the noise enhancement due to the post-equalizer is neglected in the ZF principle [Pro08]. Thus, an MMSE principle is also implemented in which the noise influence is considered to improve the transmission quality. Throughout this work, when the post-equalization is applied with ZF or MMSE principle, it is denoted as PE-ZF and PE-MMSE, respectively. Please note that the pre-equalization is not utilized in the case of PE-ZF and PE-MMSE.

Minimum Mean Square Error Equalizer

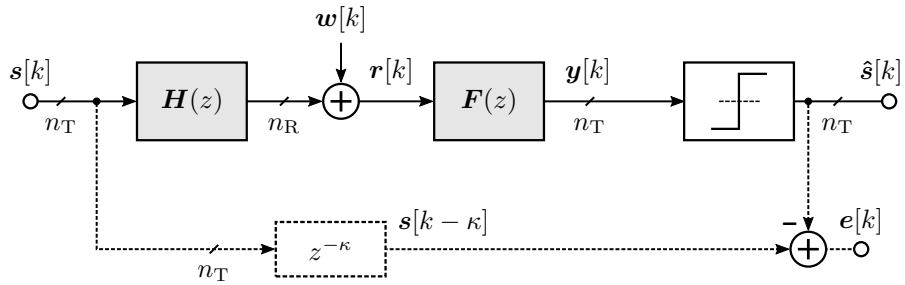

Figure 2.11.: MIMO channel with an MMSE equalizer system model.

A general system model incorporating a feed-forward MMSE equalizer $\boldsymbol{F}(z)$ is illustrated in Figure 2.11. In this system model, the equalization concept aims to compare the MIMO input symbol vector $\boldsymbol{s}[k]$ at the k-th instance with the estimated symbols $\boldsymbol{y}[k]$ at the receiver side. Correspondingly, achieving a minimum value of the mean square error of the error vector $\boldsymbol{e}[k]$. The signal vectors $\boldsymbol{s}[k]$ and $\boldsymbol{y}[k]$ are synchronized using the delay block $z^{-\kappa}$, where $\boldsymbol{s}[k]$ is delayed by κ symbols due to the channel. The MIMO frequency-selective channel is represented by $H(z)$. The received signal vector in matrix notation can be defined as

$$\boldsymbol{r}_{\mathrm{V}} = \boldsymbol{H}_{\mathrm{V}} \cdot \boldsymbol{s}_{\mathrm{V}} + \boldsymbol{w}_{\mathrm{V}} \ . \tag{2.38}$$

The auto-correlation functions of the input signal vector is

$$\boldsymbol{R}_{ss} = \mathrm{E}\left\{\boldsymbol{s}_{\mathrm{V}} \boldsymbol{s}_{\mathrm{V}}^{\mathrm{H}}\right\} \ , \tag{2.39}$$

and the noise auto-correlation is

$$\boldsymbol{R}_{ww} = \mathrm{E}\left\{\boldsymbol{w}_{\mathrm{V}} \boldsymbol{w}_{\mathrm{V}}^{\mathrm{H}}\right\} \ . \tag{2.40}$$

The cross-correlation between input and output is given as

$$\begin{aligned} \boldsymbol{R}_{sr} &= \mathrm{E}\left\{\boldsymbol{s}_{\mathrm{V}} \boldsymbol{r}_{\mathrm{V}}^{\mathrm{H}}\right\} \\ &= \mathrm{E}\left\{\boldsymbol{s}_{\mathrm{V}} \left(\boldsymbol{H}_{\mathrm{V}} \boldsymbol{s}_{\mathrm{V}} + \boldsymbol{w}_{\mathrm{V}}\right)^{\mathrm{H}}\right\} \\ &= \mathrm{E}\left\{\boldsymbol{H}_{\mathrm{V}}^{\mathrm{H}} \boldsymbol{s}_{\mathrm{V}} \boldsymbol{s}_{\mathrm{V}}^{\mathrm{H}} + \boldsymbol{s}_{\mathrm{V}} \boldsymbol{w}_{\mathrm{V}}^{\mathrm{H}}\right\} \\ &= \mathrm{E}\left\{\boldsymbol{H}_{\mathrm{V}}^{\mathrm{H}} \boldsymbol{s}_{\mathrm{V}} \boldsymbol{s}_{\mathrm{V}}^{\mathrm{H}}\right\} + \mathrm{E}\left\{\boldsymbol{s}_{\mathrm{V}} \boldsymbol{w}_{\mathrm{V}}^{\mathrm{H}}\right\} \\ &= \mathrm{E}\left\{\boldsymbol{s}_{\mathrm{V}} \boldsymbol{s}_{\mathrm{V}}^{\mathrm{H}}\right\} \boldsymbol{H}_{\mathrm{V}}^{\mathrm{H}} \\ &= \boldsymbol{R}_{ss} \boldsymbol{H}_{\mathrm{V}}^{\mathrm{H}} \ , \end{aligned} \tag{2.41}$$

where the cross-correlation between the input signal vector and noise vector $\mathrm{E}\left\{\boldsymbol{s}_{\mathrm{V}} \boldsymbol{w}_{\mathrm{V}}^{\mathrm{H}}\right\}$ is considered to be zero and $(\cdot)^{\mathrm{H}}$ is a transpose complex conjugate matrix. The auto-correlation of the received signal is defined as

$$\begin{aligned} \boldsymbol{R}_{rr} &= \mathrm{E}\left\{\boldsymbol{r}_{\mathrm{V}} \boldsymbol{r}_{\mathrm{V}}^{\mathrm{H}}\right\} \\ &= \mathrm{E}\left\{\left(\boldsymbol{H}_{\mathrm{V}} \boldsymbol{s}_{\mathrm{V}} + \boldsymbol{w}_{\mathrm{V}}\right) \left(\boldsymbol{H}_{\mathrm{V}} \boldsymbol{s}_{\mathrm{V}} + \boldsymbol{w}_{\mathrm{V}}\right)^{\mathrm{H}}\right\} \\ &= \mathrm{E}\left\{\boldsymbol{H}_{\mathrm{V}} \boldsymbol{s}_{\mathrm{V}} \boldsymbol{s}_{\mathrm{V}}^{\mathrm{H}} \boldsymbol{H}_{\mathrm{V}}^{\mathrm{H}} + \boldsymbol{H}_{\mathrm{V}} \boldsymbol{s}_{\mathrm{V}} \boldsymbol{w}_{\mathrm{V}}^{\mathrm{H}} + \boldsymbol{H}_{\mathrm{V}}^{\mathrm{H}} \boldsymbol{s}_{\mathrm{V}}^{\mathrm{H}} \boldsymbol{w}_{\mathrm{V}} + \boldsymbol{w}_{\mathrm{V}} \boldsymbol{w}_{\mathrm{V}}^{\mathrm{H}}\right\} \\ &= \boldsymbol{H}_{\mathrm{V}} \boldsymbol{R}_{ss} \boldsymbol{H}_{\mathrm{V}}^{\mathrm{H}} + \boldsymbol{R}_{ww} \ . \end{aligned} \tag{2.42}$$

In Figure 2.11, the error vector is given as

$$\begin{aligned} \boldsymbol{e}[k] &= \hat{\boldsymbol{s}}[k] - \boldsymbol{s}[k] \\ &= \boldsymbol{F}_{\mathrm{V}} \boldsymbol{r}_{\mathrm{V}} - \boldsymbol{s}_{\mathrm{V}} \ , \end{aligned} \tag{2.43}$$

From [Pro08], the aim of an MMSE equalizer can be mathematically represented as

$$\boldsymbol{F}_{\mathrm{V}} = \operatorname{argmin} \mathrm{E}\left\{ \| \, \boldsymbol{e}[k] \, \|^2 \right\} \quad . \tag{2.44}$$

The cross-correlation between the error and received signal $\boldsymbol{R}_{er}$ is given as

$$\begin{aligned} \boldsymbol{R}_{er} &= \mathrm{E}\left\{ \boldsymbol{e} \boldsymbol{r}_{\mathrm{V}}^{\mathrm{H}} \right\} \\ &= \mathrm{E}\left\{ \left(\boldsymbol{F}_{\mathrm{V}} \boldsymbol{r}_{\mathrm{V}} - \boldsymbol{s}_{\mathrm{V}} \right) \boldsymbol{r}_{\mathrm{V}}^{\mathrm{H}} \right\} \\ &= \mathrm{E}\left\{ \boldsymbol{F}_{\mathrm{V}} \boldsymbol{r}_{\mathrm{V}} \boldsymbol{r}_{\mathrm{V}}^{\mathrm{H}} - \boldsymbol{s}_{\mathrm{V}} \boldsymbol{r}_{\mathrm{V}}^{\mathrm{H}} \right\} \\ &= \boldsymbol{F}_{\mathrm{V}} \mathrm{E}\left\{ \boldsymbol{r}_{\mathrm{V}} \boldsymbol{r}_{\mathrm{V}}^{\mathrm{H}} \right\} - \mathrm{E}\left\{ \boldsymbol{s}_{\mathrm{V}} \boldsymbol{r}_{\mathrm{V}}^{\mathrm{H}} \right\} \\ &= \boldsymbol{F}_{\mathrm{V}} \boldsymbol{R}_{rr} - \boldsymbol{R}_{sr} \quad . \end{aligned} \tag{2.45}$$

The principle of MMSE equalizer states that there should be no correlation between the error and received signals $\boldsymbol{R}_{er} = 0$ [Kam18]. Hence, (2.45) can be solved as

$$\begin{aligned} \boldsymbol{R}_{er} &= \boldsymbol{F}_{\mathrm{V}} \boldsymbol{R}_{rr} - \boldsymbol{R}_{sr} = 0 \\ \boldsymbol{F}_{\mathrm{V}} &= \boldsymbol{R}_{sr} \boldsymbol{R}_{rr}^{-1} \quad . \end{aligned} \tag{2.46}$$

Substituting (2.41) and (2.42) into (2.46) leads to

$$\boldsymbol{F}_{\mathrm{V}} = \boldsymbol{R}_{ss} \boldsymbol{H}_{\mathrm{V}}^{\mathrm{H}} \left(\boldsymbol{H}_{\mathrm{V}} \boldsymbol{R}_{ss} \boldsymbol{H}_{\mathrm{V}}^{\mathrm{H}} + \boldsymbol{R}_{ww} \right)^{-1} \quad . \tag{2.47}$$

In case of uncorrelated transmit symbols and noise samples,

$$\begin{aligned} \boldsymbol{R}_{ss} &= P_{\mathrm{s}} \cdot \boldsymbol{I} \\ \boldsymbol{R}_{ww} &= P_{\mathrm{n}} \cdot \boldsymbol{I} \quad , \end{aligned} \tag{2.48}$$

with P_{s} and P_{n} denoting transmit and noise powers. On substituting (2.48) into (2.47) results in MMSE equalizer

$$\begin{aligned} \boldsymbol{F}_{\mathrm{V}} &= \left(P_{\mathrm{s}} \cdot \boldsymbol{I} \right) \boldsymbol{H}_{\mathrm{V}}^{\mathrm{H}} \left(\boldsymbol{H}_{\mathrm{V}} \left(P_{\mathrm{s}} \cdot \boldsymbol{I} \right) \boldsymbol{H}_{\mathrm{V}}^{\mathrm{H}} + \left(P_{\mathrm{n}} \cdot \boldsymbol{I} \right) \right)^{-1} \\ &= \boldsymbol{H}_{\mathrm{V}}^{\mathrm{H}} \left(\boldsymbol{H}_{\mathrm{V}} \boldsymbol{H}_{\mathrm{V}}^{\mathrm{H}} + \frac{P_{\mathrm{n}}}{P_{\mathrm{s}}} \cdot \boldsymbol{I} \right)^{-1} \quad , \end{aligned} \tag{2.49}$$

where $\boldsymbol{I}$ is the identity matrix. The MMSE solution approaches a ZF principle in case of substantial signal-to-noise-ratio (SNR). Moreover, a matched-filter solution is approached in the presence of low interference [Pro08; Kam18].

2.4. Quality Criteria

The system performance of an optical transmission link is evaluated using BER, which is considered as the key performance indicator. The theoretical BER performance $P_{\mathrm{BER}}^{(\mathrm{th})}$ of a SISO system utilizing the PAM-M format is given by

$$P_{\mathrm{BER}}^{(\mathrm{th})} = \frac{1}{\log_2(M)} \left(\frac{M-1}{M} \right) \operatorname{erfc} \left(\sqrt{\frac{\varrho}{2}} \right) \quad , \tag{2.50}$$

where $\operatorname{erfc}(\cdot)$ denotes complementary error function and ϱ is the SNR [Pro08]. The calculation of the BER is conducted by assuming that whenever an error is encountered, it will only be limited to the neighboring symbol. However, multiple errors can occur at a lower average received power. Secondly, BER calculations require an identical noise variance of each symbol. In contrary, different noise variances are observed in the shot noise dominant area. Hence, the accuracy of the system performance is compromised using (2.50). The area integration method is introduced to overcome these drawbacks for estimating the BER.

Area Integration Method

The BER is estimated using the probability density function (PDF) of the received symbols r_m, with $m = [0, 1, 2, \ldots, M-1]$. The characteristics of a PDF are approximated with a Gaussian distribution due to the prevailing noise mechanisms, such as shot and thermal noise. The generalized Gaussian PDF $f(x)$ with $x \in \mathbb{R}$ is expressed as

$$f(x) = \frac{1}{\sqrt{2\pi}\sigma} \cdot \exp \left(\frac{-(x-\bar{x})^2}{2\sigma^2} \right) \quad , \tag{2.51}$$

where σ is the standard deviation, $\bar{x}$ represents the mean of the variable x. The mean and variance of each symbol are calculated using (2.3) and (2.21), respectively. The Gray coded symbols are transmitted over the optical link during each transmission instance [Pro08]. At the receiver side, the received symbol undergoes optical-electrical conversion, transimpedance amplification and receive filtering. Consequently, a hard decision is conducted using a threshold decider based on the decision region R_m and the decision threshold τ_n with $n = [0, 1, \ldots, M-2]$. An exemplary constellation diagram at the transmitter with

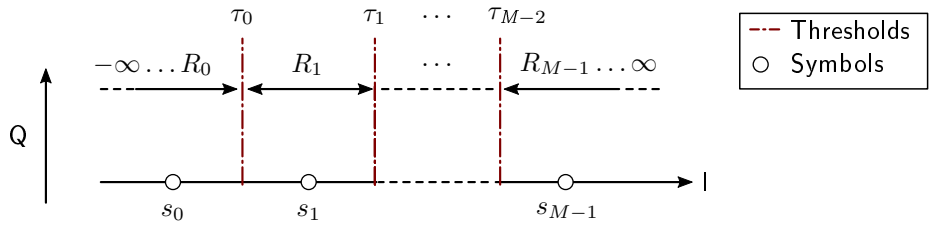

Figure 2.12.: Generalized transmitter constellation diagram for PAM-M.

the decision regions and thresholds is shown in Figure 2.12. The signal space is segregated into non-overlapping decision regions using the thresholds. The R_m region is defined as $R_0 \in (-\infty, \tau_0]$, $R_{M-1} \in [\tau_{M-2}, \infty)$ and $R_m \in [\tau_{m-1}, \tau_m]$. After the hard decision, the decider decides in favor of s_m when the received symbol r_m is situated in the region R_m. According to Figure 2.12, each symbol belongs to its defined region with its respective threshold. When the received symbol is detected outside their decision region, that symbol is labeled as a symbol error. The symbol-specific BER, when s_m is transmitted, is calculated as

$$P_{\mathrm{BER}}^{(s_m)} = \frac{1}{\log_2(M)} \sum_{i=0}^{M-1} h_{m,\,i} \cdot \int_{R_i} p(r_m)\,\mathrm{d}r \ , \tag{2.52}$$

where the PDF of the received symbol r_m is represented as $p(r_m)$. The Hamming distance $h_{m,\,i}$ is the distance between the symbols s_m and s_i. The number of differing bits between s_m and s_i is defined as Hamming distance, where $h_{m,\,i} = 0$ in the case of $m = i$. The overall system performance is calculated as

$$P_{\mathrm{BER}} = \frac{1}{M} \sum_{m=0}^{M-1} P_{\mathrm{BER}}^{(s_m)} \ . \tag{2.53}$$

Signal-to-Noise Ratio

The performance of the optical transmission link is evaluated using an SNR, which is expressed as ϱ. From (2.50), it is evident that the BER is directly dependent upon the transmission quality ϱ or SNR. Considering an optical link with a PIN photodiode, the SNR of such a system is expressed as

$$\varrho = \frac{(\text{Half vertical eye opening})^2}{\text{Noise power}} = \frac{(U_{\mathrm{A}})^2}{P_{\mathrm{n}}} \ , \tag{2.54}$$

where U_{A} is the half vertical eye opening and the noise power is denoted as P_{n}. The two fundamental noise mechanisms present in a PIN photodiode are shot noise and thermal noise [Agr02]. Therefore, the total noise power P_{n} is defined as

$$P_{\mathrm{n}} = \sigma_{\mathrm{total}}^2 = \sigma_{\mathrm{sh}}^2 + \sigma_{\mathrm{th}}^2 \ . \tag{2.55}$$

From Figure 2.9, it is evident that either shot noise or thermal noise dominate according to the average received optical power. Using (2.19), the transmission quality in the shot noise limited ϱ_{sh} is given as

$$\varrho_{\mathrm{sh}} = \frac{(U_{\mathrm{A}})^2}{\sigma_{\mathrm{sh}}^2} = \frac{(U_{\mathrm{A}})^2}{2q_0\big(i(t) + I_{\mathrm{d}}\big)B} \ . \tag{2.56}$$

Similarly, the transmission quality in the thermal noise dominant region ϱ_{th} is calculated using (2.20), and it is expressed as

$$\varrho_{\mathrm{th}} = \frac{(U_{\mathrm{A}})^2}{\sigma_{\mathrm{th}}^2} = \frac{(U_{\mathrm{A}})^2 R_{\mathrm{f}}}{4k_{\mathrm{B}}TBF_{\mathrm{n}}} \ . \tag{2.57}$$

2.5. Noise Compensation Strategies using Constellation Shaping

The performance of an IM/DD is limited due to the square-law detection and the fiber dispersion. Therefore, the primary goal is to achieve optimal performance, which can be accomplished by maximizing tolerance against noise mechanisms. The optical receiver incorporated for direct detection is corrupted mainly with shot noise and thermal noise [Agr02]. Constellation shaping techniques provide an aid to mitigate these noise impairments to further boost the system performance. Theoretically, a constellation shaping gain of up to 1.5 dB can be achieved with higher-order modulation formats [For84]. These techniques are broadly divided into two categories, namely GCS and probabilistic constellation shaping (PCS). An overview of these techniques is demonstrated in Figure 2.13, where the positioning of the constellation points is plotted with the occurrence probability.

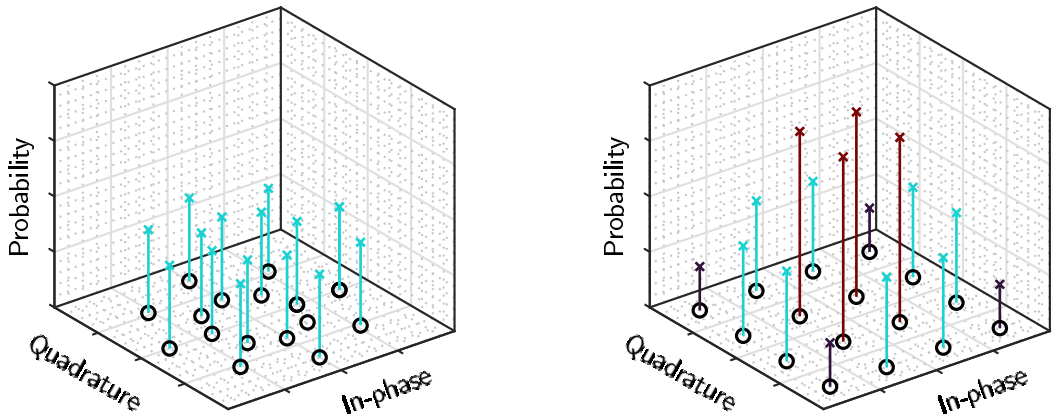

(a) GCS with a non-equidistant positioning of the constellation points and equal occurrence probability.

(b) PCS with a distinct probability distribution and equidistant constellation points.

Figure 2.13.: Types of constellation optimization using (a) GCS and (b) PCS with an exemplary QAM-16.

Probabilistic Constellation Shaping is an optimization concept in which the occurrence probability of an equidistant constellation is modified. During transmission, low-amplitude constellation points are transmitted with a higher probability in comparison to the high-

amplitude constellation points using the shaping encoder [QDA19]. The major advantages of deploying PCS are rate adaptability and energy efficiency gains. In PCS, a distribution matching technology at the transceiver is essential. In long-haul applications, the utility of PCS with M-ary QAM has been proven to be beneficial in BER enhancement [QDA19; Cho18; Cai18]. However, the system complexity is increased due to the shaping encoder and decoder [Log16].

Geometric Constellation Shaping is the non-uniform distribution of the Euclidean distance between constellation points. The occurrence probability of all the constellation points is maintained to be equal, i.e., constellation points are independently and identically distributed. According to the literature, GCS has proven to be beneficial with non-linear optical fiber channel [MAK21]. In [Log16] and [Che18], the GCS technique with M-ary QAM has yielded an SNR gain of more than 1.5 dB and 1.18 dB, respectively. Another approach, presented in [Jov23] and [Yan22], is to use an unsupervised end-to-end machine learning algorithm incorporating neural networks for optimizing the positioning of constellation points. Majorly, the performance improvements using GCS are reported in long-haul coherent systems with higher-order modulation formats ($M > 2$) [Ess10].

Hybrid Probabilistic-Geometric Constellation Shaping is a technique in which the constellation points are not limited to an equal occurrence probability or equidistant distribution. The constellation points are situated in accordance with the optimized mutual information. Additionally, the occurrence probability of each constellation point is governed by the Huffman tree [QDA19]. Hybrid probabilistic-geometric constellation shaping (HPGCS) has been proven to be beneficial in enhancing the system performance in [QDA19; QD18; Bat17; Zha18b; SAH19]. Although HPGCS is advantageous, it is challenging to implement HPGCS with an increasing number of constellation points [QDA19].

Since cost-effectiveness and complexity are the main requirements in an IM/DD system, GCS can be a low-complexity alternative to PCS and HPGCS [Jov23; Yan22]. While using higher-order modulation formats, it is necessary to provide higher transmit power for achieving optimal performance. Subsequently, a restriction over transmit power should be incorporated to avoid fiber nonlinearities [SFP13; WHL21]. Against this background, the GCS tailored for an IM/DD system using PAM-M formats should be investigated to improve system performance. Therefore, this section focuses on GCS in IM/DD systems with higher-order PAM-M formats.

Geometric Shaping Optimization in IM/DD systems

In order to quantify the effectiveness of the GCS under a given noise mechanism, an IM/DD-based SISO optical system is considered, which is shown in Figure 2.14. The encoded

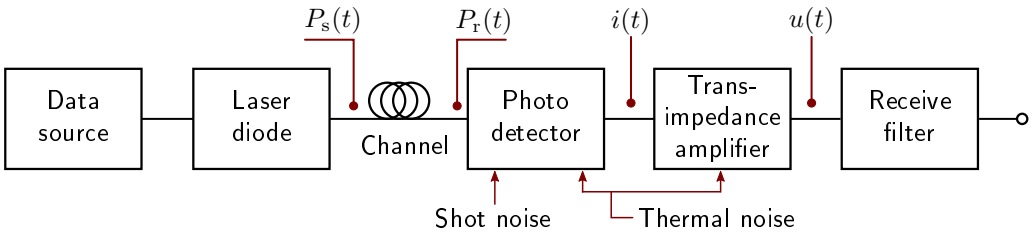

Figure 2.14.: Block diagram of an IM/DD system with two fundamental noise mechanisms.

binary input bit stream is mapped on M-ary symbols or constellation points, where each symbol represents $\log_2(M)$ bits. The mapping of the symbols $\boldsymbol{s} = [s_0, s_1, \ldots, s_{M-1}]$ is conducted onto the PAM-M scheme and then modulated using a DML source. Subsequently, the modulated signal propagates through the channel with a transmit power $P_s(t)$. The transmitted signal undergoes attenuation A due to the provided optical fiber channel. It is worth noting that the channel is assumed to be non-dispersive in order to scale down the system complexity. Finally, the photodiode receives an optical signal with a power $P_r(t)$ and converts the signal into photocurrent $i(t)$. Since the optical to electrical conversion process is not ideal, it corrupts the received signal with shot and thermal noise. In addition to this, the transimpedance amplifier contributes to the amplification of thermal noise along with converting current into voltage $u(t)$. In the final stage, the receive filtering is conducted and the SNR is evaluated for system performance.

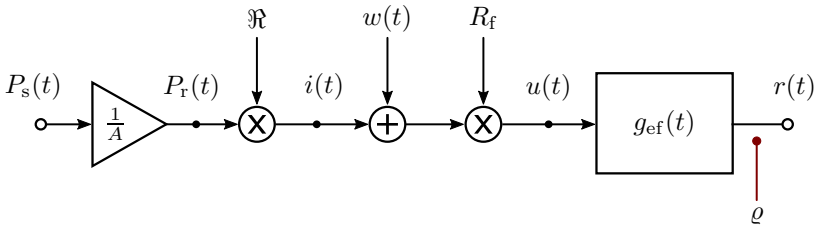

Figure 2.15.: System model for signal analysis.

Using (2.3), the signal amplitudes of the transmitted vector $\boldsymbol{s}$, which are attenuated by A, are adapted with the provided system model, and are defined as

$$s_m = \frac{m}{M-1} \cdot P_{s,\max} = \frac{m}{M-1} \cdot P_{r,\max} \cdot A \ , \tag{2.58}$$

with $P_{s,\max}$ and $P_{r,\max}$ denoting the maximum transmission of the laser diode and received power of the receiver, respectively. A detailed signal analysis of the measurement setup is illustrated in Figure 2.15. In the system model, the shot and thermal noise are represented by $w(t)$, which is added to the received signal. Simultaneously, using the feedback resistor R_f, the photocurrent is converted into the voltage $u(t)$. Finally, the received signal $r(t)$ is filtered using receive filtering $g_{ef}(t)$. The overall BER performance is computed using SNR ϱ after the receive filtering.

The overall transmission quality for a short reach optical link using the PAM-M constellation, as mentioned in (2.3), is defined as

$$\varrho \approx \frac{\left(I_\mathrm{p}\,\chi\,R_\mathrm{f}\right)^2}{P_\mathrm{n}\,R_\mathrm{f}^2} = \frac{U_\mathrm{A}^2}{P_\mathrm{n}\,R_\mathrm{f}^2} = \frac{\left(I_\mathrm{p}\cdot\dfrac{1}{2(M-1)}\right)^2}{2q_0 i(t)B + \dfrac{4kTF_\mathrm{n}B}{R_\mathrm{f}}}\ , \tag{2.59}$$

where variable χ is a scaling factor which is used to ensure the half vertical eye opening is equal to $I_\mathrm{p}\,\chi\,R_\mathrm{f}$. When the definition of SNR includes shot noise, it should be considered as time dependent.

Optimization Statement

GCS modifies the Euclidean distance between the constellation points to mitigate the noise impairments. The hypothesis states that improvements in BER performance are yielded when the distance between the symbols is adapted according to the individual noise variances. In order to verify this hypothesis, a constrained optimization statement is formulated utilizing GCS with PAM-M. The mathematical representation of the optimization is given as

$$\begin{aligned} &\underset{s_m}{\text{minimize}} && P_\mathrm{BER}(s_m) \\ &\text{subject to} && s_{j-1} < s_j < s_{j+1} \quad \forall j = 1, 2, \ldots, M-2 \\ &\text{and} && s_0 = 0, \quad s_{M-1} = P_{\mathrm{r,max}} \cdot A\ . \end{aligned} \tag{2.60}$$

The objective function in (2.60) aims to minimize the overall BER P_BER. The inequality constraint specifies the orderly arrangement of the symbols. Additionally, the maximum transmit power is provided to the last symbol, and the first symbol is situated at the non-negative signal space. An interior-point algorithm is utilized for the above-mentioned optimization problem [Wal05; Wol11].

2.5.1. Simulated Performance Evaluation

The advantages of GCS are determined using the provided system model with the optimization statement. The results are calculated with the help of Monte-Carlo simulations. Consequently, the obtained results are categorized into three different scenarios. The PDFs of all symbols and the symbol-specific BER are depicted in each scenario.

Scenario 1 represents the thermal noise dominant region with $M \leq 16$. A PAM-4 constellation with $P_\mathrm{r} = -28\,\mathrm{dBm}$ is selected and illustrated in Figure 2.16. The simulated PDF of the received data and the symbol-specific BER are represented. From Figure 2.16, it is evident that all the symbols are affected by a similar noise variance. Moreover, the thresholds are already at the optimal position, i.e., where the minimal error probability areas are situ-

ated, with an equidistant constellation diagram. Hence, the utility of GCS is not required. It is worth noting that the exhibition of lower BER by the first symbol, s_0, and the last symbol s_3, is due to the presence of only one threshold.

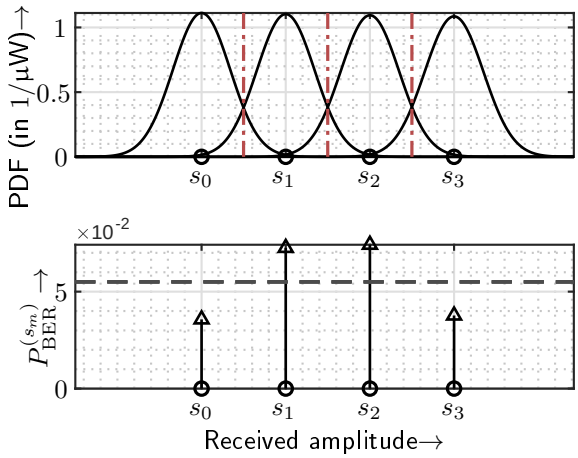

Figure 2.16.: Simulated receive data's PDFs (top) and the symbol-specific BERs (bottom), where s_m denotes the corresponding transmit symbols, for the first scenario (PAM-4, $P_{\mathrm{r}} = -28\,\mathrm{dBm}$, dashed and dash-dotted lines represent the overall BER and thresholds, respectively).

Scenario 2 describes the shot noise dominant region with $M \leq 16$. A higher received power of $P_{\mathrm{r}} = -10\,\mathrm{dBm}$ is applied using a PAM-4 constellation. The resulting PDF of each symbol and their respective symbol-specific BER are illustrated in Figure 2.17. The narrow standard deviation of PDFs resulting in no overlapping of the error probability areas. Thus,

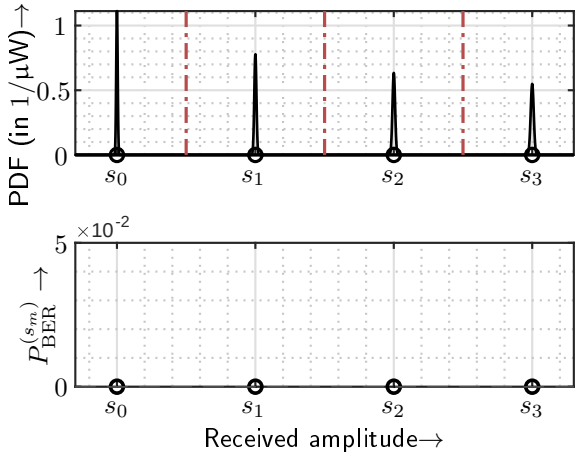

Figure 2.17.: Simulated receive data's PDFs (top) and the symbol-specific BERs (bottom), where s_m denotes the corresponding transmit symbols, for the second scenario (PAM-4, $P_{\mathrm{r}} = -10\,\mathrm{dBm}$, dash-dotted lines depict the thresholds).

repositioning the constellation points using GCS will be inadequate as the overall BER is estimated to be zero.

Scenario 3 is the shot noise dominant region with $M > 16$. In contrary to the second scenario, a larger constellation size is considered to enable an overlap between the Gaussian PDFs. In Figure 2.18, PAM-64 with $P_\mathrm{r} = -10\,\mathrm{dBm}$ is shown, where the first three and the last three symbols are depicted due to simpler visualization. It is evident that each symbol has a distinct estimated PDF. Moreover, the overlap between adjacent PDFs is significant due to an increase in the constellation size. The symbols with low power exhibit a lower symbol-specific BER in comparison to the high power symbols. Therefore, GCS is expected to improve the BER performance under this scenario with non-uniform spacing between the constellation points.

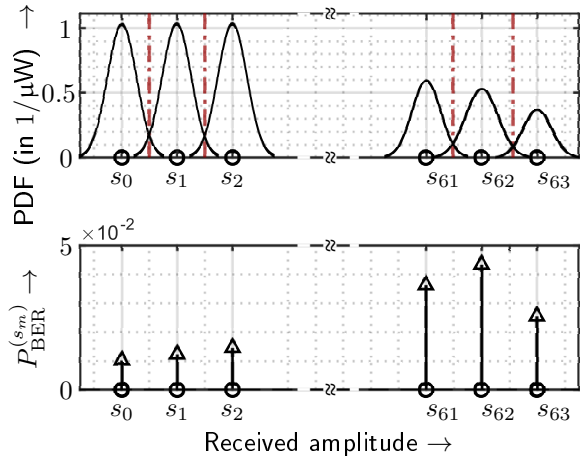

Figure 2.18.: Simulated receive data's PDFs (top) and the symbol-specific BERs (bottom), where s_m denotes the corresponding transmit symbols, for the third scenario (PAM-64, $P_\mathrm{r} = -10$ dBm, dash-dotted lines depict the thresholds).

The GCS optimization is implemented on the provided system model. Consequently, the symbol-specific BER of PAM-64 is calculated according to the received amplitudes. GCS optimization results are demonstrated in Figure 2.19, where only every seventh symbol is displayed for illustration purposes. The position of the constellation points using the GCS exhibits that the symbols with a lower power are arranged close together compared to an equidistant constellation. Additionally, it is observed that the high power symbols are situated further apart from each other. Thus, it leads to an identical symbol-specific BER except for the first and last symbols. The overall BER is ultimately improved by nearly 3-fold in comparison to the equidistant constellation. In Figure 2.19, the overall BERs are illustrated with the dashed lines.

On the basis of performance improvements in the third scenario, the system BERs in

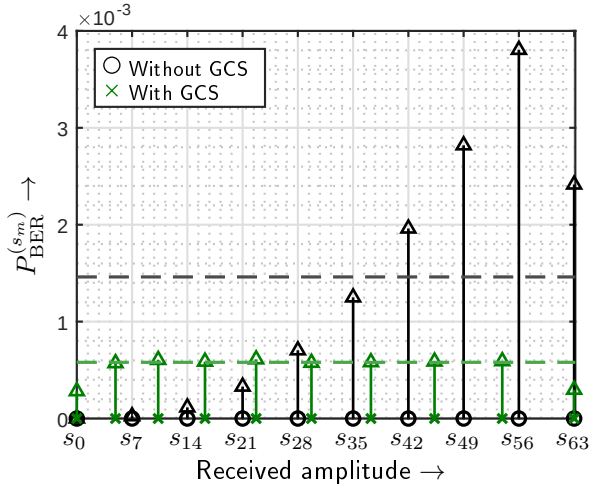

Figure 2.19.: Resulting received constellation with the symbol-specific BERs, where s_m denote the corresponding transmit symbols, comparing GCS and without GCS (PAM-64, $P_{\mathrm{r}} = -10$ dBm, dashed lines represent the overall BERs).

dependency on the average received power are computed, which are shown in Figure 2.20. The BERs are calculated for PAM-M with $M = [4, 8, 16, 32, 64, 128]$ over an entire range of the received power, i.e., irrespective of the noise dominant region. From Figure 2.20, it is clear that GCS yields no significant benefits when $M \leq 16$. This is confirmed by the BERs of PAM-4, PAM-8 and PAM-16. The presence of identical Gaussian PDFs in the thermal noise dominant region and distant PDFs in the shot noise dominant region is the primary cause of the inadequacy of GCS. Thus, an equidistant constellation is optimal to utilize under $M \leq 16$.

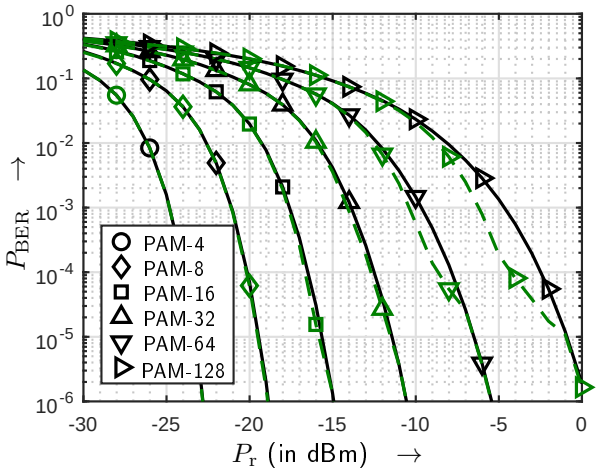

Figure 2.20.: BER in dependence on the average optical received power with GCS (green dashed line) and without GCS (black solid line).

On further analysis, the BER improvements due to GCS are depicted with larger constellation sizes $M > 16$. Considering the BER of PAM-64, an improvement of $\approx 0.4\,\mathrm{dB}$ is observed at a BER of 10^{-3} with the utilization of GCS. The performance enhancements are limited in the range of $P_\mathrm{r} = [-12, -7]\,\mathrm{dBm}$. It implies that conditions of the third scenario are prevalent with the current constellation size and received power. When $P_\mathrm{r} \leq -12\,\mathrm{dBm}$, the symbols are affected with identical PDFs according to the first scenario. Similarly, the location of the constellation points are far away from each other due to high received power with $P_\mathrm{r} > -7\,\mathrm{dBm}$ under the second scenario. Therefore, the use of equidistant constellation points is recommended when PAM-64 with $P_\mathrm{r} \notin [-12, -7]\,\mathrm{dBm}$ is applied. The GCS gain at a BER of 10^{-3} with the different constellation sizes is mentioned in Table 2.2. It is worth noting that higher GCS gains can be achieved at distinct BER levels.

Table 2.2.: Reduction in the required average optical received power to achieve a BER of 10^{-3} when comparing GCS with equidistant constellation for different modulation sizes.

Modulation format	GCS gain (in dB)
PAM-4	0.003
PAM-8	0.031
PAM-16	0.079
PAM-32	0.225
PAM-64	0.389
PAM-128	1.541

In summary, the GCS is proven to be beneficial with high constellation sizes. The optimization statement is formulated with regards to the maximum transmit power and orderly arrangement of the constellation points. An improved symbol-specific BER is achieved by placing low power symbols together and high power symbols far away. This non-uniform spacing between the constellation points leads to an enhancement in the overall system performance. Thus, the advantages of GCS are validated with the simulation results.

2.5.2. Experimental Measurement Results

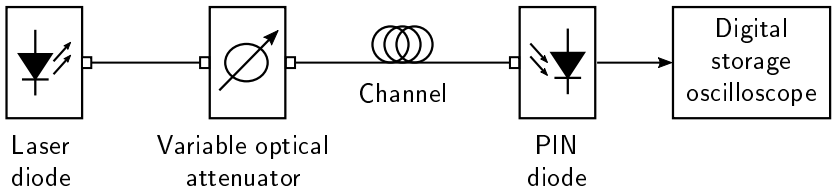

Figure 2.21.: Experimental setup to observe the noise variances.

The concept of GCS is solely dependent upon the distinct noise variances of the higher-order constellations. Thus, an experimental setup is proposed to analyze the dependency of

Table 2.3.: Measured noise variance in dependency on the average optical received power.

Attenuation (in dB)	P_r (in dBm)	Noise variance (in mV^2)
3	-11.30	0.2057
4	-12.31	0.1304
5	-13.31	0.1052
6	-14.26	0.0959
7	-15.24	0.0921
8	-16.27	0.0915
9	-17.28	0.0902
10	-18.26	0.0903
11	-19.26	0.0902

noise variance over the received power. The developed experimental setup is demonstrated in Figure 2.21. At the transmitter side, a laser diode with an operating wavelength of $\lambda = 1310\,\text{nm}$ is utilized. Additionally, a variable optical attenuator is added to provide a particular attenuation to the transmitted signal. An SMF of 1 m length is incorporated as the channel. The incident optical signal is converted into an electrical signal using a PIN photodiode, after propagating through the channel. Finally, the received signal is captured by a digital storage oscilloscope with a bandwidth of 13.6 GHz.
The measured noise variance and the average optical received power are depicted in Table 2.3. From the incremental noise variance in the table, it is evident that the shot noise is dominant when $P_r > -15\,\text{dBm}$. Similarly, the prevalent thermal noise is indicated with a constant noise variance of $\approx 0.09\,\text{mV}^2$ having $P_r < -16\,\text{dBm}$.

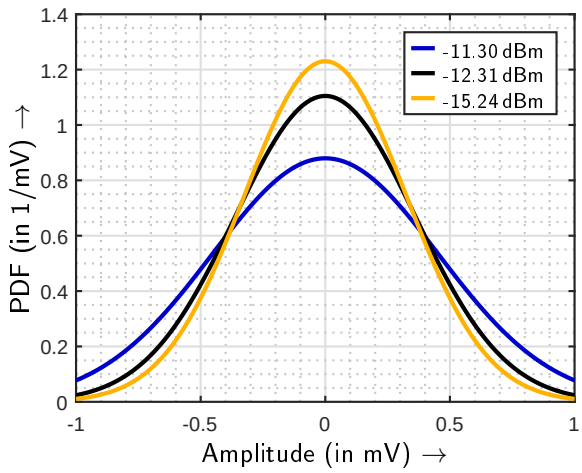

Figure 2.22.: Empirical noise PDFs comparing different received power levels.

Consequently, the PDF with the measured noise variances is shown in Figure 2.22. From Table 2.3, three noise variances are taken into account with zero mean for comparison pur-

poses only. Apparently, the distinct Gaussian PDFs are obtained for the shot noise dominant region due to their different experimental noise variances. Hence, BER improvements can be achieved by utilizing the GCS in the shot noise dominant region with higher constellation size, matching to the theory.

3. Joint-Transceiver Equalizer Design in a SISO System

This chapter focuses on analyzing the contribution of a joint-transceiver equalizer design in the enhancing the BER performance. A short reach and low-cost optical transmission system with an IM/DD utilizing an MMF is considered for this investigation. The signal transmission through an MMF is impaired with chromatic and modal dispersion. Consequently, these optical multi-mode systems are limited in data rate and length due to the significant presence of dispersion mechanisms. Physical compensation techniques to mitigate chromatic dispersion prevail for SMF systems such as dispersion compensation fibers and fiber-Bragg gratings (FBGs) [DKX09]. On the contrary, these techniques are inadequate to mitigate modal dispersion in MMF transmission links. Hence, applying advanced digital signal processing (DSP) techniques, i.e. equalization, are often necessary as they offer a potential low-cost solution and architectural compatibility to an IM/DD system. Practically, equalization schemes at the receiver side such as a decision feedback equalizer [Doc20; Li17; SBK17] and a Volterra equalizer [Huo18; Kim17] are chosen, since the channel state information is not required at the transmission end.

According to recent studies, the combination of pre-equalization with post-equalization has proven to outperform the equalization available either solely at the transmitter or at the receiver [ZYC17; Tan20; Zou20a; CZB21]. Conventionally, the computation of pre-equalizer and post-equalizer is conducted independently [Raj19; YT10]. Several studies have reported that the utilization of different pre-equalizer filter design principles, which include ZF [Zou20a; Tan20], Tomlinson-Harashima precoding [HM72] and the feedback filter [CZB21]. However, the ZF pre-equalizer design is generally incorporated due to its simpler implementation.

This chapter starts with a multi-mode system model incorporated with the joint-PPE or joint-transceiver technique. The mathematical analysis of the system model and joint-PPE filter computation are demonstrated in this section. Thereafter, the effectiveness of the proposed PPE filter is evaluated using a Monte Carlo simulation. Additionally, the obtained BER results are verified using an experimental setup. In the end, the findings of the proposed joint-PPE are discussed.

3.1. SISO System Model

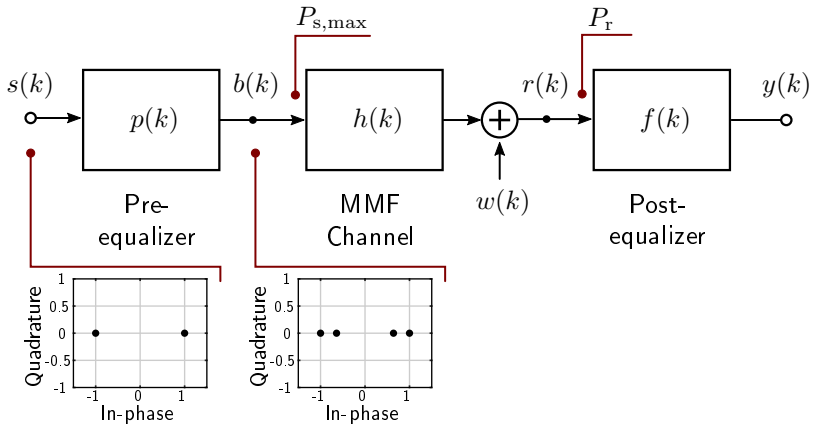

Figure 3.1.: System model and corresponding constellation diagrams at the transmitter side.

The SISO-based system model, in conjunction with a PPE filter, is illustrated in Figure 3.1. Additionally, the constellation diagrams of the input signal $s(k)$ and the pre-equalized signal $b(k)$ are also demonstrated. A binary data stream is converted into symbols, which are mapped to a PAM-2 format. Hereafter, an impulse generator converts the symbols into $s(k)$ with $s[k] \in \{s_0, s_1\}$. Therefore, the constellation diagram of $s(k)$ shows two constellation points in Figure 3.1. The input signal $s(k)$ undergoes pre-equalization denoted by $p(k)$, which results in the pre-equalized signal $b(k)$. A number of distinct signal amplitudes N are generated in $b[k] \in \{b_0, b_1, \ldots, b_{N-1}\}$ in accordance with the length of the pre-equalizer L_{p}. The relation between N and L_{p} is formulated as $L_{\mathrm{p}} = \log_2(N)$. The multi-level signaling is formed using a two-tap pre-equalizer, which is depicted in the constellation diagram after the pre-equalization in Figure 3.1. The multi-level signaling provides an aid to pre-compensate channel degradation. A restraint on the transit power is applied, which is given as

$$s_1 = b_{N-1} = q \cdot P_{\mathrm{s,max}} \ . \tag{3.1}$$

In (3.1), the input and pre-equalized symbols with the highest amplitude are provided with the maximum transmission power of the laser source. In addition, the conversion from electrical to optical domain is denoted by the factor q.

An analytical representation of an elementary SISO system without a pre-equalizer is given as

$$r(k) = h(k) * s(k) + w(k) \ , \tag{3.2}$$

with $*$ denoting the convolution operator. The received signal $r(k)$ comprises of the frequency-selective channel $h(k)$ affecting the transmitted signal $s(k)$ and the additive, white and Gaussian noise (AWGN) signal $w(k)$. Thereafter, pre-equalization $p(k)$ is applied to $s(k)$, and

$r(k)$ is expressed as

$$r(k) = h(k) * p(k) * s(k) + w(k) \ . \tag{3.3}$$

Since the complexity at the transmitter should not increase to a larger extent in an IM/DD system, a few-tap pre-equalizer is utilized. Thus, the channel degradation is partially equalized. Consequently, the post-equalization is implemented to recover the transmitted signal, and the resulting signal after post-equalization $y(k)$ is defined as

$$\begin{aligned} y(k) &= f(k) * r(k) \\ y(k) &= \underbrace{f(k) * h(k) * p(k)}_{\text{Term 1}} * s(k) + \underbrace{f(k) * w(k)}_{\text{Term 2}} \ . \end{aligned} \tag{3.4}$$

The resulting system model from Figure 3.1 is depicted in (3.4). In (3.4), the post-equalization filter $f(k)$ is implemented on the received signal, which results in two terms. The first term implies that the channel impairments can be mitigated jointly by using the PPE filter. On the other hand, the second term reveals that the post-equalization filter is solely responsible for noise amplification. Hence, by shifting a certain amount of the post-equalization efforts to the pre-equalizer can significantly minimize the noise enhancement. Therefore, the jointly designed PPE filter can aid in mitigating the channel influence while minimizing the noise increment to improve system performance.

3.2. Joint-Transceiver Design Concept

The principle of the joint-transceiver scheme is to design the pre- and post-equalizer for maximizing the SNR and minimal increase in the transmitter's complexity. The improved SNR is achieved by eliminating the ISI originating from the channel resulting in an enhanced system performance. The concept of a joint-transceiver or a joint-PPE scheme is to shift the post-equalizer coefficients to the transmitter and then collectively design and optimize the pre- and post-equalizer. Clearly, the BER performance is dependent upon the SNR, which is mentioned in (2.50) and (2.54). Noise amplification causes degradation of the BER performance due to the post-equalizer, which is evident from (3.4). Considering an MMF-based SISO system, where the ISI is assumed to be completely mitigated using a post-equalizer, the SNR ϱ will be defined as

$$\varrho = \frac{(\text{Half vertical eye opening})^2}{\text{Noise power}} = \frac{U_{\mathrm{A}}^2}{\widetilde{P}_{\mathrm{n}}} = \frac{U_{\mathrm{A}}^2}{P_{\mathrm{n}} \cdot \theta} \ , \tag{3.5}$$

with U_{A} and $\widetilde{P}_{\mathrm{n}}$ denoting the half-vertical eye opening and noise power after the post-equalizer, respectively. The noise amplification in accordance to the noise power P_{n} before the post-equalizer is quantified by the noise weighting factor (NWF) θ, where θ is expressed

as

$$\theta = \sum_{k=0}^{L_\mathrm{f}-1} \left| f\left[k\right] \right|^2 \ , \tag{3.6}$$

where the length of the post-equalizer is L_f and $f[k]$ with the square brackets refers to the k-th element from $f(k)$. From (3.5) and (3.6), a direct relation between the amplitude of post-equalization coefficients and SNR is established. Correspondingly, the system BER performance P_BER with PAM-2 format is formulated as

$$P_\mathrm{BER} = \frac{1}{2}\,\mathrm{erfc}\left(\sqrt{\frac{\varrho}{2}}\right) = \frac{1}{2}\,\mathrm{erfc}\left(\sqrt{\frac{U_\mathrm{A}^2}{2 \cdot P_\mathrm{n} \cdot \theta}}\right) \ , \tag{3.7}$$

with $\mathrm{erfc}(\cdot)$ representing the complementary error function. In (3.7), the dependency of BER over the NWF is stated. It is evident that performance benefits can be yielded by reducing the noise amplification originating from the post-equalization.

The effectiveness of the proposed joint- PPE scheme aims to shift the post-equalization efforts partially to the transmitter. Subsequently, resulting in the amplitude reduction of the post-equalizer coefficients, which will lead to BER improvements. In the joint-PPE scheme, a linear finite impulse response (FIR) pre-equalizer filter with length L_p is realized as

$$b[k] = \sum_{i=1}^{L_\mathrm{p}} p_i \cdot s[k-(i-1)] \ , \tag{3.8}$$

where p_i is the i-th coefficient of the pre-equalizer. By joint design and optimization of the pre- and post-equalizer, the channel degradation and noise amplification can be completely compensated. Thus, a mathematically constrained optimization statement is formulated to determine the coefficients of the joint-PPE scheme, which is defined as

$$\begin{aligned} &\underset{p(k),\, f(k)}{\text{minimize}} && \theta(h(k)) \\ &\text{subject to} && f(k) * p(k) * h(k) \approx z(k) \ , \\ &\text{and} && s_1 = q \cdot P_\mathrm{s,max}, \quad b_{N-1} = q \cdot P_\mathrm{s,max} \ . \end{aligned} \tag{3.9}$$

An interior-point algorithm is used in (3.9) with an objective to minimize the NWF θ, which is a function of the channel $h(k)$. Simultaneously, the PPE coefficients $p(k)$ and $f(k)$ are computed at the global minima of the NWF. The objective function complies with two constraints. The first constraint is responsible for mitigating the channel degradation by joint efforts from the PPE, resulting in a Nyquist vector $z(k)$. The limitation on the maximum transmit power is approved by the second constraint, where the highest amplitude symbol is provided with the maximum transmit power. It is worth noting that the channel state information is a prerequisite for determining the joint-PPE coefficients.

3.3. Performance Evaluation

In this section, the performance of the proposed joint-PPE scheme is evaluated over an MMF channel. The measured channel impulse response of a 250 m long MMF channel at an operating wavelength of 1550 nm is illustrated in Figure 3.2. It is evident that a significant amount of ISI is present in a 250 m long MMF channel. A pilot-based least square estimation algorithm is utilized to compute the channel influence over the known embedded pilot sequences. Firstly, a discrete-time Monte Carlo simulation incorporating the provided system model is constructed. Subsequently, these simulation results are verified using an experimental setup.

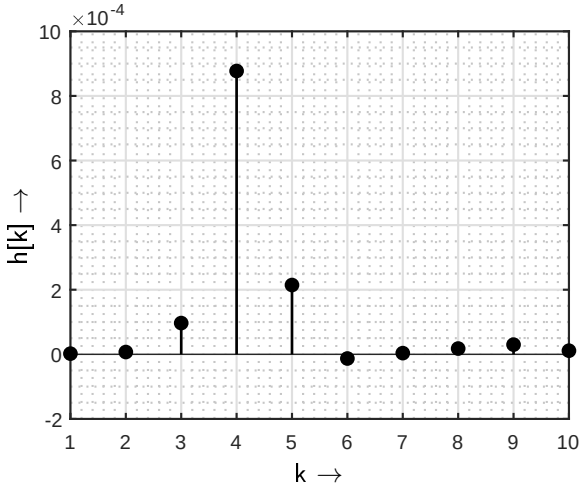

Figure 3.2.: Measured channel impulse response of a 250 m long MMF with respect to the symbol rate $f_{\mathrm{T}} = 1/T_{\mathrm{s}} = 2.5\,\mathrm{GHz}$ at 1550 nm operating wavelength.

The system performance is evaluated using the BER and an improvement factor Λ_x as the key performance indicators. The performances of the post-equalization only (PE-only) and the proposed joint-PPE schemes are compared with each other. The power improvement factor Λ_x describes the absolute reduction percentage in the required optical receive power P_{r} at a BER of 10^{-3} while using the joint-PPE scheme. Additionally, the power improvement factor is calculated as

$$\Lambda_x = \left| \frac{P_{\mathrm{r}}^{(\mathrm{PE})} - P_{\mathrm{r}}^{(\mathrm{PPE})}}{P_{\mathrm{r}}^{(\mathrm{PE})}} \right| , \tag{3.10}$$

where x provides the reference to utilized PE-ZF or PE-MMSE. This parameter characterizes the relative reduction in the NWF by utilizing the joint-PPE scheme with respect to PE-only. It implies that the Λ_x value will correspond to the effectiveness of the joint-PPE scheme.

Prior to the performance evaluation, it is essential to analyze the impact of post-equalizer coefficients on the system performance. Thus, the relation between the number of the post-equalizer coefficients with the BER and the NWF are illustrated in Figure 3.3. When a

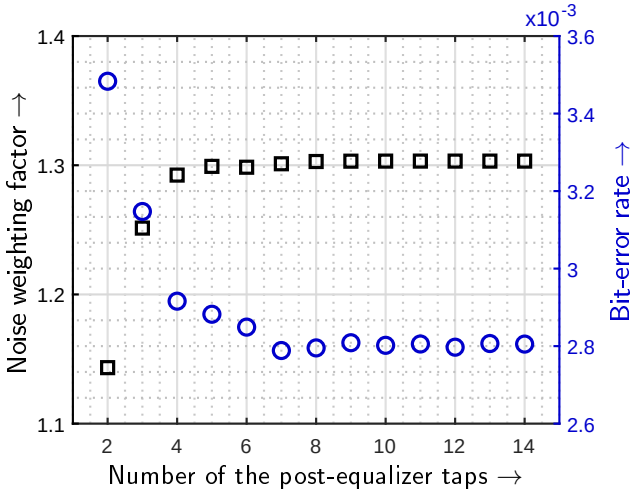

Figure 3.3.: Post-equalizer taps depending upon the NWF and BER at $P_\mathrm{r} = -15.3\,\mathrm{dBm}$.

fewer amount of post-equalizer coefficients ($L_\mathrm{f} < 8$) is utilized, a lower NWF with a degraded BER performance is yielded due to incomplete mitigation of the interference. However, the constant values of the NWF and the BER are observed once the post-equalizer coefficients are increased to eight or more ($L_\mathrm{f} \geq 8$). Therefore, the minimum number of post-equalizer coefficients correspond to eight for complete mitigation of the interference. Furthermore, the total number of equalization taps is set to be equal irrespective of the applied equalization scheme.

3.3.1. Simulation Results

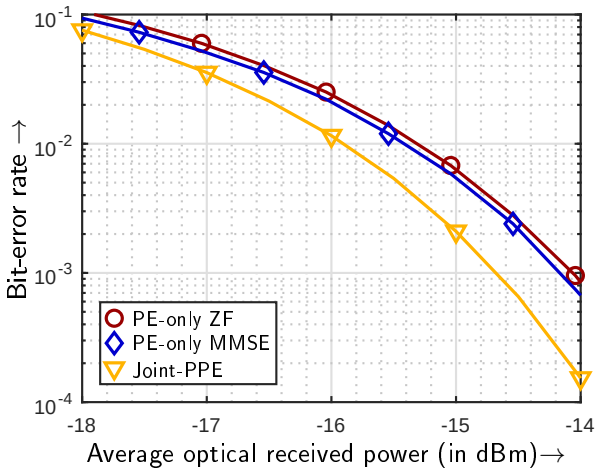

Figure 3.4.: Simulated BER in dependence on the average optical received power P_r comparing the PE-only scheme with the joint-PPE scheme having $L_\mathrm{p} = 2$.

A discrete-time Monte Carlo simulation is designed using the provided SISO system model. Three sequential steps are followed to obtain the simulation results. In the first step, the post-equalization only with ZF and MMSE principles is applied. Simultaneously, the channel impulse response is also computed using the appended pilot symbols in the transmitted data. Using the measured MMF channel, the joint-PPE coefficients are calculated using the above-stated optimization statement in the second step. Finally, the third step is concluded by assessing the performance of joint-PPE. Subsequently, the performances of each equalization scheme are compared based on the key performance indicators. Please note that the analog to digital conversion and vice versa is considered to be ideal during simulation.

In Figure 3.4, the simulated BER performance of the joint-PPE scheme is compared with the PE-ZF and PE-MMSE schemes. Clearly, the joint-PPE scheme with merely a two-tap pre-equalizer outperforms both of the PE-only schemes. The average received optical power P_r at a BER of 10^{-3} and the improvement factors are mentioned in Table 3.1. When the joint-PPE scheme with the pre-equalizer using four taps is compared with PE-ZF and PE-MMSE, a maximum reduction of $\approx 1\,\mathrm{dB}$ in P_r is observed. Similarly, the NWF using the joint-PPE with $L_\mathrm{p} = 4$ is reduced by 7.3 % and 6.8 % for the PE-ZF and PE-MMSE, respectively. When the conventional ZF-based pre-equalizer with PPE filter and joint-PPE are compared, a lower P_r is required to reach a BER of 10^{-3} and a power enhancement factor of $\approx 3\,\%$ is observed. It results in improving the SNR while using the joint-PPE schemes. Additionally, the joint-PPE scheme achieved a significant performance improvement with $L_\mathrm{p} = 2$ relative to minor improvements with $L_\mathrm{p} = 3$ or $L_\mathrm{p} = 4$. Therefore, the joint-PPE with a two-tap pre-equalizer is sufficient to attain similar BER performance for the experimental setup.

Table 3.1.: Simulated optical received powers and improvement factors at 10^{-3} BER with variable pre-equalizer filter lengths.

Equalization	L_p	L_f	P_r at 10^{-3} BER (in dBm)	NWF θ	Λ_ZF at 10^{-3} BER (in %)	Λ_MMSE at 10^{-3} BER (in %)
PE-ZF	-	25	-14.19	1.31	-	-
PE-MMSE	-	25	-14.26	1.29	-	-
ZF-PPE	2	23	-14.43	1.27	1.7	1.2
Joint-PPE	2	23	-14.85	1.22	4.7	4.1
Joint-PPE	3	22	-15.05	1.21	6.1	5.5
Joint-PPE	4	21	-15.23	1.20	7.3	6.8

3.3.2. Experimental Verification

The advantages of the proposed joint-PPE schemes are analyzed using an experimental setup, which is illustrated in Figure 3.5. Firstly, two pseudo-random binary sequences (PRBSs) of

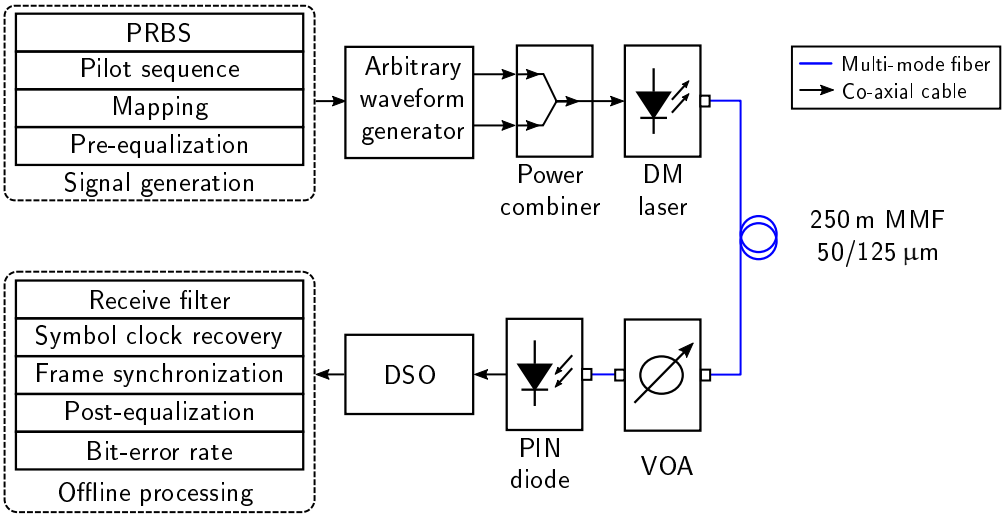

Figure 3.5.: Experimental setup for the joint-PPE scheme by using DML-based IM/DD system.

length $2^{12} - 1$ from the arbitrary waveform generator are mapped on a PAM-2 format. The pilot symbols are appended to the PRBSs. Assuming the channel state information is available at the transmitter, both sequences undergo pre-equalization using the joint-PPE scheme. Afterwards, a multi-level pre-equalized signal is formed using the power combiner, which has a 3 dB insertion loss. The electrical multi-level signal modulates a DML at the transmitter end, which operates at a 1550 nm wavelength. The maximum transmit power of the DML is $P_{\mathrm{s,max}} = 1.5\,\mathrm{dBm}$. Using (3.1), the maximum transmission power is applied to the symbol with a higher amplitude.

The transmitted optical signal propagates through a 250 m long MMF channel. A centric light launching condition is used to launch the optical signal into the MMF. This signal is adversely affected by the significant degradation due to modal dispersion and fiber attenuation. Prior to receiving the transmitted signal, a variable optical attenuator (VOA) is incorporated to sweep through all the possible range of average optical received power.

The transmitted signal is detected using a PIN diode, which functions as an optical to electrical converter and includes a trans-impedance amplifier. Please note that the utilized PIN diode consists of a large detection region, which is compatible with an MMF and leads to an inherent capacitance increase. In the end, the electrical signal is captured using a digital storage oscilloscope (DSO) with 40 GSa/s and 13.6 GHz bandwidth. The stored signal undergoes offline signal processing, which includes receive filtering, symbol clock recovery, frame synchronization and post-equalization. Finally, the BER is calculated with one sample per symbol and no forward error correction.

The experimental BER performance depending upon the average received optical power P_{r} is shown in Figure 3.6. The BER performance of PE-ZF and PE-MMSE schemes are tested

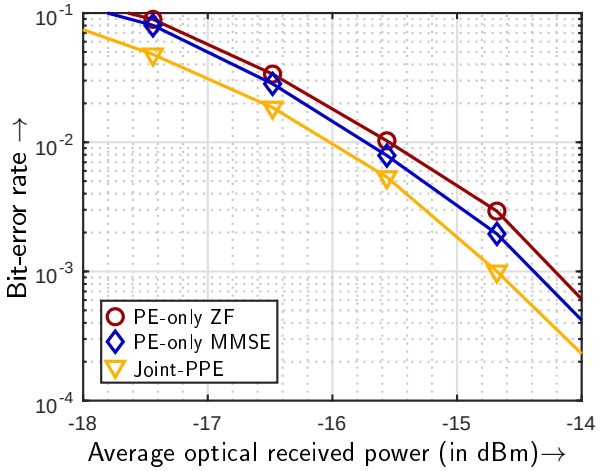

Figure 3.6.: Experimental BER in dependence on the average optical receive power P_{r} comparing the PE-only scheme with the joint-PPE scheme having $L_{\mathrm{p}} = 2$.

by assuming the pre-equalizer as a Dirac delta function. For the joint-PPE scheme, a two-tap pre-equalizer and a post-equalizer with 23 taps are considered for the BER performance. It is evident from Figure 3.6 that the joint-PPE scheme performs the best in comparison to PE-only schemes. The improvement factors to reach a BER of 10^{-3} with the joint-PPE are $\Lambda_{\mathrm{ZF}} = 4.4\,\%$ and $\Lambda_{\mathrm{MMSE}} = 3.5\,\%$. Correspondingly, a better BER performance is yielded using the joint-PPE technique. Hence, the BER improvements from the joint-PPE scheme over PE-only and ZF-PPE schemes is proven using the experimental setup.

3.4. Summary

In this chapter, the main concept of the joint-PPE is formally introduced for the optical SISO system incorporating an MMF channel. An analytical system model with the transmission power constraint is described. With the aid of the theoretical description, the joint-PPE filter is designed and optimized using a nonlinear optimizer. The proposed joint-PPE scheme effectively reduces noise amplification, which results in BER performance enhancement. The efficiency of the joint-PPE is validated using a simulation and an experimental setup. Under the influence of the significant modal dispersion and power constraint, the joint-PPE reduces the average received optical power to reach 10^{-3} BER by 7.3 % and 6.8 % compared to PE-only with ZF and MMSE principles, respectively. These improvements are yielded merely by using a two-tap pre-equalizer at the transmitter side conjugated along with the collectively designed optimal post-equalizer. Therefore, the BER benefits of the joint-PPE are confirmed for the MMF-based SISO system. In order to generate further degree of design freedom, the joint-transceiver scheme is extended to an MIMO technique in the following chapter.

4. Joint-Transceiver Equalizer Design in a MIMO System

In this chapter, the proposed joint-transceiver equalizer is designed for an SDM-based optical MIMO system. The performance of the joint-transceiver scheme is analyzed over the short reach optical interconnects incorporating distinct lengths of the MMF channel. An MMF is preferred over SMF due to its larger core, which enables the utilization of the spatial degree of freedom. Therefore, multiple parallel data channels can be realized using a larger MMF core, which can support up to 100 transverse spatial mode groups [Che14; Sil16; PSV19]. Higher spectral efficiency is achieved by using these parallel data channels. Moreover, MMFs offer cost-effectiveness and simple implementation in an IM/DD system due to higher alignment tolerance than an SMF. However, the modal dispersion and mode-dependent losses adversely affect the available bandwidth distance product in an MMF transmission link [PSV19; Lei18; Agr02].

SDM is a technique for creating multiple data channels by using the transverse spatial extent of an MMF [Ant15]. An SDM-based optical system can be realized by offset light launching conditions or photonic lanterns [Bir15]. The MIMO signal processing technique provides aid to increment the spectral efficiency due to parallel data streams and mode scrambling mitigation [PSV19; Lei18]. A further boost in the spectral efficiency is implemented by using higher-order modulation formats (HOMFs). For this work, PAM-M is considered over SCM [Szc12], CAP [Olm14], or DMT [Wei19; Zha18a] due to better sensitivity regarding the received optical power and simple implementation. The main challenge is compensating the modal dispersion originating from an MMF.

Physical dispersion compensation components, such as FBGs or dispersion compensation fibers, can be utilized. Considering the cost-effectiveness of an IM/DD system, a digital dispersion mitigation procedure using equalization is preferred. A linear MIMO equalizer with the MMSE principle is chosen over a non-linear one due to analytical traceability and comprehensive implementation [Zha18a; Zou19; Zha21]. According to literature, equalizers present at the transmitter and the receiver yield more performance benefits compared to a linear equalizer existing either at the transmitter or at the receiver [Zha21; Guo19; SY04]. State-of-the-art transceiver schemes are implemented over an SMF link or a SISO system with an independent design of a PPE filter [Guo19; Zou19; Tan20]. The reported coefficients of the pre-equalizer are calculated using the ZF design principle. Additionally, a segregated post-equalizer design is incorporated at the receiver. Although PPE schemes exist in the

literature, the experimental efficiency of jointly designed PPE filters over an MMF-based MIMO system still needs to be investigated.
Against this background, a jointly designed transceiver equalization is proposed for an optical MIMO system. The main target of the joint-transceiver scheme is to maximize the BER performance in the presence of an MMF channel, which is considerably impaired with modal dispersion and cross-talk. Hence, an analytical MIMO system model is developed to evaluate the effectiveness of the joint-transceiver scheme in this chapter. The methodology to compute the joint-PPE coefficients is also described in this chapter. In the later section, the potential of the joint-transceiver scheme is experimentally analyzed using 250 m and 1.4 km MMF fiber channels.

4.1. Introduction

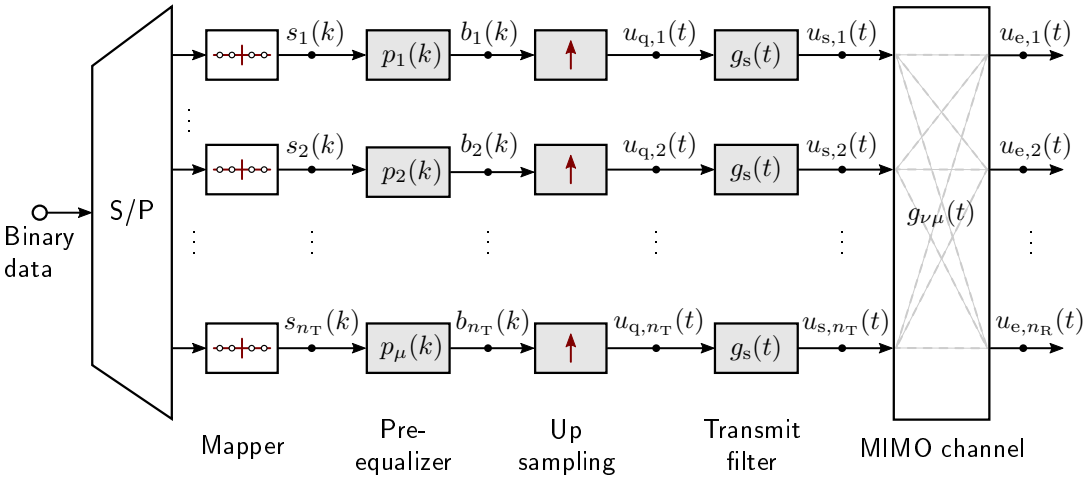

Figure 4.1.: MIMO transmitter and channel structure in continuous time domain.

A generic MIMO transmission model can be segregated into three parts: the transmitter, channel, and receiver. Starting from the transmitter and the channel in Figure 4.1, a serial binary data stream is converted into n_T parallel streams using a serial-to-parallel (S/P) converter. Subsequently, each symbol is mapped using an M_μ-ary PAM constellation format with $\mu = [1, 2, \ldots, n_T]$ using a mapper. The resulting input symbol sequence at the μ-th MIMO input is represented as $s_\mu(k)$. Since this work focuses is on a jointly designed PPE filter, a pre-equalizer $p_\mu(k)$ is incorporated in the transmitter structure. Consequently, the pre-equalized sequence $b_\mu(k)$ at the μ-th MIMO input is defined as

$$b_\mu(k) = s_\mu(k) * p_\mu(k) \ , \tag{4.1}$$

where $*$ is the convolution operator. The pre-equalized sequences are transformed into the continuous time series using a series of Dirac delta pulses, which are represented as

$$u_{\mathrm{q},\mu}(t) = T_{\mathrm{s}} \sum_{k=-\infty}^{+\infty} b_{\mu}[k] \cdot \delta\left(t - kT_{\mathrm{s}}\right) \quad , \tag{4.2}$$

with T_{s} denoting the symbol duration. This process is shown with the upward pointing arrow, which is labeled as an up-sampling block. Consequently, these impulses are shaped according to a transmit filter, and the resulting signal is defined as

$$u_{\mathrm{s},\mu}(t) = u_{\mathrm{q},\mu}(t) * g_{\mathrm{s}}(t) = T_{\mathrm{s}} \sum_{k=-\infty}^{+\infty} b_{\mu}[k] \cdot g_{\mathrm{s}}\left(t - kT_{\mathrm{s}}\right) \quad , \tag{4.3}$$

where the transmit filter is represented with $g_{\mathrm{s}}(t)$. The transmit filter is characterized as a rectangular function, which is given as

$$g_{\mathrm{s}}(t) = \frac{1}{T_{\mathrm{s}}} \cdot \mathrm{rect}\left(\frac{t}{T_{\mathrm{s}}}\right) \quad . \tag{4.4}$$

The transmitted signal $u_{\mathrm{s},\mu}(t)$ propagates through the MIMO channel $g_{\nu\mu}(t)$, which is having a time-varying property. The received signal $u_{\mathrm{e},\nu}(t)$ consists of all the transmitted signals with the channel weighting factor, which is calculated for $\nu = 1, 2, \ldots, n_{\mathrm{R}}$ as

$$u_{\mathrm{e},\nu}(t) = \sum_{\mu=1}^{n_{\mathrm{T}}} u_{\mathrm{s},\mu}(t) * g_{\nu\mu}(t) \quad . \tag{4.5}$$

The MIMO channel introduces the cross-talk between the MIMO inputs, which is named as ICI. Moreover, the frequency-selective behavior of the channel causes the degradation due to ISI. The mitigation of the channel influences is executed using the equalization process.

While propagation through the MIMO channel, the signal is corrupted with the noise $n_{\nu}(t)$. The MIMO receiver is designed to process the received signal, and the structure of the MIMO receiver is illustrated in Figure 4.2. Once the signal is received, the receive filtering $g_{\mathrm{ef}}(t)$ is applied. The resulting received filtered signal $u_{\mathrm{ef},\nu}(t)$ can be written as

$$u_{\mathrm{ef},\nu}(t) = T_{\mathrm{s}} \sum_{\mu=1}^{n_{\mathrm{T}}} \sum_{k=-\infty}^{+\infty} b_{\mu}[k]\, h_{\nu\mu}\left(t - kT_{\mathrm{s}}\right) + w_{\nu}(t) \quad . \tag{4.6}$$

In (4.6), the filters with channel and the receive filtered noise $w_{\nu}(t)$ are summarized as

$$h_{\nu\mu}(t) = g_{\mathrm{s}}(t) * g_{\nu\mu}(t) * g_{\mathrm{ef}}(t) \quad \text{and} \quad w_{\nu}(t) = n_{\nu}(t) * g_{\mathrm{ef}}(t) \quad . \tag{4.7}$$

In a later stage, the signal undergoes down sampling and post-equalization $f_{\nu\mu}(k)$, which will compensate all the interference effects. Subsequently, a hard decision is conducted to

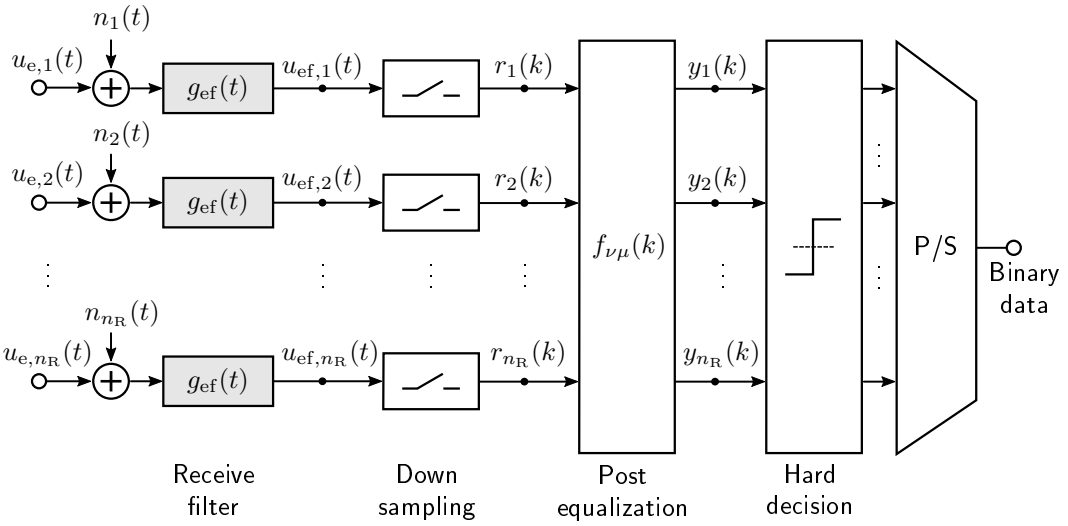

Figure 4.2.: MIMO transmitter and channel structure.

estimate the parallel binary data streams. Consequently, these bit streams are converted into serial data using a parallel-to-serial (P/S) converter. Finally, the system performance can be evaluated using key performance indicators such as BER or eye-openings.

4.2. MIMO System Model

A system model in the discrete-time domain is represented in Figure 4.3, which emphasizes on the implementation of the pre- and post-equalizer scheme. In Figure 4.3, a MIMO system

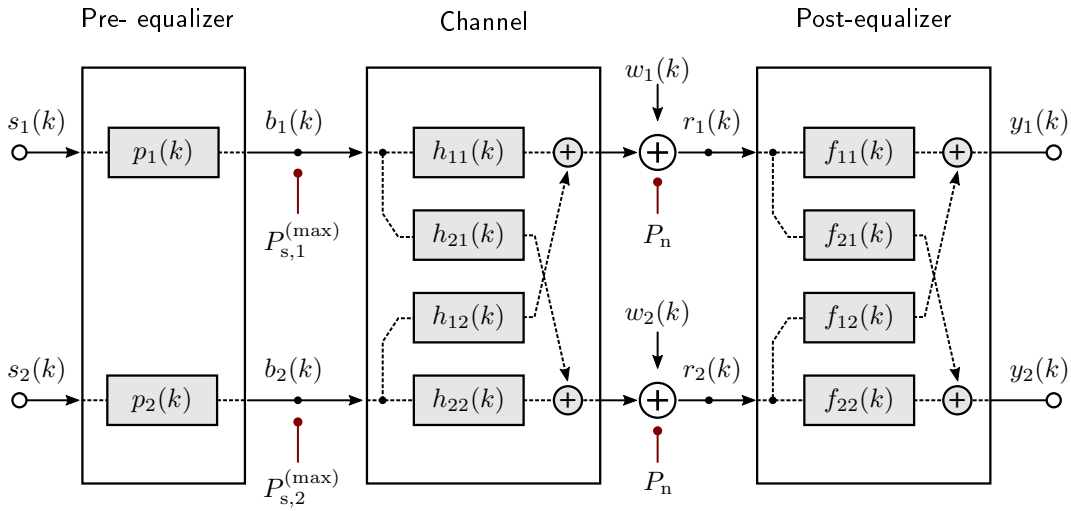

Figure 4.3.: Block diagram of electrical (2×2) MIMO system model with pre- and post-equalizer filters in discrete-time domain representation.

consists of two MIMO inputs n_{T} and two MIMO outputs n_{R}. The construction of the system model is segregated into three parts, which will describe the signal flow at the transmitter, channel, and receiver. The major functions of a MIMO transmitter are parallelization of the serial binary data, symbol mapping, and pre-equalization. A S/P conversion is applied to encoded serial binary data, which results in n_{T} parallel data streams. Subsequently, these data streams are mapped onto a M_μ-ary PAM format with $\mu = [1, 2, \ldots, n_{\mathrm{T}}]$. Afterwards, the parallel symbol streams $s_\mu(k)$, where $k \in \mathbb{N}$, are generated. These symbol streams are Gray-coded for improved system performance. The transmit signal space for the selected M_μ-ary PAM is defined as

$$s_\mu[k] \in \{s_{\mu,0}, s_{\mu,1}, \ldots, s_{\mu,m}\}, \qquad \text{where } m = M_\mu - 1 \ . \tag{4.8}$$

The symbols are independent and identically distributed. The amplitude of these symbols is given as

$$s_{\mu,m} = \left(\frac{m}{M_\mu - 1}\right) \cdot P_{\mathrm{s},\mu}^{(\max)}, \qquad \text{where } M_\mu \neq 1 \text{ and } m = [0, 1, \ldots, M_\mu - 1] \ . \tag{4.9}$$

In (4.9), the symbol amplitudes are defined with respect to the maximum transmission power $P_{\mathrm{s},\mu}^{(\max)}$ at the μ-th MIMO input. The following step is the pre-equalization of these symbols. Thus, the pre-equalizer $p_\mu(k)$ is applied to the input signal $s_\mu(k)$ at μ-th MIMO input, resulting in a multi-level signal $b_\mu(k)$. The number of distinct amplitudes N_μ of $b_\mu(k)$ is dependent upon the number of pre-equalization coefficients L_{p}, which can be expressed as $L_{\mathrm{p}} = \log_2(N_\mu)$. The pre-equalized signal $b_\mu(k)$ is transmitted through the channel. Prior to the transmission, the amplitude of the transmitted signal is obligated to follow the power constraint, which is expressed as

$$s_{\mu,M_\mu-1} = b_{\mu,N_\mu-1} = q \cdot P_{\mathrm{s},\mu}^{(\max)} \ , \tag{4.10}$$

with q denoting the electrical to optical conversion factor. It is worth noting that the analog/digital conversion (ADC) process is considered ideal, and the peak-to-average ratio is maintained to be constant.

The transmitted signal propagated through the channel $h_{\nu\mu}(k)$ with $\nu = [1, 2, \ldots, n_{\mathrm{R}}]$, which is characterized as frequency-selective. Practically, the channel is represented as an MMF, where the data streams are transmitted using different excited mode groups. While propagation, the transmitted signal undergoes degradation due to ICI and ISI. The temporal pulse broadening occurs due to $h_{\nu\mu}(k)$. Furthermore, the noise $w_\nu(k)$ is added to the signal with P_{n} noise power, which further degrades the system performance.

At the MIMO receiver, the transmitted signal, deteriorated by the channel, is received, which is expressed as $r_\nu(k)$. Subsequently, the residual interference is compensated using

a post-equalizer $f_{\nu\mu}(k)$. Finally, the $y_\nu(k)$ is estimated, and the system performance is evaluated.

Analytical Description

The purpose of the analytical description of the system model is to outline the noise amplification due to post-equalization. Moreover, the benefits of a few-tap pre-equalizer are studied regarding the effective mitigation of channel impairments and reduction in noise amplification. The analytical representation of the provided system model is given as

$$\boldsymbol{r} = \boldsymbol{H} \cdot \boldsymbol{b} + \boldsymbol{w} \ , \tag{4.11}$$

where $\boldsymbol{r}$ is the $(n_\mathrm{R} \times 1)$ received vector, which consists of the channel degraded transmitted signal and the noise vector $\boldsymbol{w}$ with a $(n_\mathrm{R} \times 1)$ dimension. In (4.11), the channel matrix $\boldsymbol{H}$ with $(n_\mathrm{R} \times n_\mathrm{T})$ is described as

$$\boldsymbol{H} = \begin{bmatrix} \boldsymbol{H}_{1\,1} & \cdots & \boldsymbol{H}_{1\,n_\mathrm{T}} \\ \vdots & \ddots & \vdots \\ \boldsymbol{H}_{n_\mathrm{R}\,1} & \cdots & \boldsymbol{H}_{n_\mathrm{R}\,n_\mathrm{T}} \end{bmatrix} \ , \tag{4.12}$$

with $\boldsymbol{H}_{n_\mathrm{R}\,n_\mathrm{T}}$ denoting an individual SISO channel matrix, which affects the pre-equalized transmitted signal vector $\boldsymbol{b}$. The signal vector $\boldsymbol{b}$ with dimensions $(n_\mathrm{T} \times 1)$ is decomposed as

$$\boldsymbol{r} = \boldsymbol{H} \cdot \boldsymbol{P} \cdot \boldsymbol{s} + \boldsymbol{w} \ , \tag{4.13}$$

where $\boldsymbol{P}$ represents the pre-equalizer $(n_\mathrm{T} \times n_\mathrm{T})$. In order to restrain the complexity at the transmitter side, $\boldsymbol{P}$ is considered a diagonal matrix. The input signal vector is defined as $\boldsymbol{s}$ with $(n_\mathrm{T} \times 1)$ dimensions. Finally, the post-equalization is applied, and it is expressed as

$$\begin{aligned} \boldsymbol{y} &= \boldsymbol{F} \cdot \boldsymbol{r} \ , \\ \boldsymbol{y} &= \underbrace{\boldsymbol{F} \cdot \boldsymbol{H} \cdot \boldsymbol{P}}_{\text{Term 1}} \cdot \boldsymbol{s} + \underbrace{\boldsymbol{F} \cdot \boldsymbol{w}}_{\text{Term 2}} \ , \end{aligned} \tag{4.14}$$

where $\boldsymbol{F}$ is the post-equalizer with $(n_\mathrm{R} \times n_\mathrm{R})$ dimensions. In (4.14), the first term describes that the channel influence can be mitigated by collectively using the pre- and post-equalizer to recover the transmitted signal. The noise amplification effect by using a post-equalizer is clearly depicted with the second term. Thus, the equalization efforts can be shifted to the transmitter side by using a pre-equalizer to enhance the system performance. Since a low-cost IM/DD system is required, a few-tap pre-equalizer is suggested for the joint-PPE

scheme. The noise enhancement from the second term in (4.14) is quantified as

$$\theta_{\mu} = \sum_{\nu=1}^{n_{\mathrm{R}}} \sum_{k=0}^{L_{\mathrm{f}}-1} |f_{\mu\nu}[k]|^2, \qquad \text{for } \mu = 1, 2, \ldots, n_{\mathrm{T}} \ , \tag{4.15}$$

where the NWF is represented by θ_{μ} at the μ-th MIMO input. The variable L_{f} is the length of the post-equalizer, and $f_{\mu\nu}[k]$ is the amplitude of the k-th post-equalization coefficient. From (4.15), it is clear that the NWF is directly proportional to the amplitude of post-equalizer coefficients. Hence, the impact of the NWF on the system performance is evaluated in the subsequent part.

Quality Criteria

The noise amplification effect of the post-equalizer degrades the transmission quality, which affects the overall BER performance. At the μ-th MIMO input, the transmission quality ϱ_{μ} is calculated as

$$\varrho_{\mu} = \frac{U_{\mathrm{A},\mu}^2}{\widetilde{P}_{\mathrm{n},\mu}} \ , \tag{4.16}$$

with denoting the variable $U_{\mathrm{A},\mu}$ is the half-vertical eye-opening and the noise power after the post-equalizer is depicted with $\widetilde{P}_{\mathrm{n},\mu}$. The relation between $\widetilde{P}_{\mathrm{n},\mu}$, and the NWF can be defined as

$$\widetilde{P}_{\mathrm{n},\mu} = \theta_{\mu} \cdot P_{\mathrm{n}} \ . \tag{4.17}$$

From combination of (4.15) and (4.17), the resulting transmission quality is calculated as

$$\varrho_{\mu} = \frac{U_{\mathrm{A},\mu}^2}{\widetilde{P}_{\mathrm{n},\mu}} = \frac{U_{\mathrm{A},\mu}^2}{\theta_{\mu} \cdot P_{\mathrm{n}}} = \frac{U_{\mathrm{A},\mu}^2}{\sum_{\nu=1}^{n_{\mathrm{R}}} \sum_{k=0}^{L_{\mathrm{f}}-1} |f_{\mu\nu}[k]|^2 \cdot P_{\mathrm{n}}} \ . \tag{4.18}$$

From (4.18), the adverse effect of post-equalization coefficients over transmission quality is shown, where the transmission quality will increase with limited usage of the post-equalization. It is worth noting that BER can only be calculated with complete mitigation of ISI and ICI. Consequently, the MIMO input-specific BER $P_{\mathrm{BER}}^{(\mu)}$ is given as

$$P_{\mathrm{BER}}^{(\mu)} = \frac{1}{\log_2(M_{\mu})} \left(\frac{M_{\mu} - 1}{M_{\mu}} \right) \operatorname{erfc}\left(\sqrt{\frac{\varrho_{\mu}}{2}} \right) \ , \tag{4.19}$$

with $\operatorname{erfc}(\cdot)$ denoting the complementary error function. By combining (4.19) with (4.18), the BER depending upon the NWF is formulated as

$$P_{\mathrm{BER}}^{(\mu)} = \frac{1}{\log_2(M_{\mu})} \left(\frac{M_{\mu} - 1}{M_{\mu}} \right) \operatorname{erfc}\left(\sqrt{\frac{U_{\mathrm{A},\mu}^2}{2 \cdot \theta_{\mu} \cdot P_{\mathrm{n}}}} \right) \ . \tag{4.20}$$

In conclusion, this section demonstrates that the system performance will deteriorate due to noise amplification caused by the amplitude of the post-equalizer coefficients. Thus, using a well-designed pre-equalizer, the BER performance can be improved by pre-compensating the channel influence.

4.3. Joint-Transceiver Equalizer Design for MIMO Systems

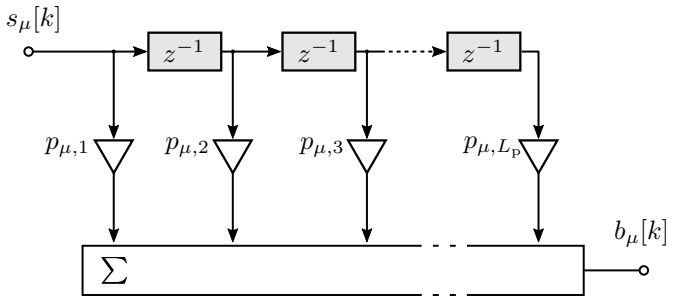

Figure 4.4.: The structure of a linear FIR pre-equalizer filter, where the delay by one symbol is denoted by z^{-1}.

The primary target of the joint-transceiver equalizer is to pre-compensate major channel impairments using multi-level signaling from a few-tap pre-equalization. Afterward, the residual channel interference should be mitigated using minimal post-equalization efforts, resulting in the reduction of noise amplification. The pre-equalizer is designed using a linear FIR structure, which is illustrated in Figure 4.4. The pre-equalized signal $b_\mu(k)$ at the μ-th MIMO input is given as

$$b_\mu[k] = \sum_{i=1}^{L_\mathrm{p}} p_{\mu,i} \cdot s_\mu\left[k-(i-1)\right], \qquad \text{where } \mu = 1, 2, \ldots, n_\mathrm{T} \ . \tag{4.21}$$

In (4.21), the i-th coefficient of the pre-equalizer is represented using $p_{\mu,i}$. The target is to calculate the pre-equalizer coefficients $p_\mu(k)$ to aid the system performance. Consequently, the post-equalization filter coefficients should be computed in conjunction with the pre-equalizer. Therefore, a numerical constraint optimization, namely an interior point algorithm, is utilized to design and optimize the PPE filter [Ste04; Wol11]. The optimization

statement with constraints is provided as

$$\begin{aligned} &\underset{p_\mu(k),\, f_{\nu\mu}(k)}{\text{minimize}} && \theta_\mu(h_{\nu\mu}(k)), && \nu = 1, 2, \ldots, n_{\mathrm{R}} \\ &\text{subject to} && \boldsymbol{F} \cdot \boldsymbol{H} \cdot \boldsymbol{P} - \boldsymbol{I} = 0 \ , \\ &\text{and} && s_{\mu, M_\mu - 1} - q \cdot P_{\mathrm{s},\mu}^{(\max)} = 0 \ . \end{aligned} \tag{4.22}$$

In (4.22), the minimization of NWF is considered as the objective function. The PPE filter coefficients are calculated at the global minimum point of NWF depending upon the given channel. The objective function is subjected to interference mitigation and power constraints. The complete compensation of the channel interference is confirmed from the first constraint, where $\boldsymbol{I}$ is the identity matrix. The maximum transmission power is provided to the highest transmitted symbol in the following constraint, which is also mentioned in (4.10).

The primal optimization statement, as formulated in (4.22), is solved using duality optimization. Thus, the constraints are incorporated into the objective function, and the modified objective statement is written as

$$\min_{p_\mu(k),\, f_{\nu\mu}(k)} \theta_\mu(h_{\nu\mu}(k)) + \max_{\alpha,\, \beta} \ \left((\boldsymbol{F} \cdot \boldsymbol{H} \cdot \boldsymbol{P} - \boldsymbol{I}) \cdot \alpha + \left(s_{\mu, M_\mu - 1} - q \cdot P_{\mathrm{s},\mu}^{(\max)} \right) \cdot \beta \right) \ , \tag{4.23}$$

where the scalar slopes of the penalty function are represented with variables α and β. The characteristic of the penalty function is to penalize the objective function when the constraints are not obeyed. Similarly, when the objective function starts converging towards minimizing the NWF, the penalties are converted into rewards for the objective function. Since the minimization and maximization functions are introduced, the objective function in (4.23) is converted into the duality problem. The duality-based objective function is defined as

$$\max_{\alpha,\, \beta} \ \min_{p_\mu(k),\, f_{\nu\mu}(k)} \ \left(\theta_\mu(h_{\nu\mu}(k)) + (\boldsymbol{F} \cdot \boldsymbol{H} \cdot \boldsymbol{P} - \boldsymbol{I}) \cdot \alpha + \left(s_{\mu, M_\mu - 1} - q \cdot P_{\mathrm{s},\mu}^{(\max)} \right) \cdot \beta \right) \ . \tag{4.24}$$

The provided objective function is solved using the Lagrangian solver. The optimal coefficients for the PPE filter are obtained using the Lagrangian multiple with the following condition

$$\nabla \left(\theta_\mu(h_{\nu\mu}(k)) + (\boldsymbol{F} \cdot \boldsymbol{H} \cdot \boldsymbol{P} - \boldsymbol{I}) \cdot \alpha + \left(s_{\mu, M_\mu - 1} - q \cdot P_{\mathrm{s},\mu}^{(\max)} \right) \cdot \beta \right) = 0 \ . \tag{4.25}$$

The strong duality between the primal and dual problem should be maintained in order to obtain the same optimal solution. Thus, Karush-Kuhn-Tucker (KKT) optimality conditions

are formulated for strong duality, which are provided as

$$\begin{aligned}
(\boldsymbol{F}\cdot\boldsymbol{H}\cdot\boldsymbol{P}-\boldsymbol{I})\cdot\alpha &= 0 \ , \\
\left(s_{\mu,M_\mu-1}-q\cdot P_{\mathrm{s},\mu}^{(\max)}\right)\cdot\beta &= 0 \ , \\
\alpha &\geq 0 \ , \\
\beta &\geq 0 \ , \\
\boldsymbol{F}\cdot\boldsymbol{H}\cdot\boldsymbol{P}-\boldsymbol{I} &= 0 \ , \\
s_{\mu,M_\mu-1}-q\cdot P_{\mathrm{s},\mu}^{(\max)} &= 0 \ .
\end{aligned} \tag{4.26}$$

The solution of this optimization problem is controlled by a variable γ, with $\gamma \in \mathbb{N}$. The variable γ refers to the positive number for regulating the degree of perturbation to achieve the optimal solution. The adapted constraints from (4.26) using γ are given as

$$\begin{aligned}
\alpha &= \frac{\gamma_1}{(\boldsymbol{F}\cdot\boldsymbol{H}\cdot\boldsymbol{P}-\boldsymbol{I})} \ , \\
\beta &= \frac{\gamma_2}{\left(s_{\mu,M_\mu-1}-q\cdot P_{\mathrm{s},\mu}^{(\max)}\right)} \ .
\end{aligned} \tag{4.27}$$

Since two constraints ($i = 2$) are subjected to the optimization statement, the zero duality gap is achieved with the condition $\gamma_i \to 0$, $\forall i$. In accordance to (4.25), (4.26) and (4.27), the final optimization problems with the modified constraints is written as

$$\nabla\left(\theta_\mu(h_{\nu\mu}(k))+\gamma_1\cdot\log\left(\boldsymbol{F}\cdot\boldsymbol{H}\cdot\boldsymbol{P}-\boldsymbol{I}\right)+\gamma_2\cdot\log\left(s_{\mu,M_\mu-1}-q\cdot P_{\mathrm{s},\mu}^{(\max)}\right)\right)=0 \ . \tag{4.28}$$

Finally, the analytical center of the feasible region is discovered using the large values of γ_i with a Newton solver. Subsequently, the optimal solution is achieved with a decrement of γ_i in the given statement.

4.4. Experimental Optical MIMO Setup with Mach-Zehnder Modulators

In this section, an experimental SDM-based MIMO setup is developed using MZMs, which is demonstrated in Figure 4.5. The experimental setup includes the MIMO transmitter, an MMF channel, and the MIMO receiver. Starting with the MIMO transmitter, a serial data stream is converted into parallel input data sequences using a S/P converter. These data sequences are corresponding to PRBSs. Consequently, these PRBSs are mapped onto the Gray-coded symbols in accordance to the selected M_μ-ary PAM formats at the μ-th MIMO input. The pilot sequences are also included with these symbols to facilitate the purpose of channel estimation. Since the experimental setup incorporates the joint-PPE setup, the input symbols are pre-equalized using the computed pre-equalizer from the optimization

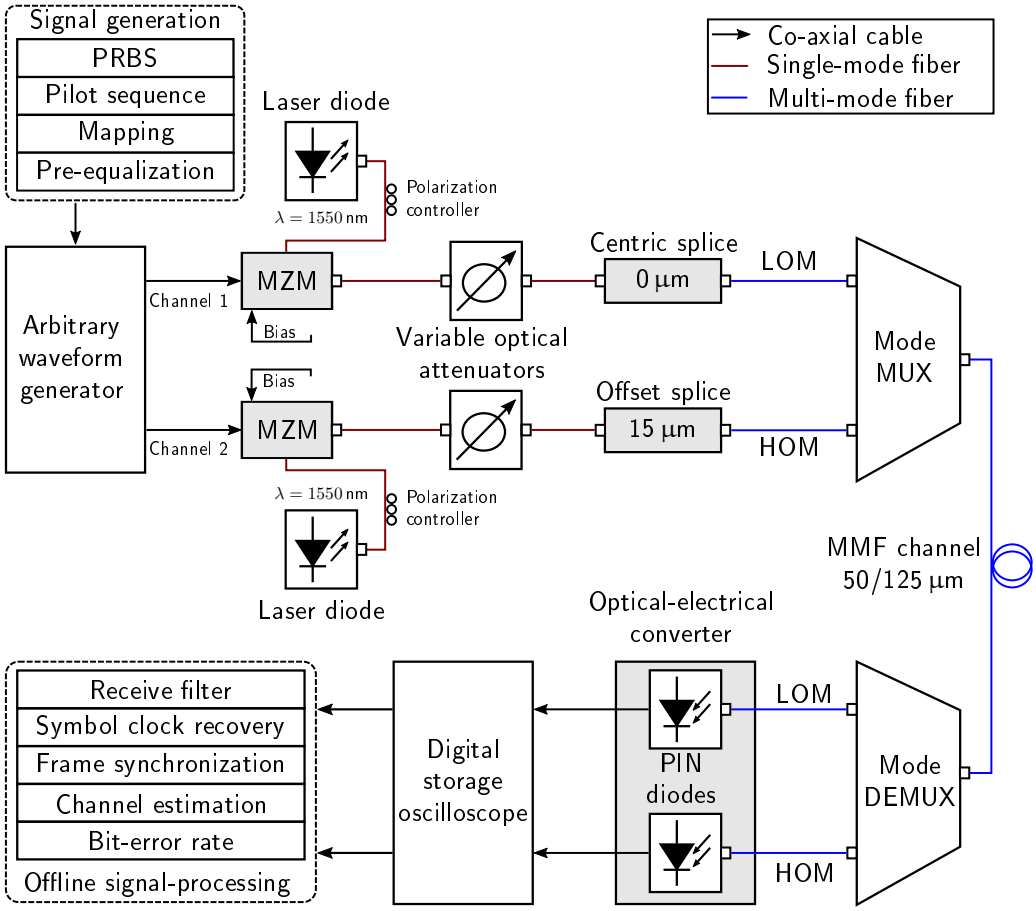

Figure 4.5.: Experimental setup for the joint-PPE scheme by using an optical MIMO system with an MMF channel.

statement. While initializing the experimental setup for PE-only implementation, the pre-equalizer is considered as a Dirac delta function. Once the signal generation is completed, an arbitrary waveform generator (AWG) is utilized to produce the electrical signal in accordance to the rectangular transmit filter. Subsequently, the electrical signal is transformed into the optical domain using the chirp-free $LiNbO_3$ MZMs. The carrier laser source is operating at a wavelength of 1550 nm. The optical signals then travel to the VOAs, which are used to estimate the system performance over a distinct range of the average optical received power P_r. Afterwards, the SDM configuration is realized using the offset launching conditions. The first MIMO input is provided with a centric splice, which launches the light into the core center of an MMF. Similarly, an offset splice is used to launch the light with a 15 µm offset from the core center. The configuration of such an SDM-based MIMO system is demonstrated in Figure 4.6. The measured mean power distribution with centric and eccentric light launching conditions are shown in Figure 4.6b and Figure 4.6c, respectively. The

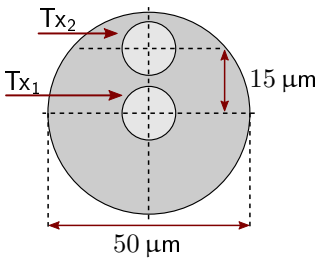

(a) Light launching condition at the MMF core

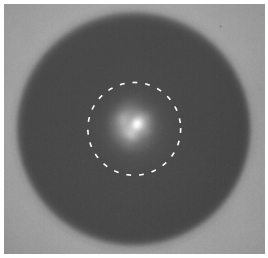

(b) Centric light launching condition at the first transmitter Tx_1

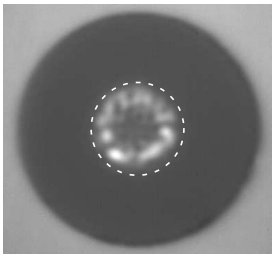

(c) 15 µm offset light launching condition at the second transmitter Tx_2

Figure 4.6.: Transmitter's configuration to enable SDM by offset light launching conditions in the MMF core.

formal and latter launching conditions excite the lower-order modes (LOMs) and high-order modes (HOMs) into an MMF core. At the end of the MIMO transmitter, these excited mode groups are multiplexed using a custom-made fusion coupler, which is labeled as mode MUX [SAL14]. From Figure 4.7, an X-shaped mode MUX structure is utilized to combine the mode groups with each other. The LOMs are activated due to centric light launching conditions into an MMF core center. Hence, LOMs are more likely to travel in a transverse direction only. On the other hand, the HOMs couple with LOMs due to their wider electric field distribution. A slight asymmetric power split ratio is utilized, which is well suitable for the multiplexing application. The power splitting ratio of 45% with $\approx 3\,\mathrm{dB}$ of insertion loss is incurred by the mode MUX.

The optical signal is propagated through an MMF channel. The transmitted signal undergoes ISI and ICI due to the presence of an MMF channel. The mode-dependent losses are caused by the SDM configuration. The channel characteristics are measured using the appended pilot symbols at the MIMO receiver. Most importantly, the compensation of channel impairments is the primary focus of the digital equalization schemes. The challenge of recovering the transmitted signal is dealt with at the MIMO receiver.
At the MIMO receiver, the received optical signal is detected by using an MMF PIN diode at each MIMO output. In these PIN diodes, trans-impedance amplifiers are integrated to

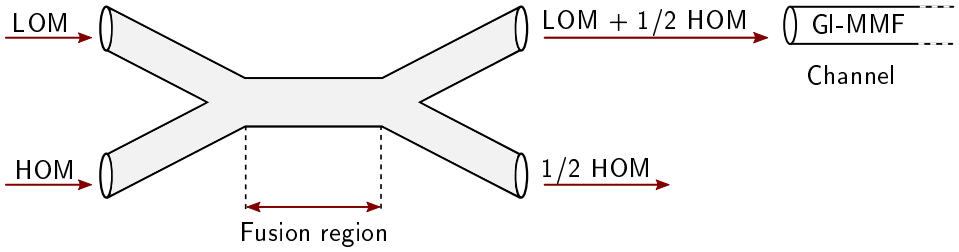

Figure 4.7.: Ideal mode MUX application of a fusion coupler and GI-MMF channel.

convert the generated photocurrent into electrical potential and amplify the latter. The large detection surfaces of these PIN diodes are responsible for an inherent increase in the capacitance, resulting in the degradation of the receiver's sensitivity. Consequently, the electrical signals are captured using a multi-channel DSO, which uses 40 GSa/s at a bandwidth of 13.6 GHz. This captured signal undergoes an offline signal processing chain with one sample per symbol. The first stage consists of receive filtering, where a rectangular filter similar to the transmit filter is deployed. Subsequently, down-sampling and symbol clock recovery are conducted on the signal, followed by the frame synchronization. An open loop timing recovery algorithm is utilized to compute the exact sampling time of the received signal. Additionally, the boundaries of each frame are calculated using a fine-timing acquisition algorithm in which the correlation between the received signal and the pilot sequence is computed. Afterward, a least-square algorithm is utilized to estimate the eigenvalues of the channel impulse response with each other. Finally, the BER performance of the different equalization schemes is calculated and compared. The reliability of the experimental setup is ensured by transmitting at least 74 frames on each MIMO input, which implies the transmission of five million bits at each MIMO input. It is worth noting that the forward error correction decoding is not incorporated at the receiver. A pictorial representation of the experimental setup is also shown in Figure 4.8.

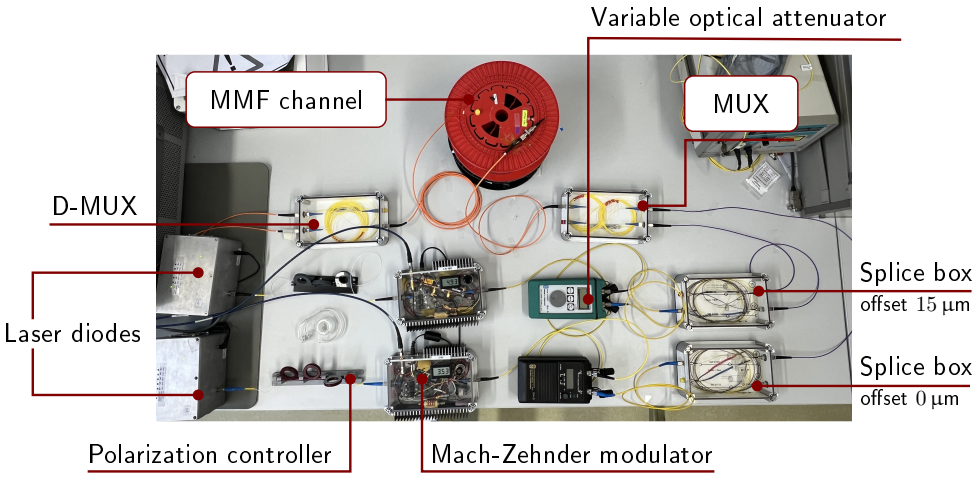

Figure 4.8.: Experimental setup of (2×2) optical MIMO system using Mach-Zehnder modulators.

4.5. Partial Joint-Transceiver Equalization with a 250 m Multi-Mode Fiber

This section outlines a partial joint-transceiver scheme in which only one of the MIMO inputs is pre-equalized. This method is applied to limit the transmitter's complexity. The

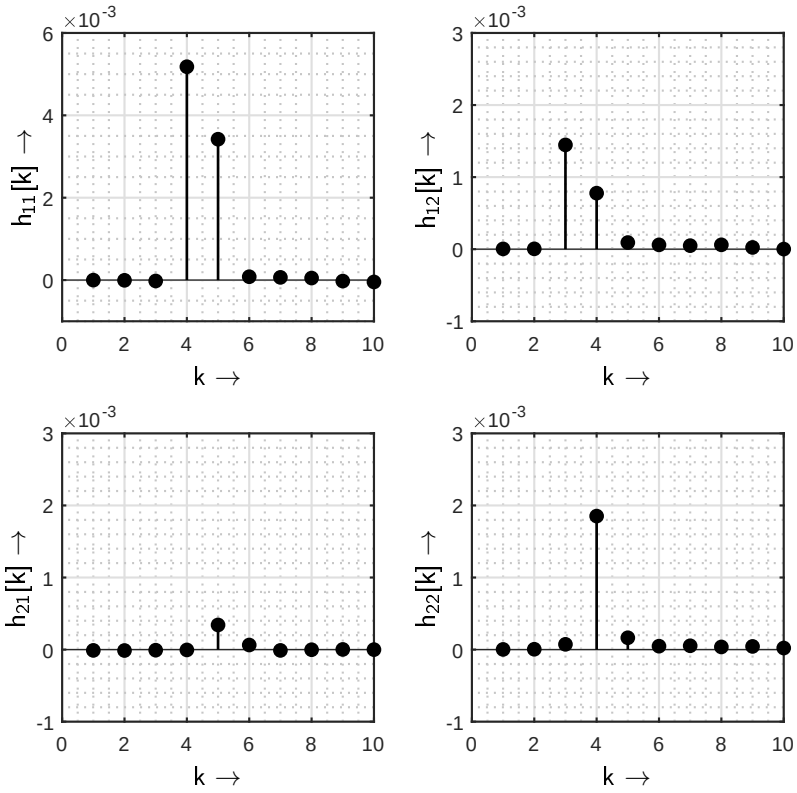

Figure 4.9.: Measured channel impulse response of a 250 m long MMF with respect to the symbol rate $f_{\mathrm{T}} = 1/T_{\mathrm{s}} = 2.5$ GBd per MIMO input at an operating wavelength of 1550 nm.

joint-transceiver equalization is analyzed over a (2×2) MIMO system using a 250 m long MMF channel. The benefits of a joint-transceiver equalizer design are computed using Monte Carlo simulations and an experimental setup. The measured channel state information of a 250 m long MMF at 2.5 GBd per MIMO input is shown in Figure 4.9. The direct channel components, $h_{\nu\mu}(k)$ when $\nu = \mu$, are degraded with ISI due to differential mode group delays. Moreover, the cross-talk between the MIMO inputs, $h_{\nu\mu}(k)$ when $\nu \neq \mu$, while propagating through the channel is considerable. The dispersion impairments and mode-dependent losses are effectively mitigated using the proposed joint-transceiver equalizer design. Moreover, the BER performances of different equalization schemes, such as PE-MMSE and PE-ZF, are compared with the joint-transceiver equalization.

4.5.1. Simulation Results

The discrete-time Monte Carlo simulation is implemented using the provided MIMO system model. The simulations are conducted in three sequential steps. In the first step, the BER performances of PE-only with MMSE and ZF equalization principles are computed while

Table 4.1.: An overview of different equalization methods.

Equalization acronym	Equalization principle
PE-ZF	ZF-based post-equalizer only
PE-MMSE	MMSE-based post-equalizer only
ZF-PPE	ZF-based pre-equalizer and MMSE-based post-equalizer
Joint-PPE	Jointly designed pre- and post-equalizer

considering the pre-equalizer as a Dirac delta function. This step also estimates the MMF channel using the pilot-based least-square algorithm. The following step includes designing and optimizing the PPE coefficients using the estimated channel. In the final step, the performance of joint-transceiver equalization is analyzed and compared. A brief overview of different equalizers is provided in Table 4.1. Moreover, an improvement factor related to NWF is introduced, which is given as

$$\mathrm{IF}_{\mu} = \frac{\theta_{\mu}^{(\mathrm{PE-ZF})} - \theta_{\mu}^{(\mathrm{PPE})}}{\theta_{\mu}^{(\mathrm{PE-ZF})}} \ , \tag{4.29}$$

where IF_{μ} is the improvement factor at the μ-th MIMO input. A higher value of IF_{μ} corresponds to a better improvement in the BER performance. The simulations are conducted with two types of joint-transceiver equalizer design: comprehensive and partial joint-PPE. In a comprehensive joint-PPE scheme, all the MIMO inputs undergo jointly designed pre- and post-equalization.

Comprehensive Joint-Transceiver Equalizer Design

The simulation results after following the sequential steps and using the pre-equalization on both MIMO inputs are presented in Figure 4.10. The input-specific and overall system BER performances of the PE-only and joint-PPE schemes are calculated. In Figure 4.10a, the input-specific BER results are shown over the first and the second MIMO inputs in green and gray colors, respectively. It is evident that the joint-PPE outperforms the PE-MMSE and PE-ZF on both inputs. Consequently, the overall BER performance is improved by using the joint-PPE scheme compared to PE-only schemes. SNR gains of $\approx 2.35\,\mathrm{dB}$ with joint-PPE are achieved to reach a BER of 10^{-3} in comparison to the PE-MMSE. Moreover, the average improvement factor on both the MIMO inputs is 39.85 %. The results confirm that the joint-PPE yields benefits in system performance by reduction in noise amplification.

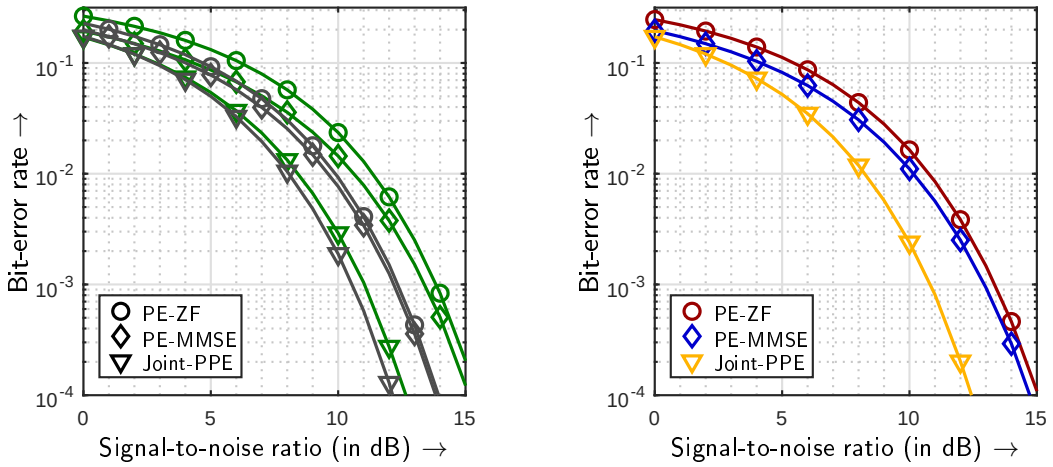

(a) MIMO input specific BER. (b) Overall system BER.

Figure 4.10.: Simulated BER in dependence on the SNR with PE-only and joint-PPE scheme. The MIMO input specific BERs of the first and second inputs are shown in green and gray color, respectively.

Partial Joint-Transceiver Equalization

When the trade-off between the transmitter's complexity and maximizing the system performance is taken into consideration, the pre-equalization present only at one of the MIMO inputs is preferred. Hence, the partial implementation of the joint-PPE scheme is conducted only on one of the MIMO inputs. The overall system BERs are demonstrated in Figure 4.11,

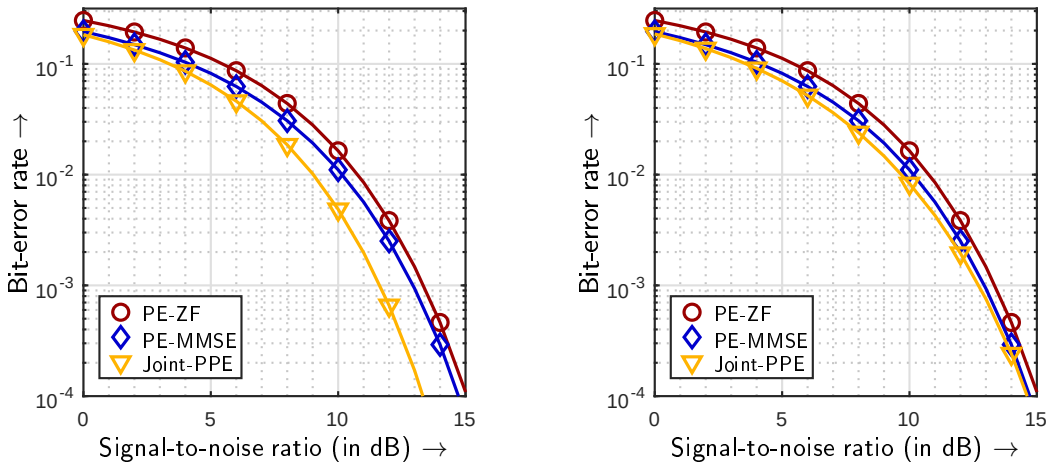

(a) Partial joint-PPE on the first input only. (b) Partial joint-PPE on the second input only.

Figure 4.11.: Simulated overall BER in dependent on the SNR using the partial joint-transceiver equalizer design.

Table 4.2.: Simulated improvement factors of a (2×2) MIMO system comparing PE-ZF with the joint-PPE scheme.

Equalization method	Multi-level signaling at MIMO inputs	L_p	L_f	IF_1 (in %)	IF_2 (in %)
PE-ZF	-	-	25	-	-
Joint-PPE	Both inputs	2	23	45.8	33.9
Partial joint-PPE	First input	2	23	45.1	4.45
Partial joint-PPE	Second input	2	23	1.18	29.4

where the partial joint-PPE scheme is implemented. When the partial joint-PPE is applied to the first MIMO input, an SNR gain of $\approx 1.6\,\mathrm{dB}$ is obtained to reach 10^{-3} BER compared to PE-MMSE. Moreover, the overall NWF improvement factor exhibits a gain of 24.8 %. The benefits are gained due to an effective mitigation of the cross-talk from $h_{12}(k)$ and ISI from $h_{11}(k)$. On the contrary, an SNR gain of just $\approx 0.45\,\mathrm{dB}$ to reach 10^{-3} BER and an average improvement factor of 15.3 % are achieved with partial joint-PPE at the second input. These results are summarized in Table 4.2.

From the simulation evaluation, the joint-PPE surpasses the PE-MMSE and PE-ZF in terms of the BER performance. The simulation results show that the comprehensive joint-PPE scheme achieves the best performance, i.e., multi-level signaling on both MIMO inputs. However, the partial joint-PPE scheme with multi-level signaling only on the first input should be preferred as it achieves nearly similar performance gains as a comprehensive joint-PPE scheme with minimal increment in the transmitter's complexity. Therefore, the potential of partial joint-PPE is explored in the following experimental setup.

4.5.2. Experimental Results

The experimental BER performance of the partial joint-PPE scheme is conducted using the setup as illustrated in Figure 4.5. The BER performances of different equalization schemes are evaluated with respect to the average received optical power P_r at 2.5 GBd per input. The power improvement factor, as mentioned in (3.10), is utilized to validate the competence of the joint-PPE scheme. The power improvement factors to achieve a BER of 10^{-3} are calculated as $\Lambda_\mathrm{MMSE} = 2.7$ % and $\Lambda_\mathrm{ZF} = 3.8$ %. Moreover, the joint-PPE scheme with multi-level signaling only on the first input achieves the lowest BER compared to PE-MMSE and PE-ZF. In the analyzed scenario, the experimental results verify the advantages of the partial joint-PPE scheme.

In summary, the performance of the partial joint-transceiver equalization design with a 250 m long MMF channel is discussed in this section. The benefits of the proposed joint-transceiver scheme are experimentally demonstrated in a (2×2) SDM-based MIMO configuration. The results clearly indicate that the joint-PPE scheme effectively mitigates the dispersion impair-

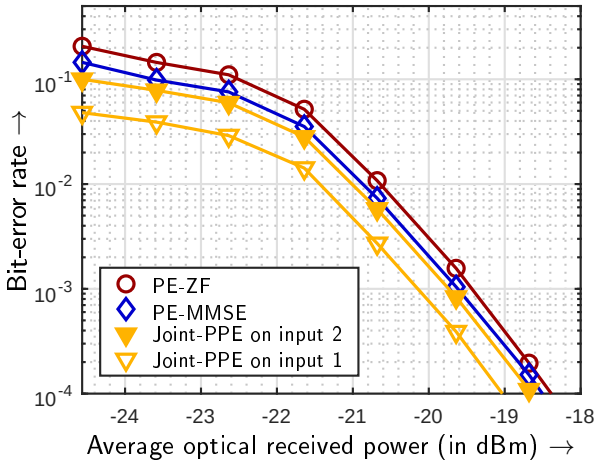

Figure 4.12.: Measured overall system BER in dependence on the average optical received power P_r over the measured channel with PE-only and proposed joint-PPE filter. The hollow and filled yellow markers represent the joint-PPE only on first and second layer, respectively.

ments and channel cross-talk. Moreover, the joint-PPE experimental results have proven beneficial in improving the BER performance with minimal increment in the transmitter's complexity.

4.6. Joint-Transceiver Equalization with a 1.4 km Multi-Mode Fiber

The partial joint-PPE equalizer design has proved beneficial under the analyzed scenario. Thus, the joint-transceiver equalizer design is further investigated with a higher bit-rate of 5 GBd per MIMO input and a longer MMF channel of 1.4 km length. In this section, the benefits of the joint-PPE technique are compared with the ZF-based PPE and PE-MMSE schemes. These equalization techniques incorporate the provided system model and experimental setup using PAM-2 and PAM-4 formats.

The measured channel impulse response is demonstrated in Figure 4.13. The channel is estimated using the appended pilot symbols to the data frames. It is evident that the MMF channel of 1.4 km is significantly degraded in comparison to the previously mentioned 250 m long MMF channel in Figure 4.9. The direct channel components, $h_{\nu\mu}(k)$ when $\nu = \mu$, are considerably deteriorated with the time dispersiveness characteristic of the MMF channel. Moreover, the performance is adversely affected due to the presence of cross-talk, which is shown by $h_{\nu\mu}(k)$ with $\nu \neq \mu$.

4.6.1. Simulation Results

The system model, as mentioned in Figure 4.3, is utilized to perform discrete-time Monte Carlo simulation with a (2×2) MIMO system considering a 1.4 km long MMF channel. The simulations are conducted using three sequential steps, as introduced in subsection 4.5.1. The first step involves the implementation of PE-MMSE and channel estimation. In the following step, design and optimization of joint-PPE coefficients. Finally, the performance evaluation of the joint-PPE scheme and comparison between different equalization techniques is realized.

According to the literature, the pre- and post-equalizers at the transceiver outperform equalizers limited either to the transmitter or receiver. Therefore, the performance comparison between the state-of-the-art ZF-PPE and the proposed joint-PPE is crucial. Moreover, the limited increase in the transmitter's complexity is also considered to be a critical factor. In order to restrict the transmitter's complexity, the least number of pre-equalization coefficients required to achieve the lowest NWF is preferable as it improves BER performance. Consequently, the relation between the length of pre-equalizer L_{p} and NWF at each MIMO

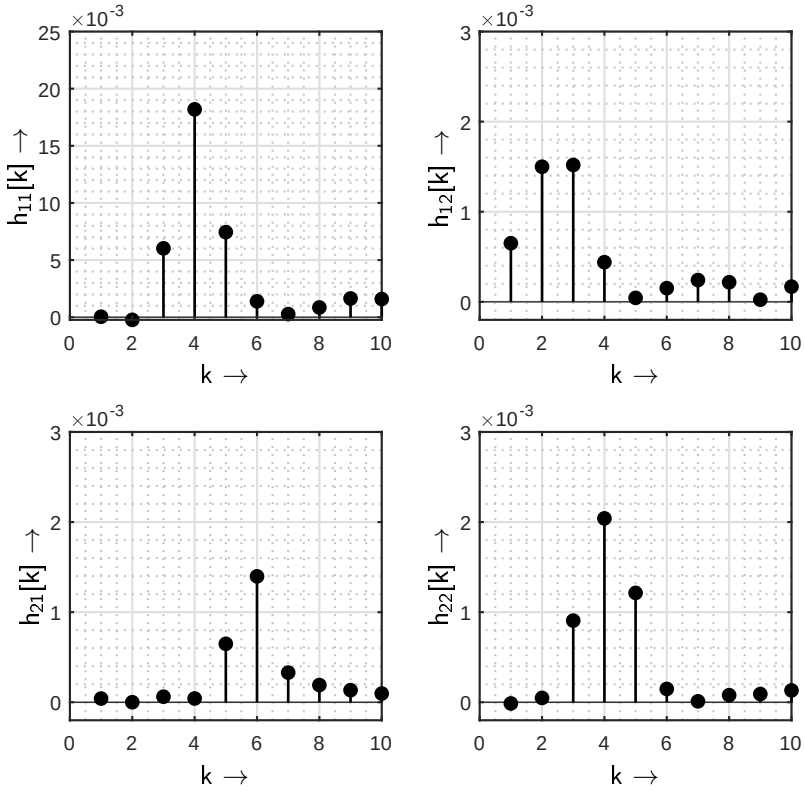

Figure 4.13.: Measured channel impulse response of a 1.4 km long MMF with respect to the symbol rate $f_{\mathrm{T}} = 1/T_{\mathrm{s}} = 5\,\mathrm{GBd}$ per MIMO layer at an operating wavelength of 1550 nm.

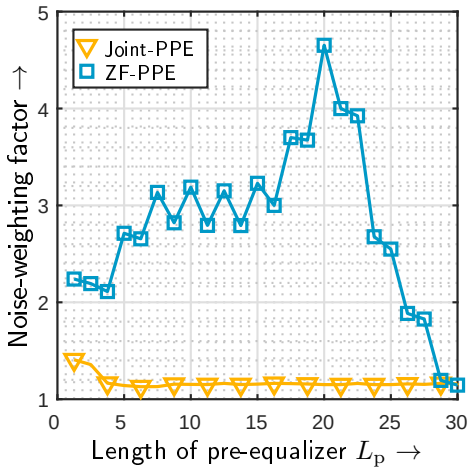

(a) First MIMO input.

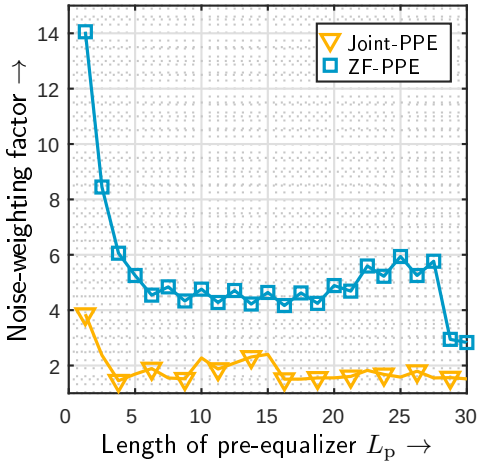

(b) Second MIMO input.

Figure 4.14.: Noise weighting factor with increasing number of pre-equalization coefficients, where an input-specific comparison between the proposed joint-PPE scheme and the ZF-based PPE is exhibited.

input is determined, which is illustrated in Figure 4.14. It is evident from the results that the pre-equalizer designed with joint-PPE achieves a lower NWF with significantly fewer pre-equalizer coefficients compared to the ZF-PPE. For instance, the joint-PPE scheme with $L_p = 4$ reaches the minimum value of NWF on both MIMO inputs. However, the ZF-PPE scheme needs $L_p = 30$ on the first MIMO input and $L_p > 30$ on the second MIMO input to reach a minimum NWF similar to the joint-PPE. Therefore, a pre-equalizer with four taps on each MIMO input is selected for further performance analysis.

The BER performances of joint-PPE, ZF-PPE, and PE-MMSE are calculated with PAM-2 and PAM-4 formats, which are shown in Figure 4.15 and Figure 4.16, respectively. The filled markers indicate that a pre-equalizer with two taps is incorporated at the transmitter. The

Table 4.3.: Overall simulated SNR gains of the (2×2) optical MIMO system at 10^{-4} BER using a 1.4 km long MMF channel at $f_T = 5$ GBd per MIMO input.

Modulation format	Equalization	L_p	L_f	SNR (in dB) at a BER of 10^{-4}	SNR gain (in dB)
PAM-2	PE-MMSE	-	30	22.39	-
	ZF-PPE	4	26	21.47	0.92
	Joint-PPE	4	26	20.03	2.36
PAM-4	PE-MMSE	-	30	58.19	-
	ZF-PPE	4	26	57.02	1.17
	Joint-PPE	4	26	55.81	2.38

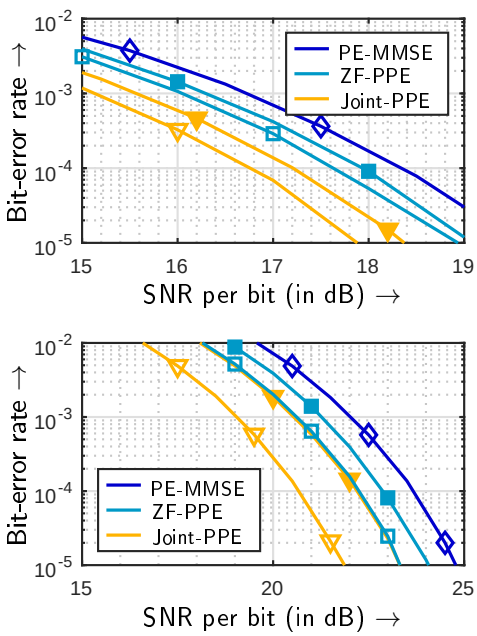

(a) MIMO first input (top) and second input (bottom).

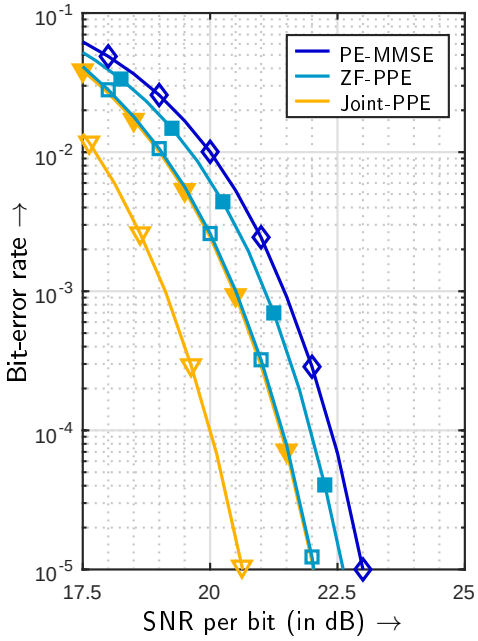

(b) System BER.

Figure 4.15.: BER dependent on SNR for the first scenario, where PAM-2 is utilized on both the MIMO inputs. The BER values associated with $L_{\mathrm{p}} = 2$ and $L_{\mathrm{p}} = 4$ are represented with the filled and the empty markers, respectively.

SNR required to reach a BER of 10^{-4} are computed and summarized in Table 4.3. From Figure 4.15, the system BER of joint-PPE with $L_{\mathrm{p}} = 4$ achieves the best results compared to ZF-PPE and PE-MMSE. An SNR gain of $\approx 2.36\,\mathrm{dB}$ to reach a BER of 10^{-4} is obtained with the joint-PPE in comparison to the ZF-PPE. Additionally, the joint-PPE yields an SNR benefit of $\approx 1.44\,\mathrm{dB}$ compared to ZF-PPE. Overall, the joint-PPE proves to be beneficial with a PAM-2 format.

The performance evaluation of the joint-PPE are validated with a PAM-4 constellation. The BER performances of joint-PPE, ZF-PPE and PE-MMSE evaluated with PAM-4 format are shown in Figure 4.16. An SNR gain of $\approx 2.38\,\mathrm{dB}$ is obtained to reach a BER of 10^{-4} with the joint-PPE scheme over the PE-MMSE. Moreover, when the PPE schemes are compared with each other, the joint-PPE leads by an SNR gain of $\approx 1.21\,\mathrm{dB}$ over the conventional ZF-PPE.

In summary, the simulation results provide an evidence that the jointly designed and optimized PPE coefficients can lead to SNR gains. Moreover, the joint-PPE scheme has proven to be beneficial with PAM-2 and PAM-4 formats. Therefore, the simulation results are subjected to be verified using an experimental setup.

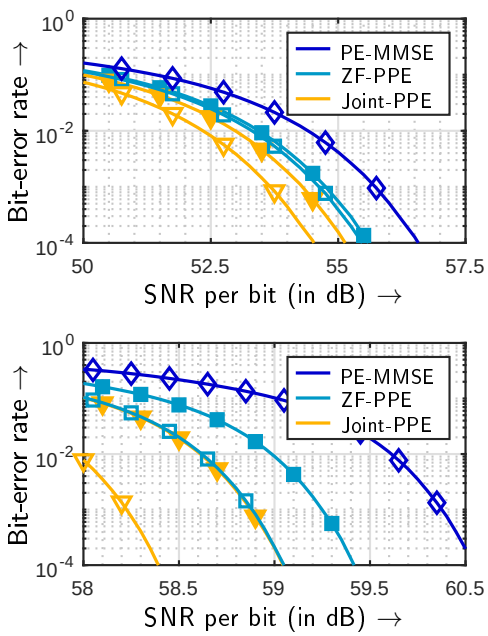

(a) MIMO first input (top) and second input (bottom).

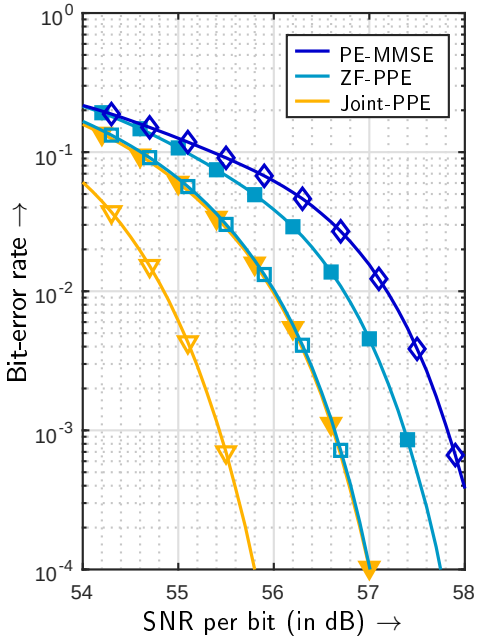

(b) System BER.

Figure 4.16.: BER dependent on SNR for the first scenario, where PAM-4 is utilized on both the MIMO inputs. The BER values associated with $L_\mathrm{p} = 2$ and $L_\mathrm{p} = 4$ are represented with the filled and the empty markers, respectively.

4.6.2. Experimental Results

The efficiency of the joint-PPE scheme is assessed using an SDM-based (2×2) MIMO system. The BER performance is evaluated with the experimental setup using a 1.4 km long MMF channel, as illustrated in Figure 4.5. The performance of equalization schemes, such as joint-

Table 4.4.: Measured average optical received power P_r gain of the (2×2) optical MIMO system at 10^{-4} BER using a 1.4 km long MMF channel at $f_\mathrm{T} = 5$ GBd per MIMO input.

Modulation format	Equalization	L_p	L_f	P_r (in dBm) at BER of 10^{-4}	P_r gain (in dB)
PAM-2	PE-MMSE	-	30	-7.58	-
	ZF-PPE	4	26	-8.42	0.84
	Joint-PPE	4	26	-10.16	2.58
PAM-4	PE-MMSE	-	30	-2.13	-
	ZF-PPE	4	26	-3.08	0.95
	Joint-PPE	4	26	-4.81	2.68

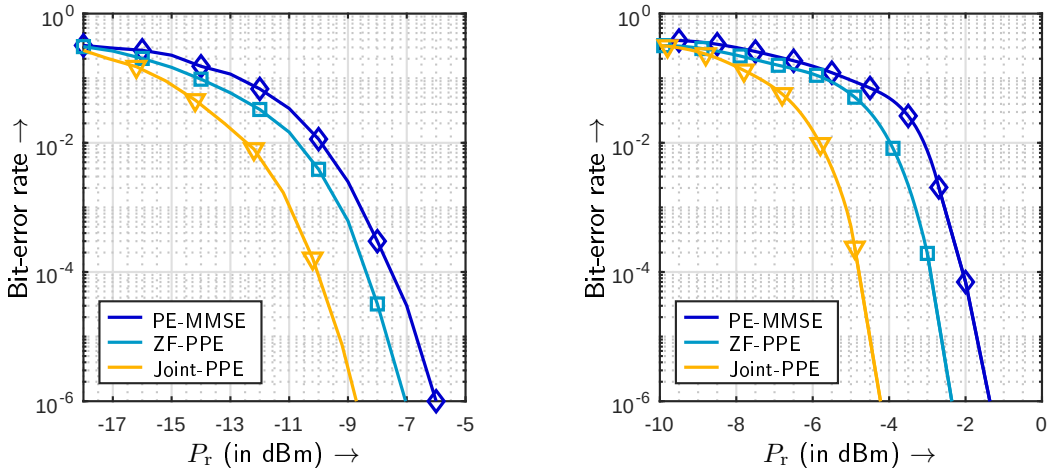

(a) PAM-2 transmission.

(b) PAM-4 transmission.

Figure 4.17.: Overall experimental BER performance comparison between the PE-MMSE, ZF-PPE and joint-PPE with PAM-2 and PAM-4 formats, where four-tap pre-equalizers are utilized in both PPE schemes.

PPE, ZF-PPE, and PE-MMSE, are analyzed using the PAM-2 and PAM-4 formats with 5 GBd per MIMO input.

The BER performances dependent upon the average received power P_r are demonstrated in Figure 4.17 and summarized in Table 4.4. From the BER performance of PAM-2 transmission, the joint-PPE scheme outperforms the ZF-PPE and the PE-MMSE over the entire range of P_r. The P_r required to reach a BER of 10^{-4} is reduced by ≈ 2.58 dB while using the joint-PPE over PE-MMSE. Moreover, the joint-PPE scheme yields better performance than the ZF-PPE. The enhancement of ≈ 1.74 dB in system performance to achieve a BER of 10^{-4} is observed with the joint-PPE scheme over the ZF-PPE. The transmission qualities with PAM-2 format using the different equalization schemes are shown in Figure 4.18. The wider eye openings with the PPE schemes in comparison to the PE-MMSE prove that the present PPE filter performs better than the equalizer limited either to the transmitter or the receiver. Considering the eye openings of the ZF-PPE and joint-PPE, the wider eye opening is exhibited by the joint-PPE, which also relates to better BER performance.

The BER performances of the joint-PPE, ZF-PPE, and PE-MMSE are computed using PAM-4 transmission, which are displayed in Figure 4.17. According to the BER comparison between the PE-MMSE and the joint-PPE schemes, the highest performance improvements of ≈ 2.68 dB are obtained. Moreover, the benefits of using joint-PPE are evident against the ZF-PPE scheme with a P_r gain of ≈ 1.73 dB to reach a BER of 10^{-4}. The eye openings using PAM-4 format with different equalization schemes are demonstrated in Figure 4.19. Clearly, the wider eye-opening using the joint-PPE is obtained in comparison to other equalization

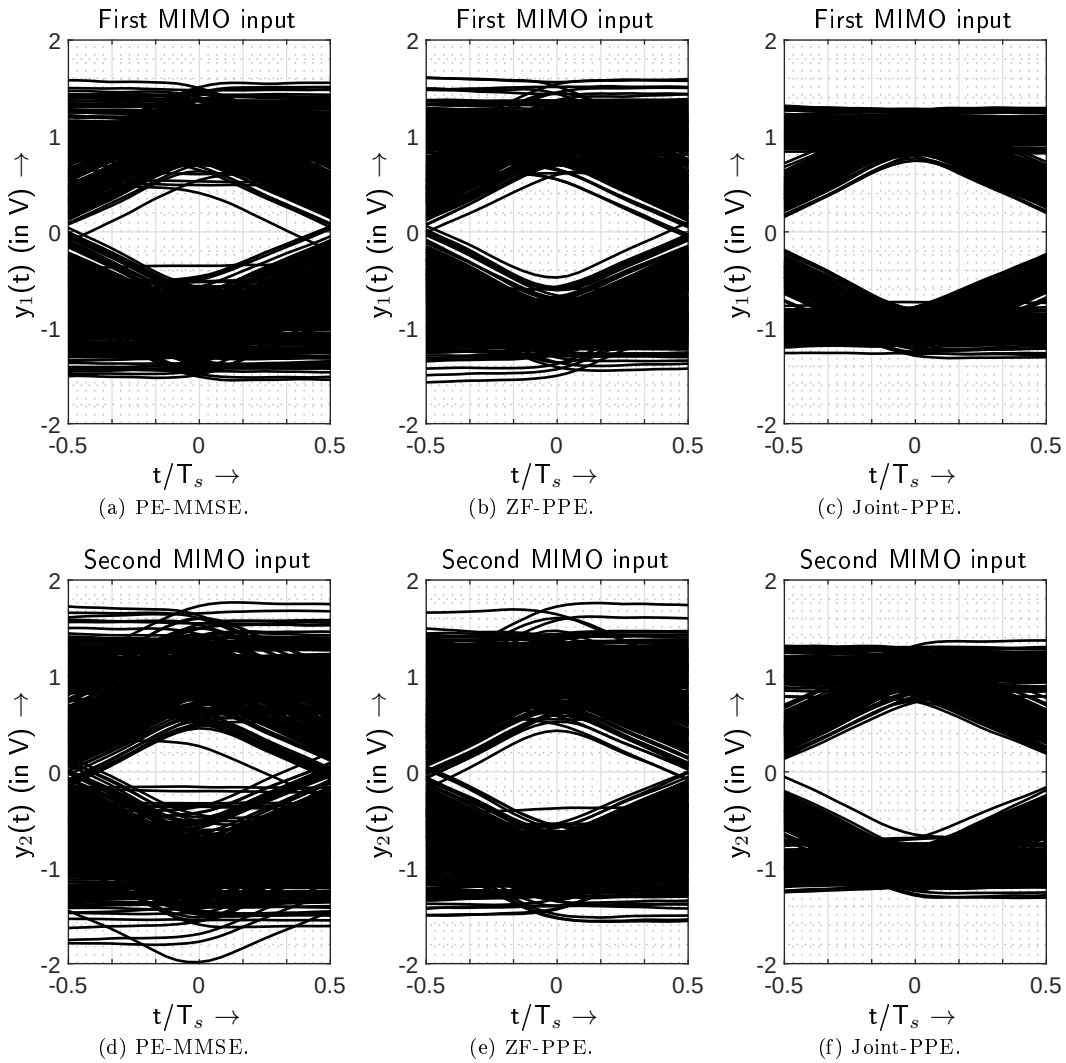

(a) PE-MMSE. (b) ZF-PPE. (c) Joint-PPE.

(d) PE-MMSE. (e) ZF-PPE. (f) Joint-PPE.

Figure 4.18.: Eye diagrams of the joint-PPE, ZF-PPE and PE-MMSE using PAM-2 transmission.

schemes. Overall, the potential of the joint-PPE is clearly verified with the experimental setup.

4.7. Summary

In this chapter, the advantages of using the joint-transceiver scheme over a (2×2) SDM-based optical MIMO system are shown. Two short reach optical MMF interconnects of the lengths 250 m and 1.4 km are utilized with this configuration. The MIMO system model is introduced using continuous and discrete time domain representations. Moreover, the power

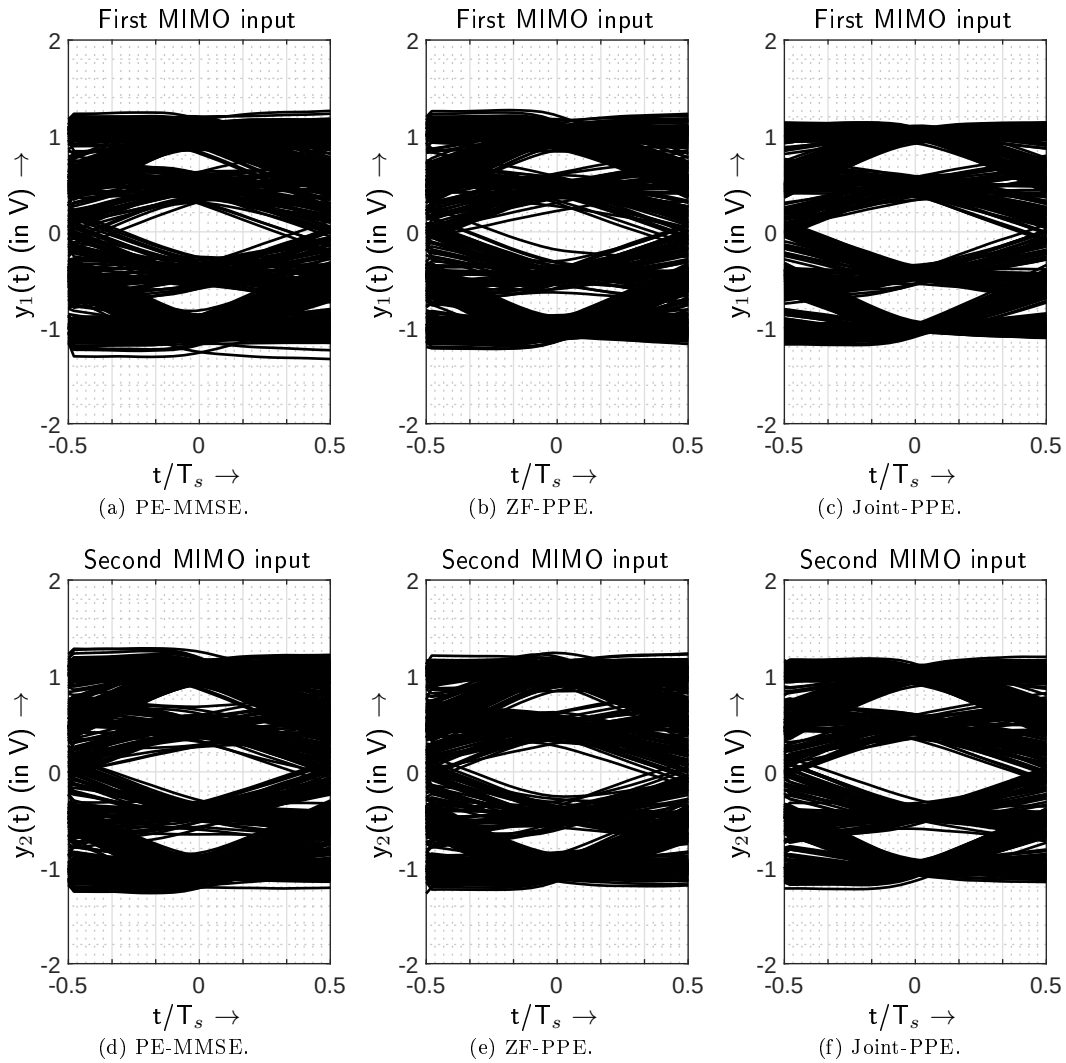

(a) PE-MMSE. (b) ZF-PPE. (c) Joint-PPE.

(d) PE-MMSE. (e) ZF-PPE. (f) Joint-PPE.

Figure 4.19.: Eye diagrams of the joint-PPE, ZF-PPE and PE-MMSE using PAM-4 transmission.

constraint is incorporated with the MIMO system model. The joint-transceiver scheme is applied on all the MIMO inputs using PAM-2 and PAM-4 formats. While considering a PAM-4 format with a 1.4 km long MMF channel, the reduction of ≈ 2.68 dB in P_{r} to reach a BER of 10^{-4} is reported with the proposed joint-PPE scheme compared to PE-MMSE. Similarly, a P_{r} gain of ≈ 2.58 dB with a PAM-2 format is achieved to reach a BER of 10^{-4}. When the performances of the ZF-PPE and joint-PPE are compared, a P_{r} gain of ≈ 1.74 dB is noted for both, PAM-2 and PAM-4, formats. The Monte Carlo simulation results also verify the benefits of using the joint-PPE schemes over ZF-PPE and PE-MMSE. Moreover, the transmission quality of the system is also enhanced, which is clearly demonstrated by

eye diagrams. Despite the presence of significant dispersion-induced impairments and modal cross-talk due to an MMF channel, the joint-PPE scheme yields BER performance benefits in an optical MIMO configuration. Hence, the hypothesis of shifting and designing a few taps at the transmitter side has proven to be beneficial in performance improvements over PE-MMSE and ZF-PPE equalization schemes.

5. Joint-Transceiver Equalizer with Advanced Signal Processing Concepts

The focus of this chapter is on analyzing the effectiveness of the joint-transceiver equalizer using a single modulator design at the transmitter for a (2×2) MIMO configuration. Additionally, this chapter targets the integration of the joint-PPE scheme with an advanced signal processing concept such as SVD. The SVD method uses factorization of the matrix into three matrices, which transforms the channel into a diagonal matrix. Thus, it has reportedly proven to be beneficial in enhancing the BER performance [Faz21; AL08; Pan11]. Moreover, power allocation over the MIMO inputs is also conducted to boost the system performance further.

This chapter is mainly divided into two sections depending upon different signal processing concepts. The first section describes a PFS at the transmitter with a corresponding system model. Thereafter, the concept of transceiver optimization and the challenges are addressed. At the end of this section, the system performance is computed with the provided system incorporating an MMF channel. The following section considers an advanced signal processing SVD concept, which is combined with the joint-transceiver technique. Consequently, the performance is evaluated while integrating the joint-PPE scheme with SVD and power allocation concepts.

The practical implementation of the PFS setup is conducted using a 100 m MMF channel. The modulation formats, such as PAM-2 and PAM-4, with two and four taps pre-equalizer are used to analyze the benefits of the joint-PPE schemes. The performance comparison with the same amount of equalization taps is conducted between the PE-MMSE and joint-PPE. Using the SVD concept, the joint-PPE technique with power allocation is tested over a 1.4 km long MMF channel. Moreover, the higher spectral efficiency is achieved using the PAM-4 format. Finally, the system performances of the different equalization schemes are evaluated and compared.

5.1. Parallel Frame Synchronization MIMO Setup

A (2×2) MIMO system with a transmitter configured in the parallel frame synchronization setup is illustrated in Figure 5.1. The channel and receiver structures are analogous to

the setup, which is shown in Figure 4.3. The channel is characterized by the time-varying behavior. Moreover, the adverse effects, such as ISI and ICI, are originating from the channel. The receiver includes complete mitigation of the interference using the post-equalization method.

5.1.1. System Model

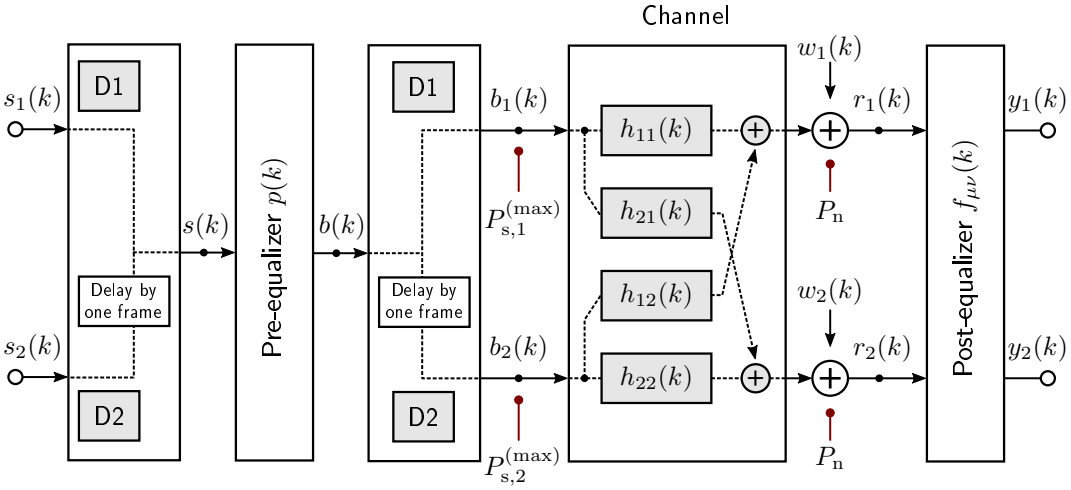

Figure 5.1.: Electrical (2×2) MIMO system model with PFS configuration.

The transmitter structure includes a serial input data stream $s(k)$, which originates from the two MIMO inputs $s_1(k)$ and $s_2(k)$. The data frames D1 and D2 are concatenated to formulate the data stream $s(k)$. The symbol amplitude at the μ-th MIMO input is given as $s_\mu(k) \in \{s_{\mu,0}, \ldots, s_{\mu,M-1}\}$ and $\mu = [1, 2, \ldots, n_{\mathrm{T}}]$. The symbols $s_\mu(k)$ are mapped onto the M_μ-ary PAM format. Afterward, the pre-equalization $p(k)$ is applied to $s(k)$ and the pre-equalized signal $b_\mu(k)$ is obtained. The data frames are again segregated using the delay by one frame on one of the MIMO inputs. Additionally, the power constraints are applied to the symbol with the highest amplitude at each MIMO input, which is mentioned in (4.10).

The multi-level pre-equalized signals propagate through the frequency-selective channel $h_{\nu\mu}(k)$. Moreover, the noise term $w_\nu(k)$ further deteriorates the transmitted signal. Afterward, the signal is received $r_\nu(k)$ with the noise power of P_{n} for the post-processing. The post-equalization is applied to the received signal for complete mitigation of the ISI and ICI. The final analytical description in the matrix notation is given as

$$\boldsymbol{y} = \boldsymbol{F} \cdot \boldsymbol{H} \cdot \boldsymbol{P} \cdot \boldsymbol{s} + \boldsymbol{F} \cdot \boldsymbol{w} \ . \tag{5.1}$$

The noise amplification due to the post-equalization is similar, as mentioned in (4.14). The quantification of the noise weighting factor is formulated in (4.15) and the BER performances are also calculated using (4.18) and (4.19). The main challenge is to design the pre-equalizer

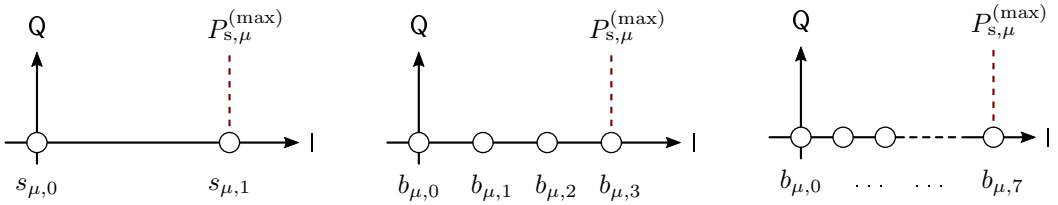

(a) Constellation of PAM-2. (b) Pre-equalizer with $L_{\mathrm{p}} = 2$. (c) Pre-equalizer with $L_{\mathrm{p}} = 3$.

Figure 5.2.: Illustrating the multi-level signals $b(k)$ after pre-equalization.

coefficients that are beneficial to compensate for the overall channel influence instead of a using pre-equalizer on each MIMO input independently.

5.1.2. Joint-Transceiver Scheme Design Principle

The joint-PPE scheme is utilized to compensate interferences originating from the channel with minimal increase in the noise amplification due to a post-equalizer. When a PFS setup is incorporated at the transmitter, a sole pre-equalizer $p(k)$ should be able to compensate the interference on both MIMO inputs simultaneously. In the MZM-based setup, an input-specific pre-equalizer $p_\mu(k)$ is available to mitigate direct and cross-talk components at the μ-th input and $\forall\ \nu$. Therefore, the optimization statement in (4.22) is modified accordingly, and it is formulated as

$$\begin{aligned} &\underset{p(k),\, f_{\mu\nu}(k)}{\text{minimize}} && \sum_{\mu=1}^{n_{\mathrm{T}}} \theta_\mu(h_{\nu\mu}(k)) && \nu = 1, \ldots, n_{\mathrm{R}} \\ &\text{subject to} && f_{\mu\nu}(k) * h_{\nu\mu}(k) * p(k) \approx z_\nu(k), && \forall \nu \\ &\text{and} && s_{\mu,M-1} = b_{\mu,N-1} = q \cdot P_{\mathrm{s},\mu}^{(\max)} \ , \end{aligned} \tag{5.2}$$

In (5.2), the optimization statement includes the minimization of the overall NWF under given constraints. The optimization problem is subjected to a complete compensation of the interference using a pre-equalizer and post-equalizer, which should result in an approximation of the Nyquist filter $z_\nu(k)$. The second constraint provides the maximum transmission optical power to the symbol with the highest amplitude. Moreover, the objective is to address the cross-talk between the channels by using the pre-equalizer. An interior-point algorithm is used for the optimization process [Wal05].
An accurate channel state information is necessary for the calculation of the PPE filters jointly. The pre-equalizer is designed using the FIR filter, which is given as

$$b[k] = \sum_{i=1}^{L_{\mathrm{p}}} p_i\,[i] \cdot s_\mu\,[k - (i-1)]\,, \qquad \text{where } \mu = 1, 2, \ldots, n_{\mathrm{T}} \ . \tag{5.3}$$

The multi-level signals after applying the pre-equalization are illustrated in Figure 5.2. The purpose of using a PFS setup is to limit the increase in the transmitter's complexity. Consequently, it results in a sole pre-equalizer to effectively compensate the channel influence. Moreover, the suggested length of a pre-equalizer is restricted to two or four taps for the latter reason. The hypothesis states that the system BER performance can be improved using the proposed joint-PPE scheme despite using the independent pre-equalizer.

5.1.3. Performance Evaluation using Monte-Carlo Simulation

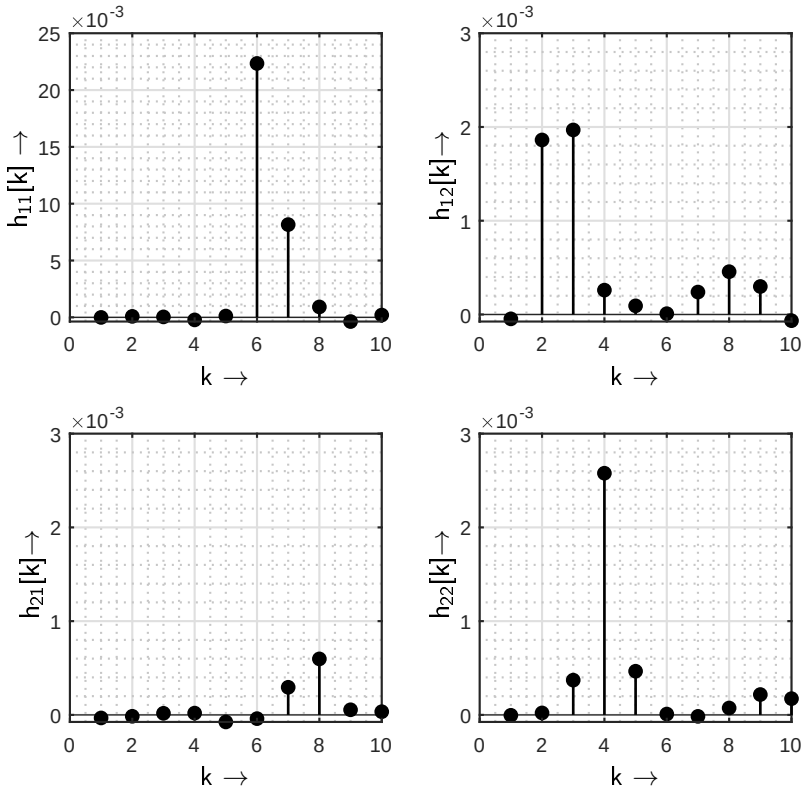

Figure 5.3.: Measured channel impulse response of a 100 m long MMF with respect to the symbol rate $f_{\mathrm{T}} = 1/T_{\mathrm{s}} = 2.5\,\mathrm{GHz}$ at an operating wavelength of 1550 nm.

The analysis of the joint-PPE scheme is conducted using the provided system model. The benefits of using a joint-PPE over a PE-MMSE equalizer are verified by using a 100 m long MMF channel. The performance is evaluated using PAM-2 and PAM-4 formats having a pre-equalizer with either two or four taps. Firstly, a Monte-Carlo simulation is performed to outline the advantages of applying the joint-PPE scheme. Afterward, an experimental setup is created to verify the effectiveness of the joint-PPE scheme.

The evaluation of the joint-PPE scheme starts by measuring the response of a 100 m long MMF channel, which is illustrated in Figure 5.3. A significant cross-talk and ISI are

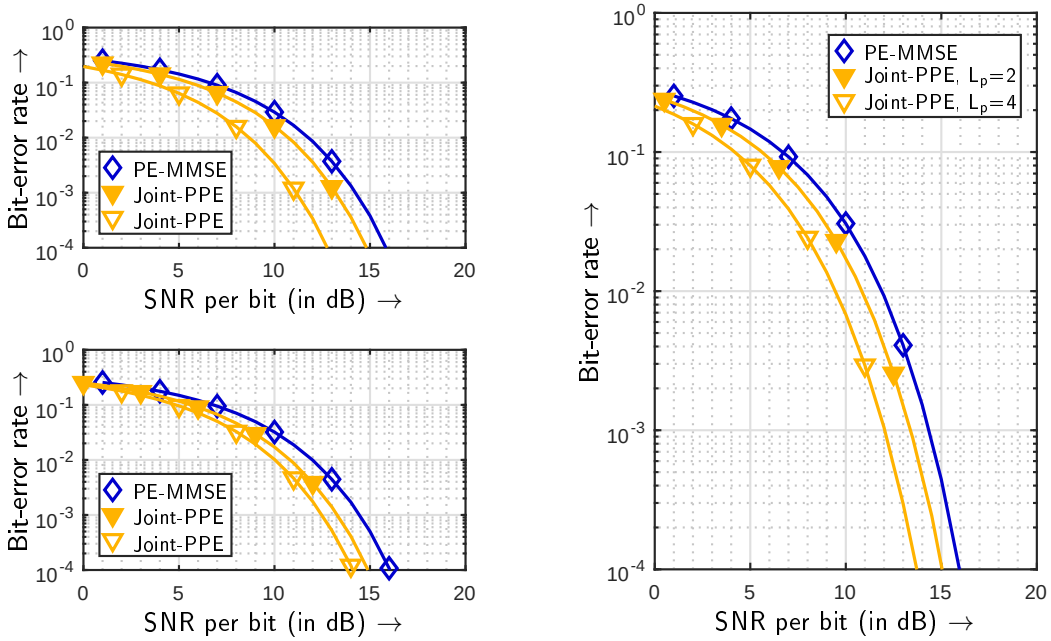

(a) MIMO input-specific BERs with the first input (top) and the second input (bottom).

(b) Overall system BER.

Figure 5.4.: BER in dependent on SNR for the first scenario, where PAM-2 is utilized on both the MIMO inputs. The BER associated with PE-MMSE and the proposed joint-PPE schemes are represented.

observed due to the presence of a single modulator for both MIMO inputs. It implies that the increase in interference is due to the deployment of the PFS configuration.

The BER performances using the joint-PPE filter and PE-MMSE with PAM-2 format are demonstrated in Figure 5.4 and Table 5.1. Additionally, the BER specific to the MIMO inputs and overall system are calculated and represented in Figure 5.4(a) and Figure 5.4(b), respectively. An SNR gain of $\approx 2.25\,\mathrm{dB}$ to reach a BER of 10^{-4} is achieved by the joint-PPE scheme using $L_\mathrm{p} = 4$ compared to the PE-MMSE. When the performance of the joint-PPE with $L_\mathrm{p} = 2$ and $L_\mathrm{p} = 4$ are compared with each other, an SNR gain of $\approx 1.35\,\mathrm{dB}$ is observed for reaching a BER of 10^{-4}. Furthermore, the joint-PPE effectively mitigates the interference, which is evident from the BER performance at the first MIMO input.

In Figure 5.5, the BER performances of the joint-PPE and PE-MMSE are illustrated with a PAM-4 format. The joint-PPE scheme yields an SNR benefit of $\approx 1.90\,\mathrm{dB}$ for reaching 10^{-4} BER in comparison to the PE-MMSE. While comparing the joint-PPE scheme with two and four taps pre-equalizer, a gain of $\approx 0.60\,\mathrm{dB}$ is realized. The minor performance increment compared to the PAM-2 implementation is due to a decrease in the extinction ratio of the PAM-4 signal. In Table 5.1, the BER performance results are described in detail. Overall, the joint-PPE is proven beneficial with a (2×2) optical MIMO setup using the PAM-4 format.

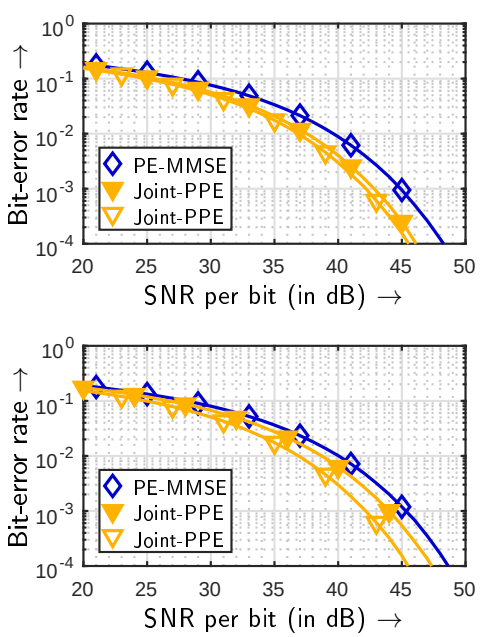

(a) MIMO input-specific BERs with the first input (top) and the second input (bottom).

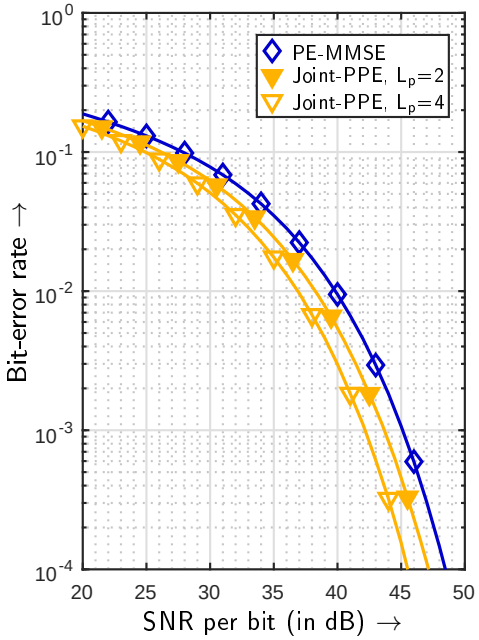

(b) Overall system BER.

Figure 5.5.: BER in dependence on SNR for the first scenario, where PAM-4 is utilized on both the MIMO inputs. The BER associated with PE-MMSE and the proposed joint-PPE schemes are represented.

In summary, the advantages of using the joint-PPE are clearly observed under all the analyzed scenarios. The results approve the hypothesis, which states that the performance benefits can be obtained by shifting of a few post-equalizer coefficients to the transmitter and appropriate designing of the PPE filter. The proposed joint-PPE is proven to be effective

Table 5.1.: Simulated SNR gain of the (2×2) optical MIMO system at 10^{-4} BER using a 100 m long MMF channel.

Modulation format	Equalization	L_p	L_f	SNR (in dB) at BER of 10^{-4}	SNR gain (in dB)
PAM-2	PE-MMSE	-	25	15.95	-
	Joint-PPE	2	23	15.05	0.90
		4	21	13.70	2.25
PAM-4	PE-MMSE	-	25	48.50	-
	Joint-PPE	2	23	47.20	1.30
		4	21	46.60	1.90

in minimal noise amplification and thereby, increasing the performance of the transmission link.

5.1.4. Experimental Performance Evaluation

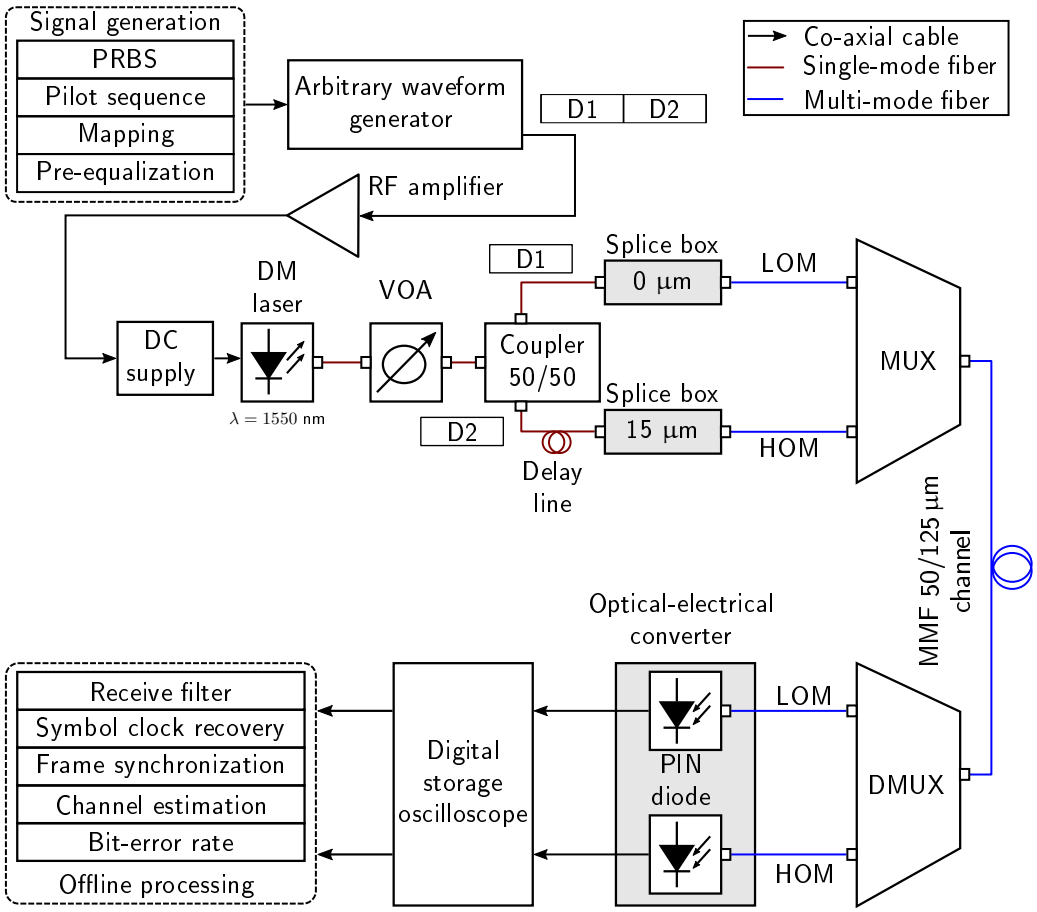

Figure 5.6.: Experimental setup for the joint-PPE scheme by using an optical (2×2) MIMO system with an MMF channel with a PFS configuration.

An experimental setup of a (2×2) optical MIMO system is developed using the PFS configuration, which is shown in Figure 5.6. The transmitter design is modified with regards to the PFS, where only one modulator (DML) is utilized. An MMF channel of 100 m is incorporated, and the receiver is identical to Figure 4.5. The signal generation starts by generating a PRBS and then pilot symbols are appended to the PRBS. Consequently, mapping and pre-equalization are applied. The electrical signal is generated using an arbitrary waveform generator, where two data frames are concatenated together, which are shown as D1 and D2. Subsequently, a radio-frequency amplifier with a gain of $\approx 20\,\mathrm{dB}$ is included for increasing the extinction ratio of the signal. The DML source operating with a maximum transmis-

Table 5.2.: Analysis of the required length of the delay lines for the PFS configuration with symbol rate of 2.5 GBd per MIMO input.

PRBS length	Delay time (in ns)	Delay length (in m)
512	204.8	41.82
1024	409.6	83.64
2048	819.2	167.27
4096	1600	334.55

sion power of ≈ 1.1 dBm and an operating wavelength of 1550 nm is utilized for modulation. Afterward, a VOA helps to realize the distinct range of average optical received power P_r for BER performance analysis. An SMF coupler and delay lines segregate the concatenated data frames by delaying one of the inputs, which is equivalent to the size of a data frame. The length of delay line L_d can be calculated as

$$L_\mathrm{d} = \frac{c \cdot L_\mathrm{m}}{n_1 \cdot f_\mathrm{T}} \ , \tag{5.4}$$

where the speed of the light is given as c, L_m is the data frame length, n_1 is the core refractive index and f_T is the symbol rate. The analysis of delay lines at 2.5 GBd per MIMO input is described in Table 5.2. The detailed description of the delay lines is provided in the Appendix A.

The SDM-based MIMO configuration is realized using the offset launching condition and the multiplexed light is launched into the MMF channel. At the receiver, the received signal is converted into an electrical signal using the PIN diodes. A DSO is used to capture the signal for further offline signal processing. Finally, the BER performances are evaluated and compared with PAM-2 and PAM-4 formats using the joint-PPE scheme and PE-MMSE.

The experimental BER performances of the joint-PPE scheme are compared with the PE-MMSE, which are demonstrated in Figure 5.7. In the joint-PPE scheme, the system per-

Table 5.3.: Measured optical received power P_r gain of the (2×2) optical MIMO system at 10^{-4} BER using a 100 m long MMF channel at $f_\mathrm{T} = 2.5$ GHz.

Modulation format	Equalization	L_p	L_f	P_r (in dBm) at BER of 10^{-4}	P_r gain (in dB)
PAM-2	PE-MMSE	-	25	-14	-
	Joint-PPE	2	23	-15.13	1.13
		4	21	-15.93	1.93
PAM-4	PE-MMSE	-	25	-9.95	-
	Joint-PPE	2	23	-10.91	0.96
		4	21	-11.79	1.84

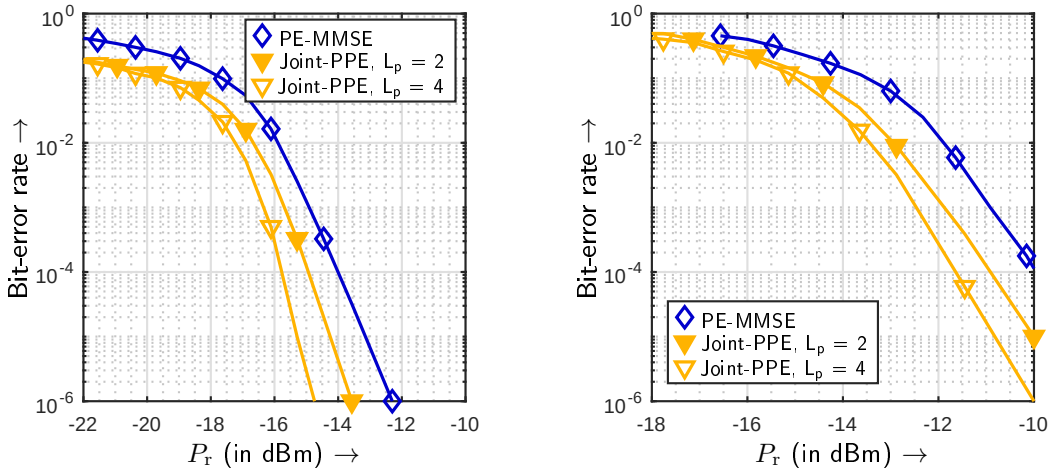

(a) PAM-2 transmission.

(b) PAM-4 transmission.

Figure 5.7.: Overall experimental BER performance comparison between the PE-MMSE and joint-PPE with PAM-2 and PAM-4 formats, where joint-PPE using $L_p = 2$ and $L_p = 4$ are represented with empty and filled downward-pointing triangle markers, respectively.

formance using the pre-equalizer with two and four taps is also included in Table 5.3. The average optical received power P_r required to reach a BER of 10^{-4} is observed with respect to the PE-MMSE. Using a PAM-2 format, the joint-PPE achieves a P_r gain of $\approx 1.93\,\text{dB}$ with a jointly designed four-taps pre-equalizer and 21-taps post-equalizer. When the joint-PPE with $L_p = 2$ is utilized, a reduction of $\approx 1.13\,\text{dB}$ in the P_r is observed for reaching 10^{-4} BER. Similarly, a P_r gain of $\approx 1.84\,\text{dB}$ is realized using the joint-PPE scheme over PE-MMSE with PAM-4. Overall, the joint-PPE outperforms the PE-MMSE while using the PFS-based optical MIMO setup. Moreover, the BER performance benefits verify the usefulness of the joint-PPE scheme with PAM-2 and PAM-4 formats.

5.2. SVD-Assisted Joint-Transceiver Equalizer Scheme

The joint-PPE scheme is proven to be beneficial with different transmission channels and transmitter's configuration. Therefore, the joint-transceiver equalizer design is integrated with the SVD technique. In MIMO signal processing, the MIMO channel undergoes SVD, which results in a number of weighted orthogonal SISO channels [SAL15; Ahr16]. The unequal weightings of the SISO channels lead to different transmission qualities at MIMO inputs, which adversely affect the overall BER performance. Thus, an optimal power allocation will aid in enhancement of the system performance [AL08; Ahr16].

The novel contribution of this section is to improve the system BER performance by using SVD-based joint-PPE over a MIMO system. Additionally, a power allocation algorithm is

introduced for an appropriate power distribution over the MIMO inputs under the constraint of fixed transmission power. The contribution of joint-PPE with SVD and power allocation strategies are evaluated over a 1.4 km MMF channel using the computer simulation. Moreover, the obtained BER from the proposed equalization scheme is compared with ZF-PPE and PE-MMSE.

5.2.1. System Model

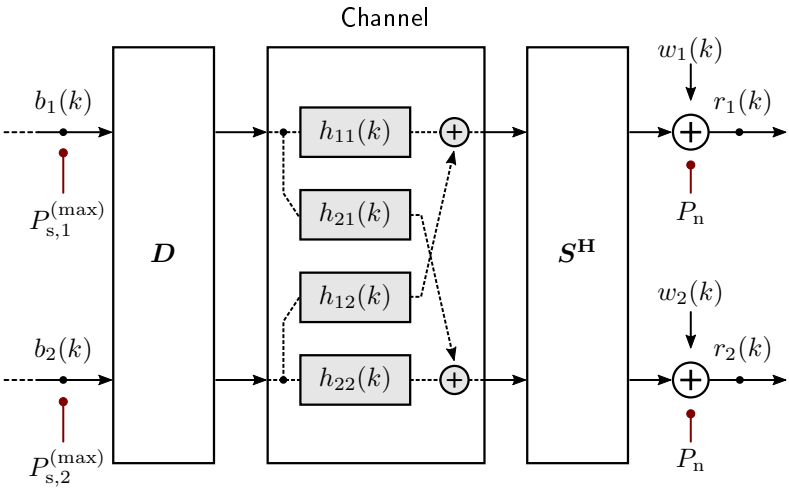

Figure 5.8.: System model of the channel using SVD.

In an SDM-based MIMO system, the design of the transmitter and receiver are identical to MZM-based MIMO system, which is shown in Figure 4.3. The SVD is applied to the MIMO channel, as shown in Figure 5.8. From (4.13), the MIMO system is represented in the matrix notation, where the received vector $\boldsymbol{r}$ and a pre-equalizer $\boldsymbol{P}$ are shown. Afterwards, the pre-equalized signal vector is multiplied with a unitary matrix $\boldsymbol{D}$, which is expressed as

$$\boldsymbol{r} = \boldsymbol{H} \cdot \boldsymbol{D} \cdot \boldsymbol{P} \cdot \boldsymbol{s} + \boldsymbol{w} \ . \tag{5.5}$$

At the receiver, a unitary matrix $\boldsymbol{S}^{\mathrm{H}}$ is multiplied by the received signal vector, and it is represented as

$$\boldsymbol{r} = \boldsymbol{S}^{\mathrm{H}} \cdot \boldsymbol{H} \cdot \boldsymbol{D} \cdot \boldsymbol{P} \cdot \boldsymbol{s} + \boldsymbol{S}^{\mathrm{H}} \cdot \boldsymbol{w} \ , \tag{5.6}$$

with $\boldsymbol{S}^{\mathrm{H}}$ denoting the Hermitian of unitary matrix $\boldsymbol{S}$ with $(n_{\mathrm{R}} \times n_{\mathrm{R}})$. The decomposition of the MIMO channel is given as

$$\boldsymbol{H} = \boldsymbol{S} \cdot \boldsymbol{V} \cdot \boldsymbol{D}^{\mathbf{H}} \ , \tag{5.7}$$

where $\boldsymbol{V}$ is the diagonal matrix having $(n_{\mathrm{R}} \times n_{\mathrm{T}})$ dimensions. By substituting (5.7) in (5.6), the resulting expression is

$$\boldsymbol{r} = \boldsymbol{V} \cdot \boldsymbol{P} \cdot \boldsymbol{s} + \tilde{\boldsymbol{w}} \ . \tag{5.8}$$

From (5.8), it is evident that the MIMO channel is decomposed into a diagonal matrix $\boldsymbol{V}$, which can be expressed as

$$\boldsymbol{V} = \begin{bmatrix} \boldsymbol{V}_{1\,1} & \cdots & \boldsymbol{0} \\ \vdots & \ddots & \vdots \\ \boldsymbol{0} & \cdots & \boldsymbol{V}_{n_{\mathrm{R}}\,n_{\mathrm{T}}} \end{bmatrix} \ . \tag{5.9}$$

In the next step, the post-equalizer signal $\boldsymbol{F}$ is applied to the received signal, and it is given as

$$\boldsymbol{y} = \boldsymbol{F} \cdot \boldsymbol{V} \cdot \boldsymbol{P} \cdot \boldsymbol{s} + \boldsymbol{F} \cdot \tilde{\boldsymbol{w}} \ . \tag{5.10}$$

The decomposed MIMO channel $\boldsymbol{V}$ can be equalized using the PPE filter. The cross-talk between the MIMO inputs is removed using SVD. The number of unequally weighted SISO channels resulting in different eye-opening on each MIMO output, and it is calculated as

$$U_{\mathrm{A},\mu} = \sqrt{\xi_\mu} \cdot U_{\mathrm{s},\mu} \ , \tag{5.11}$$

where $\sqrt{\xi_\mu}$ is the positive square roots of the eigenvalues of $\boldsymbol{H}^{\mathbf{H}}\boldsymbol{H}$ and $U_{\mathrm{s},\mu}$ denotes the half vertical eye opening at the μ-th MIMO input. The resulting system model utilizing SVD is represented in Figure 5.9. The transmission quality at the μ-th input can be defined as

$$\varrho_\mu = \frac{U_{\mathrm{A},\mu}^2}{\widetilde{P}_{\mathrm{n},\mu}} = \frac{\xi_\mu \cdot U_{\mathrm{s},\mu}^2}{\theta_\mu \cdot P_{\mathrm{n}}} \ . \tag{5.12}$$

From (5.12), the overall BER performance at the μ-th MIMO input can be calculated as

$$P_{\mathrm{BER}}^{(\mu)} = \frac{1}{\log_2(M_\mu)} \left(\frac{M_\mu - 1}{M_\mu} \right) \operatorname{erfc} \left(\sqrt{\frac{\xi_\mu \cdot U_{\mathrm{s},\mu}^2}{2 \cdot \theta_\mu \cdot P_{\mathrm{n}}}} \right) \ , \tag{5.13}$$

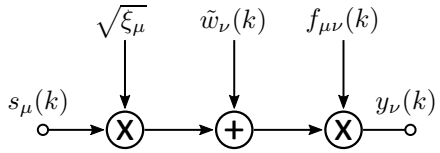

Figure 5.9.: Resulting layer-specific SVD-assisted MIMO system including the joint-PPE scheme.

5.2.2. Joint-Transceiver Equalizer Design

The SVD technique is useful in removing the ICI by transforming the MIMO channel into independent SISO channels. Furthermore, the residual interferences are mitigated using the proposed joint-transceiver equalizer. The structure of the joint-PPE scheme is similar to Figure 4.4. Consequently, the optimization statement and constraints are formulated according to the provided system model. An interior point optimization algorithm is applied to calculate the PPE coefficients collectively. The numerical optimization statement is given as

$$\begin{aligned} &\underset{p_\mu(k),\, f_{\mu\nu}(k)}{\text{minimize}} && \theta_\mu(h_{\nu\mu}(k)) && \nu = 1, \ldots, n_\mathrm{R} \\ &\text{subject to} && \boldsymbol{F} \cdot \boldsymbol{V} \cdot \boldsymbol{P} \approx \boldsymbol{I} \ , \\ &\text{and} && s_{\mu, M_\mu - 1} = q \cdot P_{\mathrm{s},\mu}^{(\max)} \ , \end{aligned} \tag{5.14}$$

where the objective is to obtain the PPE filters at a minimum value of NWF. This search for the optimal solution is conducted using the two constraints. The complete mitigation of the channel impairments $\boldsymbol{V}$ using the post-equalizer $\boldsymbol{F}$ and the pre-equalizer $\boldsymbol{P}$ are included in the first constraint. In the second constraint, the symbol $s_{\mu,M_\mu-1}$ is provided by the highest transmission power with the conversion factor q. It implies that the identical transmission power is provided to different PAM-M_μ formats.

The joint-PPE filter is computed using the optimization problem, which is dependent upon the channel state information. Therefore, it is critical to obtain an accurate channel estimation. Additionally, the obtained pre-equalizer coefficients should comply with the power budget.

5.2.3. Power Allocation

The overall BER of a MIMO system is majorly influenced by the worst-performing MIMO output. Moreover, when SVD is implemented on an MIMO system, different eye openings are obtained on each MIMO output. Therefore, it is essential to balance the BERs of each output in a decomposed MIMO system. Subsequently, the transmission quality is equalized using a scalar factor $p_\mu^{(\mathrm{PA})}$ for each MIMO input. The power allocation scheme is applied to the half vertical eye opening $U_{\mathrm{A},\mu}^{(\mathrm{PA})}$ at the μ-th MIMO input, which is defined as

$$U_{\mathrm{A},\mu}^{(\mathrm{PA})} = \sqrt{p_\mu^{(\mathrm{PA})}} \cdot \sqrt{\xi_\mu} \cdot U_{\mathrm{s},\mu} \ , \tag{5.15}$$

where $p_\mu^{(\mathrm{PA})}$ is the power allocation scaling factor and the half-level transmit amplitude is denoted by $U_{\mathrm{s},\mu}$. The transmission quality at the μ-th MIMO input is expressed as

$$\varrho_\mu^{(\mathrm{PA})} = \frac{\left(U_{\mathrm{A},\mu}^{(\mathrm{PA})}\right)^2}{\widetilde{P}_{\mathrm{n},\mu}} = \frac{p_\mu^{(\mathrm{PA})} \xi_\mu \left(U_{\mathrm{s},\mu}\right)^2}{\theta_\mu \cdot P_\mathrm{n}} \ . \tag{5.16}$$

The half-transmit amplitude of PAM-M_μ format is given as

$$U_{\mathrm{s},\mu} = \sqrt{\frac{P_{\mathrm{s},\mu}^{(\max)}}{M_\mu - 1}} \ . \tag{5.17}$$

Subsequently, the average transmit power $P_{\mathrm{s},\mu}$ is obtained by

$$P_{\mathrm{s},\mu} = \sum_{m=0}^{M_\mu - 1} \frac{m}{M_\mu} \cdot \left(U_{\mathrm{s},\mu}\right)^2 \ . \tag{5.18}$$

By substituting (5.18) into (5.16), the resulting transmission quality at the μ-th MIMO input with power allocation is described as

$$\varrho_\mu^{(\mathrm{PA})} = \frac{p_\mu^{(\mathrm{PA})} \xi_\mu}{\theta_\mu \cdot P_{\mathrm{n}}} \cdot \left(\frac{M_\mu \cdot P_{\mathrm{s},\mu}}{\sum_{m=0}^{M_\mu - 1} m} \right) \ . \tag{5.19}$$

The resulting system model with SVD and power allocation is shown in Figure 5.10. The optimal solution to minimize overall BER performance is calculated using the numerical optimization statement, which is formulated as

$$\begin{aligned} &\underset{p_\mu^{(\mathrm{PA})}}{\text{maximise}} \quad \varrho_\mu^{(\mathrm{PA})} \qquad\qquad\qquad \mu = 1, 2, \ldots, n_{\mathrm{T}} \\ &\text{subject to} \quad \sum_{\mu=1}^{n_{\mathrm{T}}} P_{\mathrm{s},\mu} - P_{\mathrm{s}} = 0 \ . \end{aligned} \tag{5.20}$$

In (5.20), the objective function aims to maximize the transmission quality with appropriate power allocation factor $p_\mu^{(\mathrm{PA})}$ for each MIMO input. The optimal solutions are searched under the power constraint. The optical power allocation coefficients will provide a better BER performance, which is investigated in the next section.

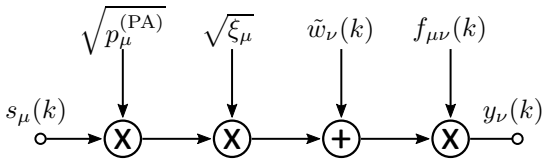

Figure 5.10.: Resulting layer-specific SVD-assisted MIMO system including the joint-PPE scheme and power allocation.

5.2.4. Performance Evaluation

In this section, the system performance of the SVD-assisted joint-PPE is evaluated. Additionally, the BER performances of PE-MMSE, ZF-PPE, and joint-PPE are calculated and compared with each other. Please note that SVD-assisted joint-PPE will be denoted as

SVD-PPE. Monte-Carlo simulations are conducted on PAM-2 and PAM-4 formats to validate the advantages of using SVD-PPE. An MMF channel of length 1.4 km with an operating wavelength of 1550 nm is utilized for the simulation, which is shown in Figure 4.13.

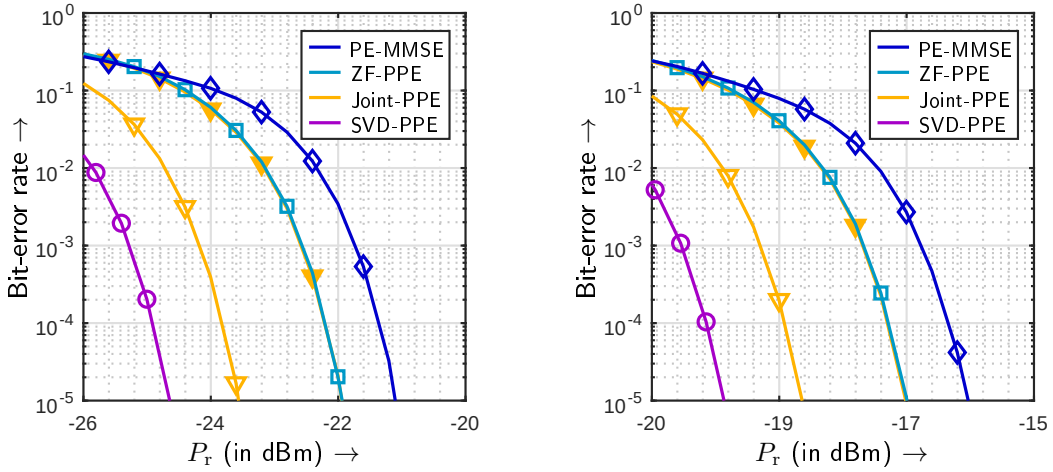

(a) PAM-2 transmission.

(b) PAM-4 transmission.

Figure 5.11.: BER dependent on simulated received power P_r for PAM-2 and PAM-4 transmissions. The BER values associated with $L_p = 2$ and $L_p = 4$ are represented with the filled and the hollow triangular markers, respectively.

The BER performances of the given system model of (2×2) MIMO system with a 1.4 km long MMF channel are illustrated in Figure 5.11. A performance overview of the different equalization schemes is depicted in Table 5.4, where the simulation received optical power P_r to reach a BER of 10^{-4}, and their P_r gains are noted. The BER results clearly indicate that the SVD-PPE outperforms the PE-MMSE, ZF-PPE, and joint-PPE schemes. While

Table 5.4.: Overall simulated P_r gains of the (2×2) optical MIMO system at 10^{-4} BER using a 1.4 km long MMF channel at $f_T = 5$ GHz.

Modulation format	Equalization scheme	L_p	L_f	P_r (in dBm) at a BER of 10^{-4}	P_r gain (in dB)
PAM-2	PE-MMSE	-	30	-21.37	-
	ZF-PPE	4	26	-22.19	0.82
	Joint-PPE	4	26	-23.91	2.54
	SVD-PPE	4	26	-24.89	3.52
PAM-4	PE-MMSE	-	30	-16.23	-
	ZF-PPE	4	26	-17.27	1.04
	Joint-PPE	4	26	-18.96	2.73
	SVD-PPE	4	26	-20.09	3.86

considering the PAM-2 format, a total P_r gain of $\approx 3.52\,\mathrm{dB}$ is achieved by SVD-PPE to reach a BER of 10^{-4} compared to PE-MMSE. It is evident from Table 5.4 that all the PPE schemes outperform the conventional PE-MMSE. A P_r gain of $\approx 0.82\,\mathrm{dB}$ is observed when ZF-PPE is utilized. The required optical received power to attain a BER of 10^{-4} is reduced to $\approx 2.54\,\mathrm{dB}$ with the joint-PPE scheme. The reduction in noise amplification by multi-level signaling ensures a three fold increase in system performance by using the joint-PPE scheme over ZF-PPE. Finally, a four times better P_r gain than ZF-PPE is achieved by SVD-PPE with the transformation of the MIMO channel into non-interfering SISO channels and jointly designing the PPE filter. The BER performance evaluation is also extended to PAM-4 format to take advantage of higher spectral efficiency. Under PAM-4 format, the SVD-PPE yields the best BER performances comparing with the PE-MMSE, ZF-PPE, and joint-PPE schemes. The maximum P_r gain of $\approx 3.86\,\mathrm{dB}$ is observed by SVD-PPE to reach a BER of 10^{-4} compared to PE-MMSE. The joint-PPE scheme without using SVD and power allocation attains a P_r gain of $\approx 2.73\,\mathrm{dB}$ for 10^{-4} BER, which is more than two times ZF-PPE.

In summary, the benefits of using the proposed joint-transceiver scheme are verified with PAM-2 and PAM-4 formats over a 1.4 km long MMF channel. Additionally, when the joint-transceiver scheme is combined with SVD and power allocation techniques, a significant boast in the BER performances has proven the effectiveness of the SVD-assisted joint-PPE scheme.

Summary

In this dissertation, a novel joint-transceiver equalizer design is proposed for enabling multi-level signaling in short reach optical MMF interconnects. A detailed analysis of the joint-PPE or the joint-transceiver equalizer is conducted using an IM/DD system. The advantages of the joint-PPE scheme in MMF interconnects are verified using different experimental setups and computer simulation scenarios.

In Chapter 2, the fundamental components utilized in an IM/DD system for short reach optical links are investigated. The functionalities of the basic structural components of an OFC system, which are transmitter, fiber channel, and receiver, are analyzed. The function of an optical transmitter is to convert a bit stream into a corresponding optical signal and, subsequently, launch this signal into a fiber channel. In this work, the external modulator MZMs and directly modulated lasers are utilized in accordance to the requirements of the provided IM/DD experimental setup. While the optical signal propagates through the channel, the optical signal is degraded by dispersion impairments, such as chromatic and modal dispersion. In a SISO configuration, the MMF-based system is adversely affected by modal dispersion, contrary to an SMF-based system. In the following section, the excitation of distinct mode groups using an offset light launching condition, and the power coupling efficiency between these mode groups are evaluated. The following section focuses on optical PIN-diode receivers, which are working on the direct-detection principle. Additionally, the major noise impairments due to an optical receiver, such as thermal and shot noise, are also discussed in this section. The dependency of these noise mechanisms on the average received optical power is studied. Consequently, the post-equalization techniques are mentioned for complete compensation of the interference originating from the channel or receiver. The emphasis of the next chapter is on utilizing the geometric constellation shaping technique to yield performance benefits. Thereby, a system model has been developed to examine the effect of the receiver's noise impairments at the different incident power levels. On the basis of the simulation results, the GCS approach has shown significant improvement in the BER performances under specific scenarios. These scenarios include using higher-order constellation sizes, such as larger than PAM-16, with high received powers in the shot noise dominant region. On the contrary, when a smaller constellation size, i.e., PAM-4, PAM-8 or PAM-16, and the received power is situated in the thermal noise dominant region, then the GCS does not yield major benefits. Additionally, the dependency of the noise variances over the received power is verified by the experimental results. It indicates that the benefits

of the GCS, as obtained in the computer simulation, can be directly transferred into practice.

The preamble of the joint-transceiver scheme for the SISO system is established in Chapter 3. Since MMF supports a higher spectral efficiency and cost-effectiveness over an SMF, an IM/DD-based system model incorporating an MMF channel is being developed with the pre- and post-equalizer. According to the literature, it has been proven that higher performance benefits are achieved with the PPE scheme over the post-equalizer only schemes. In conventional PPE schemes, the pre-and post-equalizer coefficients are computed separately. On the contrary, the joint-PPE scheme proposes to calculate and optimize the PPE filter collectively to gain higher performance benefits compared to the conventional PPE schemes. A nonlinear optimization algorithm is applied to obtain the joint-PPE coefficients, which aids the system performance by multi-level signaling. The joint-PPE coefficients follow the constraint of complete mitigation of the interference and the maximum transmission power restriction. Under the analyzed scenario, the joint-PPE has reduced the average received optical power by 7.3 % to reach a BER of 10^{-3} in comparison to the ZF-based post-equalizer only. When the performance of the MMSE-based post-equalizer only is compared with the joint-PPE scheme, a power improvement of 6.8 % is observed to reach 10^{-3} BER. In order to measure the extent of the performance benefits, the state-of-the-art ZF-based pre-equalizer with two taps and a post-equalizer with 23 taps scheme has only produced power improvement of 1.7 % and 1.2 % over PE-ZF and PE-MMSE schemes, respectively. Similarly, a two tap pre-equalizer with 23 taps post-equalizer designed using the joint-PPE scheme has improved the BER performances by power improvement of 4.7 % and 4.1 % over PE-ZF and PE-MMSE schemes, respectively. Subsequent to these simulation results, an experimental setup is constructed to verify the effectiveness of the joint-PPE scheme. The joint-PPE is able to achieve experimental improvement factors of 4.4 % over PE-ZF and 3.5 % over PE-MMSE at a BER of 10^{-3}. Due to instrumental limitation, the performance of joint-PPE with two taps pre-equalizer and 23 taps post-equalizer is validated. The BER performance benefits from simulation and experimental results are evident that the usefulness of utilizing the joint-PPE scheme can be extended from the current SISO to a MIMO configuration.

The utilization of the joint-PPE scheme is introduced to an SDM-based MIMO system to gain higher spectral efficiency. Additionally, a PAM-4 is utilized on each MIMO input to further boost the spectral efficiency. The SDM configuration is realized using the offset light launching condition into an MMF. For instance, a centric light launching with 0 µm and light with an offset of 15 µm are incorporated to achieve a (2×2) MIMO technique. Thereby, continuous and discrete-time domain MIMO system models with the pre- and post-equalizers is analyzed. The transmission power constraint is introduced with respect to the symbol with the highest amplitude for all modulation formats and on each MIMO input. An analytical description of noise amplification due to the post-equalizer and quality criteria are determined. A (2×2) MIMO experimental setup is developed to estimate the

BER performances using different equalization schemes. In order to have a minimal increase in the transmitter's complexity, a partial joint-PPE scheme is applied in which only one out of two MIMO inputs are pre-equalized. The simulation and experimental results imply that the BER performance is improved by the joint-PPE compared to post-equalizer schemes, such as PE-ZF and PE-MMSE. When the partial joint-PPE is applied to the first MIMO input, an average NWF reduction of 24.8 % is achieved. On the other hand, the average NWF reduction of 15.3 % is attained with the partial joint-PPE applied to the second MIMO input only. The simulation results signify the use of the partial joint-PPE on the first MIMO input over PE-only schemes, such as ZF and MMSE. When an experimental setup is developed, the measured BER performances validate the findings from the simulations, which indicate that the partial joint-PPE over the first MIMO input surpasses PE-ZF and PE-MMSE. The measurement campaign of the joint-PPE scheme is extended from a 250 m long MMF to a 1.4 km long MMF with a double symbol rate of 5 Gbd per MIMO input. The joint-PPE algorithm quickly converges to an optimal amount of pre-equalizer coefficients required for a better performance compared to the ZF-based PPE scheme. For instance, the joint-PPE requires only four pre-equalizer coefficients to reach a minimal NWF, whereas ZF-PPE needs 30 or more pre-equalizer coefficients for the same. The joint-PPE yields an SNR gain of ≈ 2.3 dB to reach a BER of 10^{-4} with PAM-2 and PAM-4 compared to PE-MMSE. Additionally, an SNR gain of more than two folds is achieved by the joint-transceiver scheme over conventional ZF-PPE scheme. The experimental results also verify the simulation results, and the BER performances also agree with the eye diagrams at a particular SNR.

In Chapter 5, the joint-transceiver scheme is applied to advanced signal-processing concepts. A parallel frame synchronization setup is developed to limit the transmitter's complexity. The challenge of mitigating the ISI and ICI components over both MIMO inputs using identical joint-PPE coefficients is executed. Since only one DML is incorporated, the total transmission power is reduced, and the mode coupling is prevalent in such a configuration. The simulation results indicate an SNR gain of ≈ 2 dB in BER performance to reach a BER of 10^{-4} using PAM-2 and PAM-4 formats over a 100 m long MMF channel. The experimental performance evaluation also confirms the effectiveness of the joint-PPE scheme. A combination of the joint-PPE scheme with the SVD technique is used to further boost the system performance. The ICI component of an MMF channel is compensated by transforming the MIMO into individual SISO channels using SVD. Moreover, a power allocation technique is utilized to balance the BER of different MIMO inputs. The results imply that the SVD-based joint-PPE achieves the best performance by outperforming PE-MMSE, ZF-PPE, and joint-PPE without SVD schemes. An improvement of 3.52 dB and 3.86 dB using SVD-PPE in the average optical received power is observed with PAM-2 and PAM-4, respectively. The BER results confirm the effectiveness of the joint-transceiver scheme over the MMF channel. The high spectral efficiency is achieved with an SDM-based MIMO configuration and a PAM-4 format. In conclusion, this work adds valuable insight into the optimization of the

joint-PPE with multi-level signaling while maintaining cost-effectiveness and simple implementation.

Future research could focus on the realization of an adaptive joint-PPE. Moreover, the dynamic environment of the channel should be considered for further performance improvements. Additionally, the potential of the PPE schemes can be explored in the area of quantum communication incorporating the quantum key distribution.

References

[Agr02] G. P. Agrawal. *Fiber-optic communication systems.* New York: Wiley Interscience, 2002.
ISBN: 0471221147.

[AL08] A. Ahrens and C. Lange. "Modulation-mode and power assignment in SVD-equalized MIMO systems". In: *Facta universitatis - series: Electronics and Energetics* 21.2 (2008), pp. 167–181.
DOI: 10.2298/fuee0802167a.

[Ahr16] A. Ahrens, A. Sandmann, Z. Wang, and J. G. McWhirter. "Polynomial Matrix SVD Algorithms for Broadband Optical MIMO Systems". In: *Proceedings of the 13th International Joint Conference on e-Business and Telecommunications.* SCITEPRESS - Science and Technology Publications, 2016.
DOI: 10.5220/0005949400350042.

[ABP22] M. S. Alam, E. Berikaa, and D. V. Plant. "Net 350 Gbps/λ IMDD Transmission Enabled by High Bandwidth Thin-Film Lithium Niobate MZM". In: *IEEE Photonics Technology Letters* 34.19 (Oct. 2022), pp. 1003–1006.
DOI: 10.1109/lpt.2022.3198322.

[Ant15] C. Antonelli, A. Mecozzi, M. Shtaif, and P. J. Winzer. "Modeling and performance metrics of MIMO-SDM systems with different amplification schemes in the presence of mode-dependent loss". In: *Optics Express* 23.3 (Jan. 2015), p. 2203.
DOI: 10.1364/oe.23.002203.

[App13] K. Appaiah, R. Salas, S. Vishwanath, and S. R. Bank. "Offset Coupling, Feedback, and Spatial Multiplexing in 4x4 Incoherent-MIMO Multimode Fiber Links". In: *Journal of Lightwave Technology* 31.17 (Sept. 2013), pp. 2926–2939.
DOI: 10.1109/jlt.2013.2274795.

[Bad18] S. Bade, B. Denolle, G. Trunet, N. Riguet, P. Jian, O. Pinel, and G. Labroille. "Fabrication and Characterization of a Mode-selective 45-Mode Spatial Multiplexer based on Multi-Plane Light Conversion". In: *Optical Fiber Communications Conference and Exposition (OFC).* Mar. 2018, pp. 1–3.

[Bai12] N. Bai, E. Ip, Y.-K. Huang, E. Mateo, F. Yaman, M.-J. Li, S. Bickham, S. Ten, J. Linares, C. Montero, V. Moreno, X. Prieto, V. Tse, K. M. Chung, A. P. T. Lau, H.-Y. Tam, C. Lu, Y. Luo, G.-D. Peng, G. Li, and T. Wang. "Mode-division multiplexed transmission with inline few-mode fiber amplifier". In: *Optics Express* 20.3 (Jan. 2012), p. 2668.
DOI: 10.1364/oe.20.002668.

[Bat17] H. G. Batshon, M. V. Mazurczyk, J.-X. Cai, O. V. Sinkin, M. Paskov, C. R. Davidson, D. Wang, M. Bolshtyansky, and D. Foursa. "Coded Modulation based on 56APSK with Hybrid Shaping for High Spectral Efficiency Transmission". In: *European Conference on Optical Communication (ECOC)*. IEEE, Sept. 2017.
DOI: 10.1109/ecoc.2017.8346117.

[Ben18] K. Benyahya, C. Simonneau, A. Ghazisaeidi, R. R. Muller, M. Bigot, P. Sillard, P. Jian, G. Labroille, J. Renaudier, and G. Charlet. "200Gb/s Transmission Over 20km of FMF Fiber Using Mode Group Multiplexing and Direct Detection". In: *2018 European Conference on Optical Communication (ECOC)*. IEEE, Sept. 2018.
DOI: 10.1109/ecoc.2018.8535152.

[BF82] S. Berdagué and P. Facq. "Mode division multiplexing in optical fibers". In: *Applied Optics* 21.11 (June 1982), p. 1950.
DOI: 10.1364/ao.21.001950.

[Bir15] T. A. Birks, I. Gris-Sánchez, S. Yerolatsitis, S. G. Leon-Saval, and R. R. Thomson. "The photonic lantern". In: *Advances in Optics and Photonics* 7.2 (Apr. 2015), p. 107.
DOI: 10.1364/aop.7.000107.

[Bot08] S. Bottacchi. *Noise and Signal Interference in Optical Fiber Transmission Systems: An Optimum Design Approach*. Wiley Telecom, June 2008. 854 pp.
ISBN: 0470060611.

[Cai18] J.-X. Cai, H. G. Batshon, M. V. Mazurczyk, O. V. Sinkin, D. Wang, M. Paskov, W. W. Patterson, C. R. Davidson, P. C. Corbett, G. M. Wolter, T. E. Hammon, M. A. Bolshtyansky, D. G. Foursa, and A. N. Pilipetskii. "70.46 Tb/s Over 7,600 km and 71.65 Tb/s Over 6,970 km Transmission in C+L Band Using Coded Modulation With Hybrid Constellation Shaping and Nonlinearity Compensation". In: *Journal of Lightwave Technology* 36.1 (Jan. 2018), pp. 114–121.
DOI: 10.1109/jlt.2017.2757281.

[CC01] Q. Cao and S. Chi. "Approximate analytical description for fundamental-mode fields of graded-index fibers: beyond the Gaussian approximation". In: *Journal of Lightwave Technology* 19.1 (2001), pp. 54–59.
DOI: 10.1109/50.914485.

[CES13] J. Carpenter, B. J. Eggleton, and J. Schröder. "110x110 optical mode transfer matrix inversion". In: *Optics Express* 22.1 (Dec. 2013), p. 96.
DOI: 10.1364/oe.22.000096.

[CZB21] H. Che, K. Zhu, and Y. Bai. "Multicarrier Faster-Than-Nyquist Based on Efficient Implementation and Probabilistic Shaping". In: *IEEE Access* 9 (2021), pp. 63943–63951.
DOI: 10.1109/access.2021.3075575.

[Che18] B. Chen, C. Okonkwo, H. Hafermann, and A. Alvarado. "Increasing Achievable Information Rates via Geometric Shaping". In: *European Conference on Optical Communication (ECOC)*. IEEE, Sept. 2018.
DOI: 10.1109/ecoc.2018.8535358.

[Che14] H. Chen, R. van Uden, C. Okonkwo, and T. Koonen. "Compact spatial multiplexers for mode division multiplexing". In: *Optics Express* 22.26 (Dec. 2014), p. 31582.
DOI: 10.1364/oe.22.031582.

[Cho18] J. Cho, X. Chen, S. Chandrasekhar, G. Raybon, R. Dar, L. Schmalen, E. Burrows, A. Adamiecki, S. Corteselli, Y. Pan, D. Correa, B. McKay, S. Zsigmond, P. J. Winzer, and S. Grubb. "Trans-Atlantic Field Trial Using High Spectral Efficiency Probabilistically Shaped 64-QAM and Single-Carrier Real-Time 250-Gb/s 16-QAM". In: *Journal of Lightwave Technology* 36.1 (Jan. 2018), pp. 103–113.
DOI: 10.1109/jlt.2017.2776840.

[Cis20] Cisco. *Cisco Annual Internet Report*. Tech. rep. Mar. 2020. URL: https://www.cisco.com/c/en/us/solutions/collateral/executive-perspectives/annual-internet-report/white-paper-c11-741490.pdf.

[Doc20] A. Dochhan, N. Eiselt, H. Grießer, M. Eiselt, J. J. V. Olmos, I. T. Monroy, and J.-P. Elbers. "Solutions for 400 Gbit/s Inter Data Center WDM Transmission". In: (2020).
DOI: 10.48550/ARXIV.2009.11184.

[DKX09] M. E. Durst, D. Kobat, and C. Xu. "Tunable dispersion compensation by a rotating cylindrical lens". In: *Optics Letters* 34.8 (Apr. 2009), p. 1195.
DOI: 10.1364/ol.34.001195.

[Ell16] A. D. Ellis, N. M. Suibhne, D. Saad, and D. N. Payne. "Communication networks beyond the capacity crunch". In: *Philosophical Transactions of the Royal Society A: Mathematical, Physical and Engineering Sciences* 374.2062 (Mar. 2016), p. 20150191.
DOI: 10.1098/rsta.2015.0191.

[Ess10] R.-J. Essiambre, G. Kramer, P. J. Winzer, G. J. Foschini, and B. Goebel. "Capacity Limits of Optical Fiber Networks". In: *Journal of Lightwave Technology* 28.4 (Feb. 2010), pp. 662–701.
DOI: 10.1109/jlt.2009.2039464.

[Faz21] Y. Fazea, A. Amphawan, Y. Al-Gumaei, A. M. Al-Samman, and W. M. Al-Rahmi. "Modes power equalization based-singular value decomposition in mode division multiplexing systems for multi-hungry bandwidth applications". In: *Optical Fiber Technology* 61 (Jan. 2021), p. 102389.
DOI: 10.1016/j.yofte.2020.102389.

[For84] D. G. Forney, R. Gallager, G. Lang, F. Longstaff, and S. Qureshi. "Efficient Modulation for Band-Limited Channels". In: *IEEE Journal on Selected Areas in Communications* 2.5 (Sept. 1984), pp. 632–647.
DOI: 10.1109/jsac.1984.1146101.

[Fra58] W. Franz. "Einfluß eines elektrischen Feldes auf eine optische Absorptionskante". In: *Zeitschrift für Naturforschung A* 13.6 (June 1958), pp. 484–489.
DOI: 10.1515/zna-1958-0609.

[GP60] E. N. Gilbert and H. O. Pollak. "Amplitude Distribution of Shot Noise". In: *Bell System Technical Journal* 39.2 (Mar. 1960), pp. 333–350.
DOI: 10.1002/j.1538-7305.1960.tb01603.x.

[GN89] E. Grimm and W. Nowack. *Lichtwellenleitertechnik*. Huethig Heidelberg, 1989.
ISBN: 3-7785-1708-2.

[Guo19] M. Guo, Y. Qiao, X. Tang, S. Liu, Z. Sun, H. Cui, X. Xu, and L. A. Rusch. "112-Gb/s PAM4 with Joint Pre- and Post-Equalization for Data Center Interconnects". In: *Asia Communications and Photonics Conference (ACPC) 2019*. Optica Publishing Group, 2019, T2G.2.

[HM72] H. Harashima and H. Miyakawa. "Matched-Transmission Technique for Channels With Intersymbol Interference". In: *IEEE Transactions on Communications* 20.4 (Aug. 1972), pp. 774–780.
DOI: 10.1109/tcom.1972.1091221.

[Hsu06] R. C. J. Hsu, A. Tarighat, A. Shah, A. Sayed, and B. Jalali. "Capacity enhancement in coherent optical MIMO (COMIMO) multimode fiber links". In: *IEEE Communications Letters* 10.3 (Mar. 2006), pp. 195–197.
DOI: 10.1109/lcomm.2006.1603382.

[Hua18] B. Huang, J. C. A. Zacarias, H. Liu, N. K. Fontaine, H. Chen, R. Ryf, F. Poletti, J. R. Hayes, J. Antonio-Loppez, J. Zhao, R. A. Correa, and G. Li. "Triple-clad photonic lanterns for mode scaling". In: *Optics Express* 26.10 (May 2018), p. 13390.
DOI: 10.1364/oe.26.013390.

[Huo18] J. Huo, X. Zhou, K. P. Zhong, J. Tu, J. Yuan, C. Guo, K. Long, C. Yu, A. P. T. Lau, and C. Lu. "Transmitter and receiver DSP for 112 Gbit/s PAM-4 amplifierless transmissions using 25G-class EML and APD". In: *Optics Express* 26.18 (Aug. 2018), p. 22673.
DOI: 10.1364/oe.26.022673.

[Iga18] K. Igarashi, K. J. Park, T. Tsuritani, I. Morita, and B. Y. Kim. "All-fiber-based selective mode multiplexer and demultiplexer for weakly-coupled mode-division multiplexed systems". In: *Optics Communications* 408 (Feb. 2018), pp. 58–62.
DOI: 10.1016/j.optcom.2017.08.049.

[Ina79] S. Inao, T. Sato, S. Sentsui, T. Kuroha, and Y. Nishimura. "Multicore optical fiber". In: *Optical Fiber Communication*. OSA, 1979.
DOI: 10.1364/ofc.1979.wb1.

[JC19] Z. Jia and L. A. Campos, eds. *Coherent Optics for Access Networks*. CRC Press, Oct. 2019.
ISBN: 978-0-12-816502-7.
DOI: 10.1201/9780429284106.

[Jov23] O. Jovanovic, F. D. Ros, D. Zibar, and M. P. Yankov. "Geometric Constellation Shaping for Fiber-Optic Channels via End-to-End Learning". In: *Journal of Lightwave Technology* (2023), pp. 1–11.
DOI: 10.1109/jlt.2023.3276300.

[Kam18] K.-D. Kammeyer. *Nachrichtenübertragung*. 4th ed. Springer Vieweg, 2018.
ISBN: 978-3658170042.

[Kim17] M. Kim, S. H. Bae, H. Kim, and Y. C. Chung. "Transmission of 56-Gb/s PAM-4 Signal over 20 km of SSMF Using a 1.55-μm Directly-Modulated Laser". In: *Optical Fiber Communication Conference*. OSA, 2017.
DOI: 10.1364/ofc.2017.tu2d.6.

[KSU80] K.-I. Kitayama, S. Seikai, and N. Uchida. "Impulse response prediction based on experimental mode coupling coefficient in a 10-km long graded-index fiber". In: *IEEE Journal of Quantum Electronics* 16.3 (Mar. 1980), pp. 356–362.
DOI: 10.1109/jqe.1980.1070477.

[Koo02] A. Koonen, H. Boom, van den, F. Willems, J. Bergmans, and G. Khoe. "Mode group diversity multiplexing for multi-service in-house networks using multimode Polymer Optical Fibre". English. In: *proc. Symposium IEEE/LEOS Benelux Chapter, 2002*. Ed. by T. Visser, D., D. Lenstra, and H. Schouten, F. 7th Annual Symposium of the IEEE/LEOS Benelux Chapter, December 9, 2002, Amsterdam, The Netherlands ; Conference date: 09-12-2002 Through 09-12-2002. IEEE/LEOS, 2002, pp. 183–186.
ISBN: 90-807519-1-X.

[Lab14] G. Labroille, B. Denolle, P. Jian, J.-F. Morizur, P. Genevaux, and N. Treps. "Efficient and mode selective spatial mode multiplexer based on multi-plane light conversion". In: *IEEE Photonics Conference*. IEEE, Dec. 2014.
DOI: 10.1109/ipcon.2014.6995478.

[Lab15] G. Labroille, P. Jian, L. Garcia, J.-B. Trinel, R. Kassi, L. Bigot, and J.-F. Morizur. "30 Gbit/s transmission over 1 km of conventional multi-mode fiber using mode group multiplexing with OOK modulation and direct detection". In: *2015 European Conference on Optical Communication (ECOC)*. IEEE, Sept. 2015.
DOI: 10.1109/ecoc.2015.7341786.

[LSS05] E. Lach, K. Schuh, and M. Schmidt. "Application of electroabsorption modulators for high-speed transmission systems". In: *Journal of Optical and Fiber Communications Reports* 2.2 (June 2005), pp. 140–170.
DOI: 10.1007/s10297-005-0032-6.

[Lei18] Y. Lei, K. Xu, J. Li, Z. Meng, R. Wu, Z. Wan, Y. Fan, W. Zhang, F. Yin, and Y. Dai. "Feasibility of Space Division Multiplexed Transmission of IEEE 802.11 n/ac-Compliant Wireless MIMO Signals Over OM3 Multimode Fiber". In: *Journal of Lightwave Technology* 36.11 (June 2018), pp. 2076–2082.
DOI: 10.1109/jlt.2018.2802441.

[Len16] K. Lenglé, X. Insou, P. Jian, N. Barré, B. Denolle, L. Bramerie, and G. Labroille. "4x10 Gbit/s bidirectional transmission over 2 km of conventional graded-index OM1 multimode fiber using mode group division multiplexing". In: *Optics Express* 24.25 (Dec. 2016), p. 28594.
DOI: 10.1364/oe.24.028594.

[Li17] F. Li, J. Yu, Z. Cao, J. Zhang, M. Chen, and X. Li. "Experimental Demonstration of Four-Channel WDM 560 Gbit/s 128QAM-DMT Using IM/DD for 2-km Optical Interconnect". In: *Journal of Lightwave Technology* 35.4 (Feb. 2017), pp. 941–948.
DOI: 10.1109/jlt.2016.2621052.

[Liu08] J. Liu, M. Beals, A. Pomerene, S. Bernardis, R. Sun, J. Cheng, L. C. Kimerling, and J. Michel. "Waveguide-integrated, ultralow-energy GeSi electro-absorption modulators". In: *Nature Photonics* 2.7 (May 2008), pp. 433–437.
DOI: 10.1038/nphoton.2008.99.

[Log16] N. S. Loghin, J. Zollner, B. Mouhouche, D. Ansorregui, J. Kim, and S.-I. Park. "Non-Uniform Constellations for ATSC 3.0". In: *IEEE Transactions on Broadcasting* 62.1 (Mar. 2016), pp. 197–203.
DOI: 10.1109/tbc.2016.2518620.

[LV58] K. LV. "Behavior of non-metallic crystals in strong electric fields". In: *Soviet Journal of Experimental and Theoretical Physics* 6 (1958), p. 763.

[M J14] S. K. M. Jamal Deen. *Fiber Optic Communications: Fundamentals and Applications*. WILEY, May 12, 2014. 576 pp.
ISBN: 0470518677.

[MAK21] A. Mirani, E. Agrell, and M. Karlsson. "Low-Complexity Geometric Shaping". In: *Journal of Lightwave Technology* 39.2 (Jan. 2021), pp. 363–371.
DOI: 10.1109/jlt.2020.3033031.

[Olm14] M. I. Olmedo, T. Zuo, J. B. Jensen, Q. Zhong, X. Xu, S. Popov, and I. T. Monroy. "Multiband Carrierless Amplitude Phase Modulation for High Capacity Optical Data Links". In: *Journal of Lightwave Technology* 32.4 (Feb. 2014), pp. 798–804.
DOI: 10.1109/jlt.2013.2284926.

[Ols75] R. Olshansky. "Mode Coupling Effects in Graded-Index Optical Fibers". In: *Applied Optics* 14.4 (Apr. 1975), p. 935.
DOI: 10.1364/ao.14.000935.

[OK76] R. Olshansky and D. B. Keck. "Pulse broadening in graded-index optical fibers". In: *Applied Optics* 15.2 (Feb. 1976), p. 483.
DOI: 10.1364/ao.15.000483.

[Pan11] J. Pankow, S. Aust, S. Lochmann, and A. Ahrens. "Modulation mode assignment in SVD-assisted optical MIMO multimode fiber links". In: *15th International Conference on Optical Network Design and Modeling - ONDM 2011*. 2011, pp. 1–6.

[PSV19] J. Pauwels, G. V. der Sande, and G. Verschaffelt. "Space division multiplexing in standard multi-mode optical fibers based on speckle pattern classification". In: *Scientific Reports* 9.1 (Nov. 2019).
DOI: 10.1038/s41598-019-53530-6.

[Pro08] J. Proakis. *Digital communications*. Boston: McGraw-Hill, 2008.
ISBN: 9780072957167.

[PRL21] B. J. Puttnam, G. Rademacher, and R. S. Luis. "Space-division multiplexing for optical fiber communications". In: *Optica* 8.9 (Sept. 2021), p. 1186.
DOI: 10.1364/optica.427631.

[QD18] Z. Qu and I. B. Djordjevic. "Hybrid Probabilistic-Geometric Shaping in Optical Communication Systems". In: *IEEE Photonics Conference (IPC)*. IEEE, Sept. 2018.
DOI: 10.1109/ipcon.2018.8527283.

[QDA19] Z. Qu, I. B. Djordjevic, and J. Anderson. "Two-Dimensional Constellation Shaping in Fiber-Optic Communications". In: *Applied Sciences* 9.9 (May 2019), p. 1889.
DOI: 10.3390/app9091889.

[Rad97] L. Raddatz, I. White, D. Cunningham, and M. Nowell. "Increasing the bandwidth-distance product of multimode fibre using offset launch". In: *Electronics Letters* 33.3 (1997), p. 232.
DOI: 10.1049/el:19970160.

[Rad98] L. Raddatz, I. White, D. Cunningham, and M. Nowell. "An experimental and theoretical study of the offset launch technique for the enhancement of the bandwidth of multimode fiber links". In: *Journal of Lightwave Technology* 16.3 (Mar. 1998), pp. 324–331.
DOI: 10.1109/50.661357.

[Rad21] G. Rademacher, B. J. Puttnam, R. S. Luis, T. A. Eriksson, N. K. Fontaine, M. Mazur, H. Chen, R. Ryf, D. T. Neilson, P. Sillard, F. Achten, Y. Awaji, and H. Furukawa. "Peta-bit-per-second optical communications system using a standard cladding diameter 15-mode fiber". In: *Nature Communications* 12.1 (July 2021).
DOI: 10.1038/s41467-021-24409-w.

[Raj19] S. Rajbhandari, H. Chun, G. Faulkner, H. Haas, E. Xie, J. J. D. McKendry, J. Herrnsdorf, E. Gu, M. D. Dawson, and D. O'Brien. "Neural Network-Based Joint Spatial and Temporal Equalization for MIMO-VLC System". In: *IEEE Photonics Technology Letters* 31.11 (June 2019), pp. 821–824.
DOI: 10.1109/lpt.2019.2909139.

[Ram81] O. G. Ramer. "Single-Mode Fiber-to-Channel Waveguide Coupling". In: *Journal of Optical Communications* 2.4 (Jan. 1981).
DOI: 10.1515/joc.1981.2.4.122.

[Rao20] R. Rao. "Optical communication systems serve as the backbone of today's technologies". In: *MRS Bulletin* 45.12 (Dec. 2020), pp. 1056–1057.
DOI: 10.1557/mrs.2020.319.

[RFN13] D. J. Richardson, J. M. Fini, and L. E. Nelson. "Space-division multiplexing in optical fibres". In: *Nature Photonics* 7.5 (Apr. 2013), pp. 354–362.
DOI: 10.1038/nphoton.2013.94.

[RMY91] W. H. Richardson, S. Machida, and Y. Yamamoto. "Squeezed photon-number noise and sub-Poissonian electrical partition noise in a semiconductor laser". In: 66.22 (June 1991), pp. 2867–2870.
DOI: 10.1103/physrevlett.66.2867.

[Ryf18] R. Ryf, N. K. Fontaine, S. Wittek, K. Choutagunta, M. Mazur, H. Chen, J. C. Alvarado-Zacarias, R. Amezcua-Correa, M. Capuzzo, R. Kopf, A. Tate, H. Safar, C. Bolle, D. T. Neilson, E. Burrows, K. Kim, M. Bigot-Astruc, F. Achten, P. Sillard, A. Amezcua-Correa, J. M. Kahn, J. Schroder, and J. Carpenter. "High-Spectral-Efficiency Mode-Multiplexed Transmission Over Graded-Index

Multimode Fiber". In: *European Conference on Optical Communication (ECOC)*. IEEE, Sept. 2018.
DOI: 10.1109/ecoc.2018.8535536.

[Sai17] X. Sai, Y. Li, X. Zeng, L. Feng, W. Li, J. Qiu, X. Hong, Y. Zuo, H. Guo, and J. Wu. "Elliptical-core Mode-selective Photonic Lanterns for MIMO-free Mode Division Multiplexing Systems". In: *Conference on Lasers and Electro-Optics*. OSA, 2017.
DOI: 10.1364/cleo_at.2017.jw2a.68.

[ST91] B. E. A. Saleh and M. C. Teich. *Fundamentals of Photonics*. John Wiley & Sons, Inc., Aug. 1991.
DOI: 10.1002/0471213748.

[San21] A. Sandmann. "Optical Space Division Multiplexing in Short Reach Multi-Mode Fiber Systems". en. PhD thesis. Christian-Albrechts-Universitaet zu Kiel, 2021.
URL: https://macau.uni-kiel.de/receive/macau_mods_00002508.

[SAL14] A. Sandmann, A. Ahrens, and S. Lochmann. "Experimental Description of Multimode MIMO Channels utilizing Optical Couplers". In: *Photonic Networks; 15. ITG Symposium*. VDE, May 2014, pp. 1–6.

[SAL15] A. Sandmann, A. Ahrens, and S. Lochmann. "Resource Allocation in SVD-Assisted Optical MIMO Systems using Polynomial Matrix Factorization". In: *Photonic Networks; 16. ITG Symposium*. 2015, pp. 1–7.

[San17] A. Sandmann, A. Ahrens, S. Lochmann, W. Rosenkranz, and H. Zimmermann. "Experimental Multi-Mode MIMO System Evaluation using Segmented Photo Detection". In: *Photonic Networks; 18. ITG-Symposium*. May 2017, pp. 1–4.

[SSR08] S. Schollmann, N. Schrammar, and W. Rosenkranz. "Experimental Realisation of 3 x 3 MIMO System with Mode Group Diversity Multiplexing Limited by Modal Noise". In: *OFC/NFOEC 2008 - 2008 Conference on Optical Fiber Communication/National Fiber Optic Engineers Conference*. IEEE, Feb. 2008.
DOI: 10.1109/ofc.2008.4528224.

[SXR06] S. Schollmann, C. Xia, and W. Rosenkranz. "Experimental investigations of mode group diversity multiplexing on multimode fibre". In: *Optical Fiber Communication Conference and the National Fiber Optic Engineers Conference*. IEEE, 2006.
DOI: 10.1109/ofc.2006.215635.

[Sch18] W. H. Schottky. "Über spontane Stromschwankungen in verschiedenen Elektrizitätsleitern". In: 362.23 (1918), pp. 541–567.
DOI: 10.1002/andp.19183622304.

[SFP13] M. Secondini, E. Forestieri, and G. Prati. "Achievable Information Rate in Nonlinear WDM Fiber-Optic Systems With Arbitrary Modulation Formats and Dispersion Maps". In: *Journal of Lightwave Technology* 31.23 (Dec. 2013), pp. 3839–3852.
DOI: 10.1109/jlt.2013.2288677.

[SY04] S. Serbetli and A. Yener. "Transceiver Optimization for Multiuser MIMO Systems". In: *IEEE Transactions on Signal Processing* 52.1 (Jan. 2004), pp. 214–226.
DOI: 10.1109/tsp.2003.819988.

[SK09] M. B. Shemirani and J. Kahn. "Higher-Order Modal Dispersion in Graded-Index Multimode Fiber". In: *Journal of Lightwave Technology* 27.23 (Dec. 2009), pp. 5461–5468.
DOI: 10.1109/jlt.2009.2030146.

[Sil16] P. Sillard, D. Molin, M. Bigot-Astruc, K. D. Jongh, F. Achten, A. M. Velazquez-Benitez, R. Amezcua-Correa, and C. M. Okonkwo. "Low-Differential-Mode Group Delay 9-LP-Mode Fiber". In: *Journal of Lightwave Technology* 34.2 (Jan. 2016), pp. 425–430.
DOI: 10.1109/jlt.2015.2463715.

[Sil10] M. Silva-Lopez, W. Gaberl, W. Rosenkranz, and H. Zimmermann. "Segmented Photo-Detection for a MIMO Multi-Mode Fiber Transmission System". In: *Journal of Optical Communications* 31.1 (Jan. 2010).
DOI: 10.1515/joc.2010.31.1.10.

[Sim20] E. Simpanen. *Longer Wavelength GaAs-based VCSELs for Extended Reach Optical Interconnects*. Göteborg: Chalmers University of Technology, 2020.
ISBN: 9789179052423.

[SSB08] A. C. Singer, N. R. Shanbhag, and H.-m. Bae. "Electronic dispersion compensation". In: *IEEE Signal Processing Magazine* 25.6 (Nov. 2008), pp. 110–130.
DOI: 10.1109/msp.2008.929230.

[SA23] J. Singh and A. Ahrens. "Joint-Transceiver Equalization Technique over a 1.4 km Multi-Mode Fiber Using Optical MIMO Technique in IM/DD Systems". In: *Photonics* 10.6 (June 2023), p. 696.
DOI: 10.3390/photonics10060696.

[SAL22] J. Singh, A. Ahrens, and S. Lochmann. "Joint Pre- and Post-Equalization with Higher-Order Modulation Formats in SDM-Based Optical MIMO Systems". In: *Photonics* 9.11 (Nov. 2022), p. 876.
DOI: 10.3390/photonics9110876.

[Sin21] J. Singh, A. Ahrens, S. Lochmann, and C. B. Peces. "Joint Pre- and Post-Equalization in Optical MIMO with Multimode Fiber Link". In: *IEEE Microwave Theory and Techniques in Wireless Communications (MTTW)*. IEEE, Oct. 2021.
DOI: 10.1109/mttw53539.2021.9607117.

[Sin23] J. Singh, A. Ahrens, S. Lochmann, and C. B. Peces. "SVD-Assisted Joint Pre- and Post-Equalization in Optical MIMO System". In: *2023 International Interdisciplinary PhD Workshop (IIPhDW)*. IEEE, May 2023.
DOI: 10.1109/iiphdw54739.2023.10124406.

[Sin22a] J. Singh, M. Gotten, A. Ahrens, and S. Lochmann. "Joint Pre- and Post Equalization in Optical MIMO Systems using Multi-Level Signaling". In: *IEEE 95th Vehicular Technology Conference: (VTC2022-Spring)*. IEEE, June 2022.
DOI: 10.1109/vtc2022-spring54318.2022.9860726.

[Sin22b] J. Singh, A. Sandmann, A. Ahrens, and S. Lochmann. "Joint pre- and post-equalization using optical multi-level signaling". In: *The Journal of Engineering* 2022.4 (Jan. 2022), pp. 442–446.
DOI: 10.1049/tje2.12123.

[SAH19] M. Stark, F. A. Aoudia, and J. Hoydis. "Joint Learning of Geometric and Probabilistic Constellation Shaping". In: *IEEE Globecom Workshops*. IEEE, Dec. 2019.
DOI: 10.1109/gcwkshps45667.2019.9024567.

[Ste04] L. V. Stephen Boyd. *Convex Optimization*. Cambridge University Press, Mar. 25, 2004. 732 pp.
ISBN: 0521833787.

[Ste14] G. Stepniak. "Dispersion-supported direct-detection mode group division multiplexing using commercial multimode fiber couplers". In: *Optics Letters* 39.7 (Mar. 2014), p. 1815.
DOI: 10.1364/ol.39.001815.

[Stu00] H. R. Stuart. "Dispersive multiplexing in multimode fiber". In: *Optical Fiber Communication Conference. Technical Digest Postconference Edition. Trends in Optics and Photonics Vol.37 (IEEE Cat. No. 00CH37079)*. Opt. Soc. America, Mar. 2000.
DOI: 10.1109/ofc.2000.868597.

[SBK17] C. Sun, S. H. Bae, and H. Kim. "Transmission of 28-Gb/s Duobinary and PAM-4 Signals Using DML for Optical Access Network". In: *IEEE Photonics Technology Letters* 29.1 (Jan. 2017), pp. 130–133.
DOI: 10.1109/lpt.2016.2629623.

[Szc13] K. Szczerba. *Multilevel modulation in short-range optical links*. Göteborg: Chalmers University of Technology, 2013.
ISBN: 9789173859004.

[Szc12] K. Szczerba, P. Westbergh, J. Karout, J. S. Gustavsson, Å. Haglund, M. Karlsson, P. A. Andrekson, E. Agrell, and A. Larsson. "4-PAM for High-Speed Short-Range Optical Communications". In: *Journal of Optical Communications and Networking* 4.11 (Oct. 2012), p. 885.
DOI: 10.1364/jocn.4.000885.

[Tan20] X. Tang, Y. Qiao, Y.-W. Chen, Y. Lu, and G.-K. Chang. "Digital Pre- and Post-Equalization for C-Band 112-Gb/s PAM4 Short-Reach Transport Systems". In: *Journal of Lightwave Technology* 38.17 (Sept. 2020), pp. 4683–4690.
DOI: 10.1109/jlt.2020.2993997.

[Tka10] R. W. Tkach. "Scaling optical communications for the next decade and beyond". In: *Bell Labs Technical Journal* 14.4 (Feb. 2010), pp. 3–9.
DOI: 10.1002/bltj.20400.

[Ung84] H.-G. Unger. *Optische Nachrichtentechnik*. Huethig Heidelberg, 1984.

[Uni22] I. T. Union. *Measuring digital development -Facts and Figures*. International Telecommunication Union, 2022.
ISBN: 9789261370115.

[UWM15] V. J. Urick, K. Williams, and J. McKinney. *Fundamentals of Microwave Photonics*. Wiley Series in Microwave and Optical Engineering. Wiley, 2015.
ISBN: 9781119029786. URL: https://books.google.de/books?id=mg91BgAAQBAJ.

[Vel18] A. M. Velazquez-Benitez, J. E. Antonio-Lopez, J. C. Alvarado-Zacarias, N. K. Fontaine, R. Ryf, H. Chen, J. Hernandez-Cordero, P. Sillard, C. Okonkwo, S. G. Leon-Saval, and R. Amezcua-Correa. "Scaling photonic lanterns for space-division multiplexing". In: *Scientific Reports* 8.1 (June 2018).
DOI: 10.1038/s41598-018-27072-2.

[Wal05] R. A. Waltz, J. Morales, J. Nocedal, and D. Orban. "An interior algorithm for nonlinear optimization that combines line search and trust region steps". In: *Mathematical Programming* 107.3 (Nov. 2005), pp. 391–408.
DOI: 10.1007/s10107-004-0560-5.

[WHL21] F. Wang, G. Hu, and Z. Li. "A novel four dimensional constellation shaping with non-uniform signaling for long-haul fiber-optic communication". In: *Optics Communications* 486 (May 2021), p. 126755.
DOI: 10.1016/j.optcom.2021.126755.

[Wei19] J. Wei, N. Stojanovic, L. Zhang, S. Calabrò, T. Rahman, C. Xie, and G. Charlet. "Experimental comparison of modulation formats for 200 G/λ IMDD data centre networks". In: *45th European Conference on Optical Communication (ECOC 2019)*. Institution of Engineering and Technology, 2019.
DOI: 10.1049/cp.2019.0868.

[Wil15] J. Wilde, C. Schulze, R. Brüning, M. Duparré, and S. Schröter. "Selective higher order fiber mode excitation using a monolithic setup of a phase plate at a fiber facet". In: *SPIE Proceedings*. Ed. by A. V. Kudryashov, A. H. Paxton, V. S. Ilchenko, L. Aschke, and K. Washio. SPIE, Mar. 2015.
DOI: 10.1117/12.2078933.

[Wil20] A. Willner. "Dedication". In: *Optical Fiber Telecommunications VII*. Elsevier, 2020.
ISBN: 9780128165027.
DOI: 10.1016/b978-0-12-816502-7.00031-2.

[Win09] P. J. Winzer. "Modulation and Multiplexing in Optical Communications". In: *Conference on Lasers and Electro-Optics/International Quantum Electronics Conference*. OSA, 2009.
DOI: 10.1364/cleo.2009.ctul3.

[WF11] P. J. Winzer and G. J. Foschini. "MIMO capacities and outage probabilities in spatially multiplexed optical transport systems". In: *Optics Express* 19.17 (Aug. 2011), p. 16680.
DOI: 10.1364/oe.19.016680.

[WNC18] P. J. Winzer, D. T. Neilson, and A. R. Chraplyvy. "Fiber-optic transmission and networking: the previous 20 and the next 20 years". In: *Optics Express* 26.18 (Aug. 2018), p. 24190.
DOI: 10.1364/oe.26.024190.

[Wol11] S. Wolf. "An Introduction to Duality in Convex Optimization". en. In: (2011).
DOI: 10.2313/NET-2011-07-2_20.

[XR05] C. Xia and W. Rosenkranz. "Statistical analysis of electrical equalization of differential mode delay in MMF links for 10-Gigabit Ethernet". In: *OFC/NFOEC Technical Digest. Optical Fiber Communication Conference, 2005.* IEEE, Sept. 2005.
DOI: 10.1109/ofc.2005.193165.

[Yan22] M. P. Yankov, O. Jovanovic, D. Zibar, and F. Da Ros. "Recent advances in constellation optimization for fiber-optic channels". In: *2022 European Conference on Optical Communication (ECOC)*. 2022, pp. 1–4.

[YT10] B. Yuksekkaya and C. Toker. "Joint transceiver design for multiuser MIMO channel equalization". In: *IEEE 18th Signal Processing and Communications Applications Conference*. IEEE, Apr. 2010.
DOI: 10.1109/siu.2010.5650423.

[Zha21] Z. Zhai, H. Jiang, M. Fu, L. Liu, L. Yi, W. Hu, and Q. Zhuge. "An Interpretable Mapping From a Communication System to a Neural Network for Optimal Transceiver-Joint Equalization". In: *Journal of Lightwave Technology* 39.17 (Sept. 2021), pp. 5449–5458.

[ZYC17] J. Zhang, J. Yu, and H.-C. Chien. "EML-based IM/DD 400G (4 x 112.5-Gbit/s) PAM-4 over 80 km SSMF based on linear pre-equalization and nonlinear LUT pre-distortion for inter-DCI applications". In: *Optical Fiber Communications Conference and Exhibition (OFC)*. IEEE, Mar. 2017, pp. 1–3.

[Zha18a] L. Zhang, J. Wei, N. Stojanovic, C. Prodaniuc, and C. Xie. "Beyond 200-Gb/s DMT Transmission Over 2-km SMF Based on A Low-Cost Architecture with Single-Wavelength, Single-DAC/ADC and Single-PD". In: *European Conference on Optical Communication (ECOC)*. IEEE, Sept. 2018.
DOI: 10.1109/ecoc.2018.8535319.

[Zha18b] S. Zhang, Z. Qu, F. Yaman, E. Mateo, T. Inoue, K. Nakamura, Y. Inada, and I. B. Djordjevic. "Flex-Rate Transmission using Hybrid Probabilistic and Geometric Shaped 32QAM". In: *Optical Fiber Communication Conference*. OSA, 2018.
DOI: 10.1364/ofc.2018.m1g.3.

[Zhu21] Z. Zhu, J. Chen, M. Zhao, F. Pang, Q. Zhang, and N. Ye. "IM/DD mode division multiplexing transmission enabled by machine learning-based linear and nonlinear MIMO equalization". In: *Optics Communications* 488 (June 2021), p. 126832.
DOI: 10.1016/j.optcom.2021.126832.

[Zou19] D. Zou, Y. Chen, F. Li, Z. Li, Y. Sun, L. Ding, J. Li, X. Yi, L. Li, and Z. Li. "Comparison of Bit-Loading DMT and Pre-Equalized DFT-Spread DMT for 2-km Optical Interconnect System". In: *Journal of Lightwave Technology* 37.10 (May 2019), pp. 2194–2200.
DOI: 10.1109/jlt.2019.2899737.

[Zou20a] D. Zou, F. Li, W. Wang, Z. Li, and Z. Li. "Amplifier-less transmission of beyond 100-Gbit/s/λ signal for 40-km DCI-Edge with 10G-class O-band DML". In: *Journal of Lightwave Technology* 38.20 (Oct. 2020), pp. 5649–5655.
DOI: 10.1109/jlt.2020.3004007.

[Zou20b] D. Zou, Z. Zhang, F. Li, Q. Sui, J. Li, X. Yi, and Z. Li. "Single λ 500-Gbit/s PAM Signal Transmission for Data Center Interconnect Utilizing Mode Division Multiplexing". In: *Optical Fiber Communication Conference (OFC) 2020*. Optica Publishing Group, 2020.
DOI: 10.1364/ofc.2020.w1d.6.

Appendix

A. Parallel Frame Delay Synchronization

In parallel-frame synchronization experimental setup, the delay lines are utilized. In order to calculate the length of the delay fiber line L_{d}, the delay time t_{d} should be estimated as

$$t_{\mathrm{d}} = \frac{L_{\mathrm{d}}}{f_{\mathrm{T}}} \ , \tag{A.1}$$

Table A.1.: Analysis of delay lines up to 200 m.

PRBS length L_{d}	Symbol rate (in GHz)	Delay time (in ns)	Delay length (in m)
512	5.0	102.4	20.91
512	4.0	128.0	26.14
512	2.5	204.8	41.82
512	2.0	256.0	52.27
512	1.25	409.6	83.64
512	1.0	512.0	104.55
1024	5.0	204.8	41.82
1024	4.0	256.0	52.27
1024	2.5	409.6	83.64
1024	2.0	512.0	104.55
1024	1.25	819.2	167.27
2048	5.0	409.6	83.64
2048	4.0	512.0	104.55
2048	2.5	819.2	167.27
4096	5.0	819.2	167.27

where f_T represents the symbol rate. Subsequently, L_d is expressed as

$$L_\mathrm{d} = \frac{c \cdot t_\mathrm{d}}{n_1} = \frac{c \cdot L_\mathrm{m}}{n_1 \cdot f_\mathrm{T}} \ , \tag{A.2}$$

with c denoting the speed of light and core refractive index is n_1. The delay lines below 200 m are given in Table A.1. Moreover, the delay lines over 200 m are shown in Table A.2.

Table A.2.: Delay lines over a length of 200 m.

PRBS length L_d	Symbol rate (in GHz)	Delay time (in ms)	Delay length (in m)
1024	1.0	1.0	209.09
2048	2.0	1.0	209.09
2048	1.25	1.6	334.55
2048	1.0	2.0	418.18
4096	4.0	1.0	209.09
4096	2.5	1.6	334.55
4096	2.0	2.0	418.18
4096	1.25	3.3	669.09
4096	1.0	4.1	836.36
8192	5.0	1.6	334.55
8192	4.0	2.0	418.18
8192	2.5	3.3	669.09
8192	2.0	4.1	836.36
8192	1.25	6.6	1338.18
8192	1.0	8.2	1672.73
16384	5.0	3.3	669.09
16384	4.0	4.1	836.36
16384	2.5	6.6	1338.18
16384	2.0	8.2	1672.73
16384	1.25	13.1	2676.37
16384	1.0	16.4	3345.46
32768	5.0	6.6	1338.18
32768	4.0	8.2	1672.73
32768	2.5	13.1	2676.37
32768	2.0	16.4	3345.46
32768	1.25	26.2	5352.73
32768	1.0	32.8	6690.91

Name: Jasmeet Singh
Title of Dissertation: Joint-Transceiver Design for Short Reach Multi-Mode Fiber Systems

Declaración de autoría y originalidad del trabajo

Doctorado en Ingeniería de Sistemas y Servicios para la Sociedad de la Información (DISSSI)

Como el autor de esta tesis doctoral, declaro que el trabajo presentado aqui para su ex-posición y defensa es original; no he utilizado fuentes de información sin mencionar de forma clara y estricta su origen, tanto en el cuerpo del texto como en la bibliografía.

Statement of Authorship

Doctoral Degree in Systems and Services Engineering for the Information Society (DISSSI)

I declare that this dissertation and the work presented in it are my own and has been generated by me as the result of my own original research. Where I have consulted the published work of others, this is always clearly attributed. Where I have quoted from the work of others, the source is always given. With the exception of such quotations, this thesis is entirely my own work.